A HYDRODYNAMIC CHARACTERIZATION OF TIDAL ECOSYSTEMS WITH RESPECT TO PREDATION

A Thesis
Presented to
The Academic Faculty

by

William Alexander Berry

In Partial Fulfillment
of the Requirements for the Degree
Masters of Science in the
School of Civil and Environmental Engineering

Georgia Institute of Technology
December 2009

A HYDRODYNAMIC CHARACTERIZATION OF TIDAL ECOSYSTEMS WITH RESPECT TO PREDATION

Approved by:

Professor Donald R. Webster, Advisor
School of Civil and Environmental Engineering
Georgia Institute of Technology

Professor Marc J. Weissburg
School of Biology
Georgia Institute of Technology

Professor Terry W. Sturm
School of Civil and Environmental Engineering
Georgia Institute of Technology

Date Approved: 20 August 2009

ACKNOWLEDGEMENTS

I would like to thank my advisor, Dr. Donald Webster for all of his support throughout the process of bringing this thesis to life. His tireless guidance and input have helped me grow both professionally and personally. I would also like to thank my committee members, Dr. Marc Weissburg and Dr. Terry Sturm, for all of their insight. This work is much improved thanks to their comments. The source material for this study comes exclusively from field work performed by Dr. Lee Smee and Dr. Matt Ferner. Thanks to both for searching through forgotten files and memories to answer all of my questions.

Sarah Delavan has been a wonderful friend and cube-mate in my time at Georgia Tech. I was fortunate to have someone doing work similar to my own who could catch many of the mistakes I've made. It is also nice to see some of the things developed in this study put to use elsewhere.

I would like to thank the students in the Environmental Fluid Mechanics and Water Resources Department, particularly those in the Webster group. Your friendship and advice have been much appreciated.

Throughout the course of writing this thesis, my family and frends have been very supportive. I am thankful for the happiness you have brought into my life.

I would like to thankfully acknowledge the financial support provided by the National Science Foundation (NSF Grant OCE0424673)

TABLE OF CONTENTS

LIST OF TABLES

LIST OF FIGURES

SUMMARY

This study seeks to identify naturally occurring differences in the turbulent environment at a variety of field sites near the Skidaway Institute of Oceanography, in Wassaw Sound and surrounding bodies of water. The sites previously have been used to study predator-prey interactions while also considering the impact the physical environment has on these processes ([33], [9], [35]). Turbulent flow properties serve to mediate the transmission of chemosensory cues which in turn exert an influence on predation. The current study seeks to give a more in-depth characterization of the sites from a turbulent flow perspective.

Velocity time records were recorded using acoustic Doppler velocimetry (ADV) probes at six sites on four days, with a total of 14 data sets. Each set consists of 5 minute bursts sampled at 16 Hz with 15 minute intervals between bursts, spanning at least one complete tidal cycle of incoming and outgoing tides.

ADV data were subjected to differential estimate phase filtering in order to identify erroneous velocity measurements. Less than 3% of the total samples were identified as velocity spikes for any given data set with the exception of three sets that were composed, at least partially, of nonphysical banded bursts. The mean burst-average velocity statistics were largely unaffected by phase filtration. In contrast, the turbulent kinetic energy (TKE) reduced in magnitude following phase filtration, which indicates the influence of ADV data spikes on turbulence quantities.

Because the data were collected in estuarine field sites where waves were present, wave contributions to TKE and Reynolds shear stress were computed. Power spectral

densities (PSDs) were computed for each velocity burst. From the PSD it is possible to separate the contribution to power spectral density from wave-related and turbulent fluctuations. Based on this separation, the wave component of TKE and Reynolds shear stress were computed. For most sets, the wave contributions to turbulent characteristics were between 10-20% of the total, and the maximum contribution was 85.5% of the total value. While the results for the TKE were consistent and reliable, high variability in wave impact for the wave contribution to Reynolds stress was observed.

Burst-average velocity statistics, TKE, Reynolds shear stress, and turbulence intensity (TI) were computed for each data set. Because multiple sites were monitored over multiple days, it was possible to examine the variation spatially and temporally. Large variability in turbulent characteristics was observed at different sites on the same day as well as within the same site over different days. Tidal influences were apparent as turbulent characteristics often reached absolute maximum values during the incoming or outgoing tides, and sites on the whole were less energetic at high tide when flowrates should be at a minimum. No consistent trends were observed in relationships between the sites. In some cases, sites located on Wassaw sound directly had lower TKE and Reynolds shear stress than those located further upstream, where sites would be expected to be less energetic.

The findings of the study emphasize the importance of applying data filtration to raw ADV data, suggest an order of magnitude of wave contributions in a particular tidal ecosystem, and demonstrate the inherent variability of turbulent characteristics. The high levels of variability are consistent with the complex predator-prey interactions that have been observed in the Wassaw Sound ecosystem. The study also illustrates the importance of calculating multiple turbulence parameters for a give site, due to the lack of observed relationships between TKE, TI, and Reynolds shear stress.

While TI and root-mean square velocity fluctuations have most commonly been hypothesized to affect predator-prey interactions, further work is needed to determine if other parameters that are relevant from a flow characterization standpoint are also important ecologically.

CHAPTER I

INTRODUCTION

The current study seeks to identify naturally occurring differences in the turbulent environment at a variety of field sites near the Skidaway Institute of Oceanography. Prior predation studies ([33], [9], [35]) have documented some characteristics of the field sites, but an in-depth characterization of the sites from a turbulent flow perspective has not been performed. Flow data collected at the same site for a sequence of a few days and concurrently across sites allows for the examination of differences both spatially and temporally. An understanding of the turbulent environment in these sites serves to illuminate some of the factors mediating the transmission of chemical signals, which in turn play a role in the predator-prey interactions among local organisms that shape ecological processes.

1.1 Environmental Importance of Turbulence

While the inherent randomness and vast diversity of turbulent flows pose significant hurdles to fully understand turbulent behavior, adequately describing turbulent effects is crucial to understanding the role it plays in the natural environment. Of particular interest in environmental pursuits is the fate and transport of chemicals. In this usage, fate refers to the function within the environment of the chemical, while transport refers to the temporal evolution of the chemical's spatial distribution. Turbulence plays a crucial role in the transport of chemicals, which in turn ultimately mediates their fate. The fate and transport of chemicals has been shown in a variety of applications to be important in shaping both community- and individual-level

biological interactions ([50] and [17]). In boundary layer flows, turbulent characteristics moderate organism behavior, benthic algal distributions, resource availability to deposit and filter feeders, the breakdown of organic matter, and gas and nutrient exchange [30]. Turbulence differences within a riverine setting have been shown to strongly influence biodiversity and spatial distribution of aquatic organisms, where the spatial diversity was attributed to nutrient availability gradients affected by turbulent mixing and transport [15].

Interactions between predators and prey in aquatic settings are strongly influenced by flow characteristics. Crustaceans, fishes, echinoderms and gastropods have all be observed to respond to aquatic stumulus plumes derived from food sources (reviewed in [51]). Because sensory information can be limited, particularly near the boundary layer where visibility may be low, chemical cues carried in the flow are a valuable resource to both prey and predators (reviewed in [53]). Bed roughness and the resulting effect on chemical signal mixing and transport has been shown to influence the tracking behavior of blue crabs *Callinectes sapidus* to food sources in a series of laboratory experiments (see [49], [27] and [18]). In both laboratory and field studies, turbulence manipulation experiments have shown that the influence of increased flow and mixing depends on both the physiology of the predator and prey organisms (see [49], [33], [9] and [24]). In particular, slower moving predators can function better at high flow rates in the presence of more dispersed chemical signals, whereas mobile predators function best at lower flow rates when chemical plumes are more coherent ([10] and [18]).

An ecosystem of particular interest is the tidally driven estuary, where multiple hydrodynamic forces (tides, wind, freshwater flow, density stratification and porewater infiltration, for example) serve to mediate organism- and community-level interactions. Despite the great number of ecological studies that focus on estuarine systems,

hydrodynamic characteristics of these ecosystems have seldom been described (see [32], [45], and [40] for examples). Among these studies, fewer still focus on smaller estuaries and the tidal channels associated with them. To quote Trevethan and Chanson [40], "... to date virtually no studies have been conducted on the physical properties in small estuaries anywhere in the world."

1.2 Complexities of Field Data

In contrast to a controlled laboratory setting, significant difficulties and challenges arise in the collection of field data. Complex geometries, unsteady flows, and irregular disturbances such as changing atmospheric conditions, upstream inputs, and anthropogenic or organismal interference can all affect flow characteristics such as mean flowrates, turbulent fluctuations, turbulent kinetic energy (TKE), bed shear stress, et cetera. The spatial and temporal variability of studies in a natural environment means that additional steps must be taken to quantify the connection between effects and observations.

Data in this study were collected with acoustic Doppler velocimeters (ADVs). An ADV uses the signal lag between an acoustic signal and its reflection to calculate the Doppler shift between signals, which is converted to a three-dimensional average velocity for a sampling volume [21]. ADVs are portable, sample at high frequency (16 Hz in this study), and can collect data for multiple days, features that make them a popular choice for field work. However, it is critical to properly estimate data quality. In this study, ADV probes were deployed at field sites for multiple days and were exposed to the open air at low tides. The ADV units compute data quality parameters such as correlation percentage and signal to noise ratio, which allows for the removal of clearly erroneous data.

Further, a study by Goring and Nikora [12] tested a variety of methods for identifying erroneous "spikes" in ADV data. Spikes occur due to aliasing of the Doppler signal, resulting in erroneous data that may still have good correlation percentage and signal to noise ratio. Of the methods tested, a modified phase filtration technique using estimated first and second order velocity differentials and an application of the Universal threshold for normal random variables was found to best identify spikes within ADV data. Polynomial fitting was then used to replace identified points. This study used the Goring and Nikora [12] method to evaluate the quality of the data collected by the ADVs and assess its impact on the results.

Turbulent measurements are more difficult to accurately obtain in aquatic systems in the presence of waves. Grant et al. [13] identified the potential for wave fluctuations contributing to apparent turbulent fluctuations, which can occur if sensors are improperly aligned with the principal axes of the flow or if there is sloping bed geometry [43]. The apparent wave contribution to turbulent quantities can result in inaccurate calculations that either over- or underestimate parameters due to wave fluctuations that should not be considered turbulent because of their low frequency periodicity. This study follows the methodology of Bricker and Monismith [4] to identify and remove wave contributions to the turbulent kinetic energy (TKE) and Reynolds shear stress, two quantities that provide important information about the turbulent environment at each site. The study also assesses the importance of wave influence at each site.

1.3 Study Objectives

The objective of the current study is to analyze field ADV data collected at six sites near the Skidaway Institute of Oceanographic in May 2007. The raw data consist of time records for periods of greater than one tidal cycle. Data were collected

simultaneously at three or four sites, facilitating spatial comparisons. Data were collected at the same site for a series of days, facilitating a temporal comparison. Ultimately, the flow and turbulence characteristics will be discussed to provide insight into the distribution and success of whelk and blue crab predators at these sites.

CHAPTER II

LITERATURE REVIEW

This chapter reviews literature describing the general characteristics of turbulent flows and acoustic Doppler velocimeters. More specific information is reviewed regarding tidal boundary layer flows and the impacts of tidal flows on ecological interactions. The objective is to review current knowledge in order to provide background and context for the research described in the following chapters.

2.1 Turbulent Flows

2.1.1 Turbulence Classification

The classification of fluid motion into laminar and turbulent flows was first presented by Osborne Reynolds [28], regarding experiments in circular pipes. Dye was injected into flows of varying velocity. At low velocities, dye streaks were advected downstream in a stable, predictable manner with minimal mixing, which are characteristics of laminar flows. As the flow velocity increased the dye streaks became unstable, showing oscillations in time and increased mixing, which was termed the transitional range of the flow. Upon reaching a critical velocity value, fluctuations in the dye streaks became fully random in all directions and mixing across the pipe cross section quickly occurred. Reynolds observed that this transition occurred at a critical value of the dimensionless parameter now known as the Reynolds number ($Re = \frac{\bar{u}d}{\nu}$), a function of mean fluid velocity ($\bar{u}$), pipe diameter (d), and fluid kinematic viscosity (ν). The Reynolds number is the ratio of inertial forces to viscous forces on fluid elements in a

given flow. For low Reynolds numbers, viscosity provides a stabilizing effect, and the flow is stable and laminar. Large values of the Reynolds numbers are indicative of relatively large flow inertia compared to viscosity effects, which magnifies disturbances and the flows exhibit turbulent characteristics such as random fluctuations in flow variables. Reynolds also observed that the transition to turbulence could occur at lower Reynolds numbers in the presence of outside disturbances or relatively rough pipes, indicating a variable range of the transitional flow regime and the lack of a universal critical Reynolds number.

Despite significant research focus since the work of Reynolds [28], turbulent flows continue to be notoriously difficult to describe and predict. Tennekes and Lumley [39] provide a useful description of characteristics that all turbulent flows possess:

- Irregularity: All turbulent flows exhibit randomness, requiring statistical approaches to turbulence problems.
- Diffusivity: Turbulent fluctuations serve to create large gradients of velocity, momentum, and passive scalars, resulting in increased rates of mixing and momentum, heat, and mass transfer.
- Large Reynolds numbers: A large Reynolds number is required for turbulent flows, as turbulent phenomena develop from instabilities that occur when the Reynolds number reaches a critical value.
- Three-dimensional vorticity fluctuations: Turbulence is three-dimensional and rotational, and furthermore identified by vorticity fluctuations. Vortex stretching, a necessary vorticity persistence mechanism cannot occur in two-dimensional flow.
- Dissipation: Turbulent flows serve to dissipate energy as viscous shear stresses smooth the small-scale velocity fluctuations and convert kinetic energy into

heat. The removal of kinetic energy from a turbulent system requires, as a consequence, a constant energy input from an external source such as the mean flow for turbulent phenomena to persist.

- Continuum: The fundamental equations of fluid mechanics govern turbulent motions because fluctuations at the smallest scales are much larger than molecular length scales.

- Flow dependence: Turbulent phenomena are characteristic of flows, not the material fluids themselves. At large Reynolds numbers, many turbulent mechanisms are similar across molecular differences between fluids. It therefore follows that flow characteristics rather than fluid properties determine turbulent behavior.

Turbulent flows also display generalized or universal behavior at large Reynolds numbers. Richardson presented the idea of an energy cascade within turbulent flows [29]. Kinetic energy of velocity fluctuations is produced in turbulent flows at large scales, is cascaded through inviscid processes to smaller and smaller scales, and is finally dissipated by viscous effects. This theory is complemented by the idea that turbulence is composed of eddies of varying sizes, where an eddy is defined as a form of rotating turbulent motion that is coherent on a defined length interval. Large length scales are roughly half the size dimensions of the mean flow, whereas the smallest scales are determined by the viscous dissipation rate.

Kolmogorov's first similarity hypothesis furthered this phenomenological approach to turbulent behavior, arguing that at small scales, turbulent motions are statistically isotropic, meaning directionally independent, and that statistics of small scale turbulent motion should be universal for all Reynolds numbers [20]. Dimensional analysis arguments then indicate that these motions and their statistics are functions solely

of the energy dissipation rate, ϵ, and fluid viscosity, ν. Combinations of these parameters yields the Kolmogorov scales for length, velocity, and time, which serve to describe the behavior of the smallest eddies [23]. Kolmogorov's analysis included a range of scales between the largest eddies (l_0) and the Kolmogorov length scale (η) in which turbulent flow statistics are a function of ϵ and ν alone. This intermediate range is commonly termed the inertial subrange, while lengths closer in magnitude to the smallest eddies are known as the dissipation range. The combined inertial subrange and dissipation range are known as the universal equilibrium range. Further dimensional analysis leads to an equation for the energy spectrum $E(\kappa)$ using the compensated Kolmogorov spectrum function $\Psi(\kappa\eta)$ within the universal equilibrium range: $E(\kappa) = \epsilon^{\frac{2}{3}}\kappa^{-\frac{5}{3}}\Psi(\kappa\eta)$, where κ is the spectral wavenumber. In the inertial subrange, $\Psi(\kappa\eta)$ tends towards a constant value, yielding the Kolmogorov -5/3 spectrum: $E(\kappa) = C\epsilon^{\frac{2}{3}}\kappa^{\frac{-5}{3}}$ (see Figure 2.1). Kolmogorov's assumptions and resulting equation for energy spectrum behavior in the inertial subrange allow for an estimate of the energy dissipation rate. The -5/3 dependence has also been frequently observed experimentally.

2.1.2 Statistical Descriptions of Turbulence

2.1.2.1 Random Variables

Non-linear behavior leads to the characteristic randomness of turbulence. A statistical approach to describe the quantities of interest, including the three-dimensional velocity and pressure fields, is therefore necessary. Each term of interest in the Navier-Stokes equations can be treated as a random variable, such as the velocity field $u(x,t)$, where u is the instantaneous velocity field and x is the spatial position. A sample value of a random variable is called an event. While the value of each random variable is not discrete, it is possible to describe the probability that an event within a

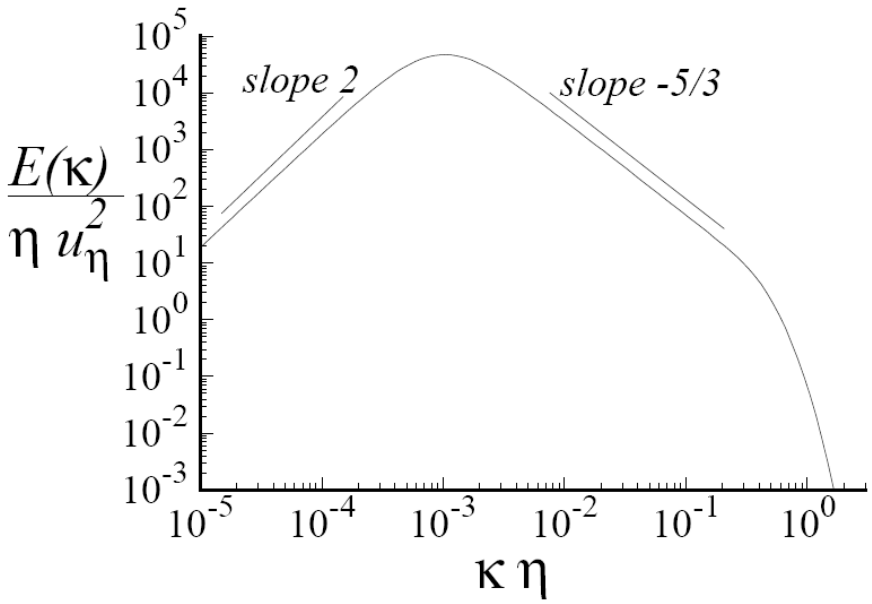

Figure 2.1: Spectrum normalized by the Kolmogorov scales (Source: [23]).

certain range of values will occur. An independent velocity variable V, defined as the sample-space variable, can be used to describe ranges of interest and the probability of an event occurring in that range. For the event $B \equiv \{u \leq V_b\}$, the probability of the event occurring is denoted

$$p = P(B) = P\{u \leq V_b\} \tag{2.1}$$

The probability of an event in a range can be expressed, therefore:

$$P\{V_a < u < V_b\} = F(V_b) - F(V_a) = \int_{V_a}^{V_b} f(V)\, dV \tag{2.2}$$

where $F(V)$ is the cumulative distribution function and $f(V)$ is defined as the probability density function (PDF). From a known PDF it is possible to calculate the mean value of a random variable:

$$\bar{u} = \langle u \rangle = \int_{-\infty}^{\infty} V f(V)\, dV \tag{2.3}$$

as well as the variance:

$$var(u) = \langle (u - \bar{u})^2 \rangle = \int_{-\infty}^{\infty} (\bar{u} - V)^2 f(V)\, dV \tag{2.4}$$

where the notation $\langle\rangle$ indicates averaging and behaves like a linear operator. In turbulent flows, the random variables of each velocity component, the pressure, and the scalar quantities are not independent. For joint random variables that may not be independent from one another, a joint PDF similarly can be defined to describe the probability that events will occur. From a joint PDF, it is possible to compute the covariance:

$$\begin{aligned} cov\left(u_1, u_2\right) &= \left\langle (u_1 - \bar{u_1})(u_2 - \bar{u_2}) \right\rangle \\ &= \int_{-\infty}^{\infty} \int_{-\infty}^{\infty} \left(V_1 - \bar{u_1}\right) \left(V_2 - \bar{u_2}\right) f_{12}\left(V_1, V_2\right) dV_1 dV_2 \end{aligned} \tag{2.5}$$

and the correlation coefficient:

$$\rho_{12} = \frac{cov\left(u_1, u_2\right)}{\sqrt{var\left(u_1\right) var\left(u_2\right)}} \tag{2.6}$$

2.1.2.2 Reynolds Decomposition

Experimental measurements of turbulent flows do not a priori follow known distribution functions of the random variables. These variables often are measured in the form of a time series. Based on measurements of the random variable $u\left(x,t\right)$, it is possible to calculate the time average value $\bar{u}\left(x\right)$:

$$\bar{u}\left(x\right) = \lim_{t_0 \to \infty} \frac{1}{t_0} \int_0^{t_0} u\left(x,t\right) dt \tag{2.7}$$

where t_0 is a time period that is much longer than the characteristic temporal fluctuations of the record. This approach is valid for statistically stationary flows whose mean behavior does not change with time. From the mean value it is possible to perform a Reynolds decomposition to isolate the fluctuating part of a random variable, $u\left(x,t\right)$:

$$u'\left(x,t\right) = u\left(x,t\right) - \bar{u}\left(x\right) \tag{2.8}$$

The autocorrelation function can be used to describe how the fluctuating part of a random variable correlates to itself in time:

$$R(s) = \frac{\langle u'(t)\, u'(t+s)\rangle}{\langle u'(t)^2\rangle} \tag{2.9}$$

The correlation function provides a measure of how well the flow remembers previous velocity samples as a function of the delay period, s.

2.1.3 Turbulent Boundary Layers

Boundary layer flows develop when a unidirectional mean flow with velocity $\bar{u}$ moves past a surface where the no-slip friction condition is applied, generating a wall-normal velocity gradient. The comments in this section relate to flat plate boundary analysis. The general notation for boundary layer flows is that the x-direction is aligned with the free stream flow direction, and the z-direction is perpendicular to the surface. The boundary layer forms near the wall to provide the interface between the wall constraint and the free stream flow, and its thickness grows in the x-direction. Important physical parameters include the shear stress at the wall τ_w and the viscous length scale $\delta_\nu = \dfrac{\nu}{u_\tau}$, where u_τ is the wall shear velocity ($u_\tau^2 = \tau_w/\rho$). Two dimensionless variables, z^+ and u^+, where $z^+ = z/\delta_\nu$ and $u^+ = \bar{u}/u_\tau$ are used to create self-similar scaling profiles for the mean flow quantities (see Figure 2.2).

The boundary layer thickness $\delta(x)$ is generally defined as the height above the physical boundary where the time-averaged velocity is equal to 99% of the free stream velocity, although this quantity is difficult to experimentally verify due to measurement uncertainty [23]. If the free stream velocity is constant, the Bernoulli equation can be used to show that there is no streamwise pressure gradient, and vice versa. In a boundary layer flow with negligible pressure-gradient, laminar behavior will occur when the Reynolds number is small, which can be described by a similarity solution

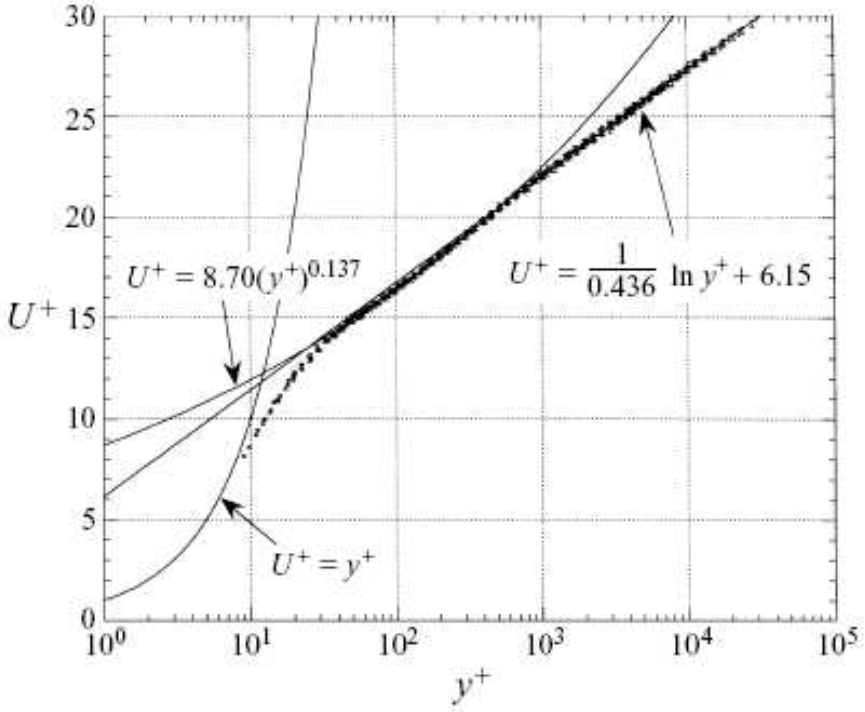

Figure 2.2: Velocity profile normalized with inner scaling variables for pipe flow at various Reynolds numbers. Note that in this figure, y is used to describe the wall normal direction. (Source:[52]).

by Blasius [3]. When the mean-flow-direction Reynolds number reaches a critical value $Re_x \approx 10^6$ [23], the flow begins to transition to turbulence. Dimensional analysis leads to the argument that the mean velocity profile is only a function of z/δ and $z^+ = z/\delta_\nu$. Prandtl proposed the law-of-the-wall, stating that within the viscous sublayer, the normalized velocity profile was only a function of z^+ [25]. The no-slip condition at the wall, combined with a Taylor expansion of the unknown function, yields a third order approximation of $u^+ = z^+$ close to the wall ($z^+ < 5$, see Figure 2.2). Further from the wall ($z \gg 1$), von Karman [46] argued that viscosity could be neglected and developed the log-law profile:

$$u^+ = \frac{1}{\kappa} ln\left(z^+\right) + B \tag{2.10}$$

where $\kappa = 0.41$ and $B = 5.2$ (see Figure 2.2). When $z^+ > 50$ or $z/\delta > 0.2$, the flow is in the outer layer and can be assumed to be independent of viscosity. However, universal behavior in the outer layer does not exist, as the mean velocity profile varies for different flow conditions. It is important to mention that the velocity defect law can be used to normalize profiles for flat plate boundary layer flows.

The turbulent kinetic energy budget can be examined in order to gain insight into the turbulent nature of the flow. Direct numerical simulations of turbulent kinetic energy performed by Spalart [36] showed production of turbulent kinetic energy starting at zero at the wall and increasing to a maximum in the log-law region. Production decreases and remains non-zero in the outer layer. Turbulent kinetic energy dissipation rate is a maximum near the boundary, and steadily decreases in magnitude further from the boundary. For much of the layer, the balance is between production and dissipation rate [23].

2.2 Acoustic Doppler Velocimetry

2.2.1 Function

Kraus et al. [21] outlined design parameters for a three-dimensional point velocity sensor to be used in research initiatives to study flow behavior at entrances and inlets, involving tidal flow, wave-induced currents, wave-current interaction, and wave transformation. The current meter utilized the Doppler-shift of acoustic waves to measure velocity. An acoustic source signal is emitted from a transmit transducer. If the signal encounters tracer material such as suspended sediments, microbubbles, or seeding particles, a fraction of the acoustic pulse is scattered. A series of receiver transducers detect the backscatter in a defined sampling volume (see Figure 2.3).

The scattered signal experiences a frequency shift related to the velocity of the tracers, which are assumed to move with the flow. The fixed geometry of the transducers then allows for the velocity vector field to be resolved as an average of the readings within the sampling volume. This device is referred to as an acoustic Doppler velocimeter (ADV).

ADV devices offer many advantages over alternative velocity measuring methods. Probes are relatively small and durable, allowing them to be effectively utilized in the field, unlike laser Doppler velocimetry (LDV), which is usually confined to laboratory settings [47]. The acoustic nature of the sampling technique is non-intrusive, yielding no flow interference from the device itself, unlike electromagnetic current meters (ECMs). ADV sample volume and sampling rate also compare favorably to ECMs, and the spectral and temporal scales of turbulence that can be resolved are limited by these factors. The small sample volume also allows for measurements to be taken closer to the bed than techniques with larger sample volumes such as travel-time acoustic sensors. ADV techniques resolve velocity components in three dimensions,

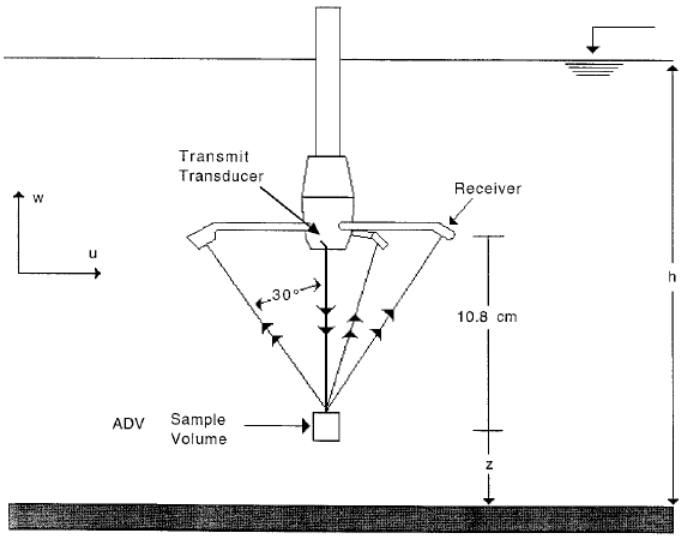

Figure 2.3: Example sensor geometry and sample volume for an ADV (Source: [47]).

allowing for the successfully measurement of mean flows, Reynolds stresses, turbulence intensity, and estimates of bottom shear stress [47].

2.2.2 Limitations

While ADV probes have many advantages, there are some important limitations to ADV measurements. With respect to turbulence, the spatial and temporal resolutions of the device are limiting factors as to what turbulent phenomena can be observed. Instrument calibration is necessary for near-bed ADV measurements, where Finelli et al. [11] found variability in sampling volume depth. Relative to measurements by hot-film velocimetry, ADV measurements within 10 mm of the bed underestimated velocities by as much as 80%, which is a larger value than could be attributed to differences in spatial resolution between the two instruments. Near the bed, hot-film velocimetry point velocity measurements spatially integrated across the nominal ADV sampling volume height were much greater than the actual ADV data collected with the nominal sample volume located in this range. The study also used a monofilament target to provide a stable source of feedback in measuring the extent of the ADVs sample volume. The effective sample volume height was determined to be on the order of double the nominal, factory-specified value. If an ADV is mistakenly positioned so that its sample volume includes the bed, the accuracy of results sharply decreases, so it is important to correctly identify the sample volume height. Precht et al. [26] also found the actual sampling volume height of an ADV to be approximately double that of the nominal value. Additionally, data quality parameters such as signal-to-noise ratio and signal amplitude were evaluated for their effectiveness in identifying when measured data are of poor quality. While the inflation of these parameters above their open water values does indicate that the sample volume is partially sampling

the bed, they are not accurate indicators of when the transition occurs, as the accuracy of measured velocities when compared to laser Doppler velocimetry (LDV) measurements decreases before these parameters increase noticeably. Precht et al. [26] recommends a conservative limit of 2.5 times the nominal sample volume height is an acceptable distance from the bed to obtain accurate ADV measurements.

Voulgaris and Trowbridge [47] compared ADV, laser Doppler velocimetry (LDV) and combined "ground truthing" measurements derived from known relationships between noise and "true" parameters for each method and the assumption that noise variability for each acoustic beam has the same magnitude and is uncorrelated to the other beams. The study found that the ADV underestimated the mean flow velocity by 1% relative to the LDV, which could be attributed to inaccuracies in aligning the sample volumes at the same heights. Another source of error in mean velocity estimation is the fact that within a boundary layer the velocity profile is distributed logarithmically, so a velocity estimate based on the arithmetic average across the sample volume in this region will give a biased estimate that is determined by the shape of the mean velocity profile. Reynolds stress measurements with the ADV were on average only 1% lower than ground truth values. Drombroski and Crimaldi [8] also compared ADV and LDV measurements, finding that ADV data at distances from the bed greater than 1 cm at slower flow ($Re = 670$) and greater than 0.7 cm at faster flow ($Re = 1410$) were within 5% of LDV readings. The ADV had a nominal sampling volume height of 0.9 cm and a calculated sample volume height of 1.3 cm. Variability with Reynolds number is attributed to changing boundary layer profiles, which Voulgaris and Trowbridge [47] estimated to be on the order of 0.1%, and bed effects. While the sample volume should not include the bed at distances 0.7 cm above it, it is still possible that a large object such as the bed could have a disproportionately large signal response than the smaller monofilament targets used in the sample volume extent estimation. Drombroski and Crimaldi [8] also noted that because near-bed

velocity estimates were underestimated relative to LDV and noise removal served only to increase that underestimation, the use of data filtering is not helpful in improving the accuracy of ADV measurements near the bed.

2.2.3 Data Post-Processing

One potential source of error when using ADV probes to measure velocity is the aliasing of the Doppler signal. If the phase shift between the incoming and outgoing signal is greater than $\pm 180°$, an erroneous spike can occur in the data (see [12]). Velocity values exceeding the range of the device or interference from previous pulses that have been reflected off irregular surfaces can create spikes, which unfortunately can often look like regular velocity fluctuations. Goring and Nikora [12] examined a variety of methods for identifying and removing spikes within an ADV time series. They compared the effectiveness of RC filtration, the Tukey 53H method (which uses the median as a robust estimator of the mean), an acceleration thresholding method (using estimates of acceleration compared to that due to gravity), a wavelet thresholding method (using acceleration comparisons to gravity in wavelet space), and the phase-space thresholding method. The phase space thresholding method, which Goring and Nikora [12] conclude is best suited for improving ADV data, is based upon the imposition of the Universal criterion on estimates of first and second derivates for the time series. The Universal criterion is the expected absolute maximum expected for a random normal variable with zero mean and an estimator of standard deviation. A 3D Poincaré map is created, and the Universal criterion is used to generate an ellipsoid that should theoretically bound all the acceptable data points in the time record. The points outside the ellipsoid are then passed through an interpolation procedure, of which Goring and Nikora [12] reccommend a third order polynomial fit using 12 points on either side of an identified spike. This combination of spike

detection and interpolation was determined to be the most effective at improving data quality for noisy data sets.

Following the methodology of Goring and Nikora [12] , Chanson et al. [6] found that "pre-filtering" of ADV data, involving the removal of obvious disturbances such as navigation, probe movement, or aquatic organism interference were similarly important to improving data quality, as nearly 12% of the total flagged points would be missed without the removal of large disturbances. The study found that turbulent properties changed dramatically between pre- and post-processing procedures, and that hydrodynamic characteristics could not be accurately computed from raw ADV data.

2.3 Tidal Boundary Layers

2.3.1 Intertidal Dynamics

Estuaries and other tidally driven near-shore regions are complex and dynamic systems with multiple driving forces, identified by LeHir et al. [22] in an observation of three intertidal flat regions. The primary forcing mechanism within a tidal basin is the tide itself. Because tidal wavelengths are generally longer than the width of the study areas, the water depth is approximately horizontal normal to the shore. Retarding effects of shallow water and bottom roughness can inhibit tidal propagation, resulting in nonzero surface elevation gradients. While the primary component of tidal currents is usually in the long-shore direction, cross-shore components also exist with magnitudes depending on basin width. Long-shore currents are affected by the topography of the basin. Tidal currents provide a source of mean flow within a basin, resulting in the development of boundary layers and accompanying bed shear stresses that are important to mixing, sediment transport, and ecological processes. Water

surface elevations can be influenced by wind and atmospheric pressure gradients. The propagation of waves from offshore or locally generated wind waves can alter the water surface profile and generate secondary currents. Wave-induced shear stresses can be the same order of magnitude as tidally-induced shear stresses, although the former can be strong at high tide when the latter become insignificant [22]. In an estuarine system, salinity or temperature differences also can drive circulation patterns. Sediments that are exposed by receding tidewater can drain porewater and add another flow input into a system.

Internal consistency analysis of 192 velocity profiles performed by Collins et al. [7] found that the assumption of a logarithmic boundary layer is not always applicable in tidally-driven flows. Less than 40% of the analyzed flows were found to have a logarithmic velocity profile. This deviation from theory was attributed to the unsteadiness of tidal currents, surface non-uniformities and bedforms, suspended sediment, water column stratification, and bed-load transport. The results of the study also identified rotational tidal flows, wind influence close to the water surface, logarithmic profile disruption by oscillatory water motion, and secondary flow characteristics as potential factors in deviation from logarithmic velocity profiles. Oceanic swells also can play an important role in intertidal dynamics [38]. Defined as ocean waves with periods between 10 and 20 seconds, these swells have been shown to be an important source of shear stress and near-bed energy when there is little tidal forcing and wind-wave influence. The hydrodynamic environment in a tidally driven sandflat in the Manukau Harbour, New Zealand was characterized by Bell et al. [1]. Using current meters, sediment surveys, sediment tracking and numerical modeling, the study observed a heirarchy of forces acting upon the sandflat. Mean current velocity and bed shear stress were primarly affected by semi-diurnal tides, with secondary influences driven by the wind. Tidal asymmetry was observed at the site, where the incoming current and outgoing current were not mirror images, influenced by topography, tidal currents

and wind. Flows were generally at a maximum during the outgoing tide. While tidal currents alone were not strong enough to initate sediment transport, the presence of small-scale orbital currents served to redistribute sediment into to ridges and runnels that were observed at the site. The study serves to illustrate the importance of considering the complex coupling of factors in a tidally-driven system that span a variety of time scales (long period tides to high frequency orbital currents).

Kawanisi and Yokosi [19] used electromagnetic and ultrasonic current meters to quantify turbulent behavior in a tidally-driven river. The mean velocity lagged slightly behind the water level, with maximums following high and low tides. Salinity measurements indicated that vertical stratification found in ebb tides reduces the ratio of Reynolds stress to turbulent intensity, whereas flood tides can be considered well mixed and have larger ratios. The ratio of vertical to horizontal integral length scales also decreases with increasing vertical stratification, indicating that large vertical velocity fluctuations are more damped by buoyancy than those in the horizontal direction. Turbulent velocity behavior was studied in an estuary through the use of electromagnetic flowmeter by Shiono and West [32]. Near-bed fluctuations were shown to behave similarly to bed-generated turbulence found in laboratory settings and to generate a well-mixed zone near the bed during flood tides. Shear-generated turbulent behavior was observed during the ebb tide, with larger velocity and density gradients.

The role of suspended sediment in altering turbulent behavior in a tidal channel through density modification was investigated by van der Ham et al. [45]. In a silt and clay tidal channel, the study found that while near-bed turbulent fluctuations were not affected by sediment-related density gradients, farther from the bed the integral length scale was reduced. Acoustic Doppler velocimetry, laser diffraction, and optical backscatter were used by Voulgaris and Meyers [48] to investigate sediment transport

behavior in a tidal creek. The study observed the full range of tide strengths from neap to spring tides, and found that while some sediment transport occurs during ebb neap tides, erosion rates are highest during an ebb spring tide, where strong currents re-suspend sediments that are then transported downstream. Tidal creeks therefore serve as a sediment source to the salt marshes they often drain into.

Turbulence and environmental impacts were measured in a small estuary in Eastern Australia by Chanson et al. [5]. The study is one of few to investigate turbulent properties in a small estuary, and served as the inital data set for future studies. One study was performed in the same estuary by Trevethan et al. [41], where ADVs were used to measure turbulent variation over several tidal cycles. The study found that velocity magnitude in this estuary peaked before and after low tide, and that maximum flood velocities exceeded ebb velocities. The same estuary was the focus of a more comprehensive study by Trevethan and Chanson [40]. ADVs were employed in the long-term monitoring of turbulent characteristics within the estuary. The study again observed maximum velocities immedately preceding and following low tides and flood tide velocities that exceeded those of the ebb tide, suggesting a net flux of water upstream. Within the estuary, turbulent properties exhibited great variability. Relative turbulence intensities at the site were large when compared to similar results from larger estuaries, attributed to increased turbulent activity due to greater friction and bed roughness impacts in shallow water. The study illuminates some important turbulent characteristics of small estuaries and calls for further study of these ecosystems from a hydrodynamics standpoint, as even among estuaries there can be significant variability.

2.3.2 Turbulence Characterization

Gross and Nowell [14] studied a tidal channel with a well mixed flow over a uniform bed to evaluate the validity of wall scaling measures in tidal flows. A set of 11 triple-ducted current meters logarithmically spanning a depth of 4 meters were used to measure velocity profiles. Dissipation rates were estimated from the assumption of the Kolmogorov -5/3 law in the linear portion of the horizontal velocity fluctuation spectra. When compared to the production term estimated from the bed shear stress and assumed wall of the law profile shape, production and dissipation rate were in agreement for heights greater than one meter above the bed. Near the wall the local Reynolds number, a function of the shear velocity, was found to be small. Because the width of the inertial subrange scales with this Reynolds number, the length of the subrange near the wall was not large enough to be accurately resolved with the current meters. Resulting estimates of energy dissipation rate therefore underestimated the total amount of energy dissipation in this region. Gross and Nowell [14] found that dissipation rate estimates were lower than corresponding production estimates within one meter of the bed. As predicted by theory, probability distributions of velocity fluctuations were found to be nearly Gaussian (see Figure 2.4).

Measures of fluctuation products, such as the Reynolds stress, were found to resemble leptokurtic distributions far from the bed. Near the bed, the Reynolds stress probability distribution exhibited lower kurtosis than would be expected from a product of normal random variables. This difference was attributed to the greater overall level of turbulence near the bed while extreme values of Reynolds stresses remained at the same magnitude far or near the bed. The turbulent shear velocity and wall length scale were found to be adequate to describe the boundary layer. Turbulent shear velocity scaled with the mean velocity shear, Reynolds stress, and dissipation rate in all regions except near to the bed. Vertical velocity fluctuations and therefore the

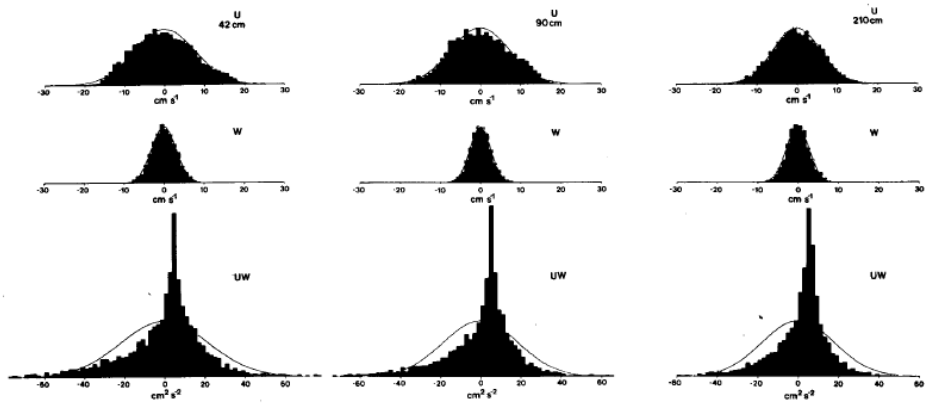

Figure 2.4: Distributions of horizontal and vertical velocity fluctuations as well as their product at varying heights (42 cm, 90 cm, and 210 cm) above the bed in a turbulent boundary layer. Fitted curves are the best fit normal distribution (Source: [14]).

cospectra had low energy in small wavenumber regions, indicating that low-frequency periodic eddies are not prevalent in the vertical direction. The study concluded that most tidal boundary layers can be classified as having a quasi-stationary balance of turbulent kinetic energy.

Trowbridge et al. [44] used benthic acoustic stress sensors to measure velocity profiles in a partially-mixed estuary in order to evaluate the applicability of the law-of-the-wall and characterized the momentum balance in the system. Turbulent kinetic energy production and dissipation rate were found to be in balance for all of the observations. The law-of-the-wall was validated within 1 meter of the bed for all flooding tides, but no agreement was found for ebb tides. Because local stratification was not large enough to account for the ebb tide departure, the finite thickness of the well-mixed layer below the pycnocline was identified as a possible source of the greater shear stress causing the departure from the law-of-the-wall.

2.3.3 Wave Influence

Potential interference in turbulent fluctuations from surface energy in the form of waves was identified by Grant et al. [13]. Because internal waves can have orders of magnitude more energy than turbulent eddies, it is important to identify wave contributions to apparent turbulent kinetic energy [31]. These contributions arise because it is often not possible to properly rotate measured velocity vectors into alignment with the principal axes of wave-induced velocity fields in practice. Trowbridge [43] introduced a method for the removal of wave energy using two velocity sensors that are separated spatially. The critical assumption was that if the distance between the sensors was large relative to the scale of turbulent motions and small relative to the wavelength of the waves, that wave and turbulent motions would be uncorrelated. The two measurement sets could then be differenced to remove the wave effects while preserving the behavior of the turbulence. Order of magnitude analysis showed that the above assumptions combined with the assumption of weakly nonlinear waves should yield a wave bias one order of magnitude below typical near-bed Reynolds shear stresses. Shaw and Trowbridge [31] extended this method by utilizing a difference for only one of the measured parameters, either the horizontal or vertical velocity, in the estimation of both Reynolds shear stress and heat flux. Further modifications were made in the use of least-squares filtering to approximate the coherent velocity components, allowing for differences in phase and amplitude of the waves to be minimized. When applied to experimental data, Shaw and Trowbridge [31] found that using horizontal velocity differencing was successful and superior to using vertical velocity differencing to remove surface wave effects in the unfiltered case. However, more energetic surface waves (such as during extreme weather conditions) were better addressed by the filtering methods with differencing in either the vertical or horizontal direction. Internal waves posed a greater challenge, due to their

intermittency. While high-pass filtering can remove the internal wave contribution to apparent Reynolds shear stress, this approach cannot be used for turbulent heat flux.

It is possible to address wave contributions to turbulence with a single velocity sensor [4]. Assuming equilibrium turbulence and no interactions between waves and turbulence, the phase lag between the horizontal and vertical velocity components is used to approximate the energy contribution of turbulence and therefore remove the wave energy within the inertial subrange. Because wave energy co-occurs spectrally with turbulent energy, bandpass filtering will lose important turbulent information. It is also difficult to interpolate the turbulence cross-spectral density because it can be positive or negative. Bricker and Monismith [4] instead used the autospectral densities of the horizontal and vertical velocity components, which are always positive. The wave peak is identified and delineated, either by hand or by some peak-finding algorithm and replaced with a least squares approximation of turbulent energy for each direction, from which the cross-spectral density, post-wave removal, can be reconstructed. The results of the decomposition when applied to both laboratory and field data sets and compared to established two-sensor methods indicate the methodology is sound close to the bed where wave strain is small. Large wave strain fields consist of turbulent frequencies that co-occur with wave peak frequencies, so turbulence could be attributed to wave bias erroneously. In order to identify wave peaks for many data sets, an empirical peak identifying metric must be used, which has the potential to introduce error.

2.3.4 Ecological Impacts

Turbulent characteristics have significant impacts on various features of tidally-driven basins. Because these environments function as complex ecosystems, it is becoming increasingly clear that turbulent characterization of flow fields can illuminate the role

that the physical environment plays in community- and individual-level biological interactions. The objective of this section is to provide a brief overview of some of the research that has connected turbulent flow characteristics to ecological activities.

In boundary layer flows, turbulent behavior at the bed moderates invertebrate distribution and movement, benthic algae distributions, the supply of organic material to and removal of waste from deposit and filter feeders, the breakdown of organic matter, and gas and nutrient exchange [30]. Turbulence can result in a decrease in interval between contact between small particles and the bed, possibly allowing invertebrates who avoid predators by entering the flow to escape while preventing transport beyond a significant distance from a suitable habitat. Increased dissipation and fluctuation rates characteristic of turbulent flow serve to increase oxygenation and evenly distribute organic matter. Growns and Davis [15] classified invertebrates as flow obligates, facultators, and avoiders and surveyed their densities in a stream and characterized flow conditions. Obligates were found preferentially in turbulent regions with large bed shear stresses. Facultative organisms were found more often in areas with large bed roughness, attributed to the increased refuge that the roughness elements provided from flow. Flow avoiders were found in areas with large shear stresses, bed roughness, and turbulence, where greater nutrient fluxes and entrained oxygen were likely to occur.

Turbulent transport of chemical signals is an important process that serves to mediate many ecological and evolutionary processes (reviewed in [53]). Physiological impacts of various flow conditions and chemical predator cues on the topmouth gudgeon (*Pseudorasbora parva*), a prey fish were examined by Sunardi et al. [37]. Visual cues (adjacent caged predator), predator odorant cues (water from caged predators), and alarm cues (killed conspecifics) at various flow rates were presented to the gudgeons. In order of increasing effect, visual cues, predator odor, and alarm cues all

served to induce increased metabolic rates, ventilation, and movement in the prey fish. Predictably, an increased metabolic response was also found for increasing flow rate, although interactions between flowrate and cues did not have a significant effect on physiological stress. The lack of a combined impact was attributed to the large magnitude response to larger flowrates serving to mask the response to the predation signals. The study primarily illustrates the importance of chemical signaling and it follows that factors that mediate the delivery of these messages can also affect predator-prey interactions.

Weissburg and Zimmer-Faust [49] found in a laboratory setting that flow properties influenced the chemical tracking ability of blue crabs foraging for hard clams. Greater levels of boundary layer turbulence decreased the ability of predatory crabs to chemically orient themselves in the flow field. A critical factor in boundary layer turbulence is bed roughness, as studied by Rahman and Webster [27]. The study used planar laser-induced fluorescence (PLIF) to study chemical plume behavior in a channel flow with bottom sediments of varying roughness. The downstream rate of increase of the plume width and decrease in centerline concentration were accelerated by greater bed roughness. Increased bed roughness results in lower and faster decreasing variance of concentration fluctuations in the downstream direction. Time-averaged concentration profiles were observed to be Gaussian except at large distances downstream, where bivariate distributions developed.

The impact of bed roughness on odorant transport was examined via behavioral trials by Jackson et al. [18]. Tracking trials using blue crabs, *Callinectes sapidus*, and varying bed roughness were compared to the PLIF imaged plume data quantified by Rahman and Webster [27]. Blue crabs were presented with an odorant plume composed of shrimp-conditioned water under identical conditions to those in the PLIF observations. At greater roughness levels, the blue crabs moved at lower walking speeds and

were significantly less successful at tracking to the odorant source. Further insight was gained through the examination of vertical plume structure with respect to the blue crab sensory arrays (antennules and distal appendages). At the antennules, plume properties change dramatically with increased roughness, with much lower variability and mean concentration values. The decrease in signal quality at the antennule height is a significant factor in the decrease in crab foraging success. Because sensors on the appendages are separated spatially, the transverse plume structure near the bed is a relevant characteristic of odorant plumes.

Substrates with greater roughness resulted in plumes with greater width and crab behavior correspondingly included larger transvere movements. This behavior was attributed to the need for crabs to make bilateral comparisons, nominally with one set of appendage sensors in the plume and one set outside of the plume, in order to follow the contour upstream to the odorant source. When bed roughness is greater and the plume exhibits greater transverse width, the crabs must either increase the spatial separation between sensors or move further from the plume centerline. The hypothesis is validated by the observed tendency of crabs to move towards the outer edges of the plume in successful tracks. These observations indicate how physical parameters affecting flow conditions and turbulent mixing mediate predator-prey interactions.

Studies of the turbulent impacts have also been extended to the field. Hart et al. [16] used hot-film anemometry to quantify the turbulent microenvironment near the surfaces of rocks that were inhabited by larval blackflies (*Simulium vittatum*). Larval blackflies are suspension-feeders requiring a steady influx of food sources and therefore should preferentially anchor themselves in areas with ideal hydodynamic conditions. More larvae were found on rocks with relatively large flow velocities within 2 mm of the rock surface. No correlation was found at 10 mm, however, leading Hart et al. to emphasize the importance of small-scale characteristics in the microenvironment

and to condemn the sole use of free-stream parameters when the study organism has a small range. Interactions between predatory knobbed whelks (*Busycon carica*) and blue crabs (*Callinectes sapidus*) and prey bay scallops (*Argopecten irradians*) and hard clams (*Mercenaria mercenaria*) were observed in manipulated channels in the field by Powers and Kittinger [24]. Hinged plywood channel dividers served to either increase or decrease natural flow rates and restrict the predator-prey interaction area. The study found that predator and prey response to flow rate varied in both magnitude and direction (increase or decrease of sensory abilities). Blue crabs, which are relatively mobile, had foraging success affected by flow rate and independent of prey species. Blue crab predation decreased with increasing flow and was attributed to the increased mixing and dissipation of chemical cues due to enhanced turbulence found at greater flow rates. Knobbed whelks, which are less mobile relative to blue crabs, exhibited foraging efficiencies that were dependent only on the prey species assayed. The findings indicate that whelk foraging was not affected by the flow rate levels used in the experiment. The slow traveling speed of whelks allows for relatively greater temporal integration of available cues, which has been suggested as a mechanism for increased foraging success in turbulent environments [10]. Powers and Kittinger [24] found that any predator avoidance behaviors used by clams were ineffective with regard to whelk predation. Whelk predation on bay scallops actually increased at larger flow rates. Because whelk predation did not vary with flow rate in the whelk-clam pairing, Powers and Kittinger [24] ascribe the findings to behavioral changes in the scallops. While scallops have shown successful avoidance behaviors, they are usually mediated by chemosensory information gathered from tentacles. Because increased current speeds can cause scallops to retract their tentacles and the associated increased turbulence can rapidly dilute chemical signals, scallop ability to detect predators at greater flow rates could be compromised. The variability in magnitude and direction of flow rate on both predators and prey in this study illustrate

the importance of the transport of chemicals in natural systems.

The presence of caged predators has been shown to increase clam survival in the field due to chemically-mediated behavioral changes in clams [34]. Smee et al. [33] studied predator-prey interactions between caged blue crabs and hard clams in a tidally-driven estuarine system with manipulated levels of turbulence to illustrate the role that turbulent mixing plays in chemical signal transport and resulting predation success. Smee et al. [33] placed caged blue crabs 0.5 m and 2 m from plots of clams. The caged predators were surrounded with a ring of shell hash or left in a natural state (i.e., mud). Acoustic Doppler Velocimetry (ADV) was applied to measure the increase in turbulent fluctuations induced by the shell hash. The study found that the placement of crabs 0.5 m from the clam plots with and without shell hash increased clam survival relative to clam plots with no caged predator. Clam survival similarly increased for caged crabs 2 m from the clam plots without shell hash, but the presence of shell hash at this greater distance had no effect on clam survival rates. The study concluded that at the 2 m spatial scale with increased turbulent mixing, the clams were unable to detect the caged predator or alter their behavior accordingly. In a similar study considering whelk-clam interactions, Ferner et al. [9] found that while caged whelks increased clam survival rates, the introduction of shell hash around clam plots led to decreased clam survivability, regardless of the presence of a caged predator. Both studies serve to illustrate the importance of turbulent chemical transport in tidally-driven basins.

Because natural environments are rarely characterized by binary "on or off" factors but rather by gradients of contrasting effects, it is important to consider turbulent characteristics beyond merely "enhanced" and "natural." A study by Smee et al. [35] considered predator-prey interactions between blue crabs and hard clams. Root-mean-squared velocity was calculated from ADV observations in concert with

predation assays at 4 sites in Wassaw Sound. Blue crabs were found to have the most foragaing success in areas with moderate levels of turbulence and mean velocity, but had reduced success in areas with high or low turbulence and mean velocity. Smee et al. [35] hypothesize that while intermediate turbulence is not ideal for crab foraging, nonlinear interactions between the perceptive abilities of both prey and predators results in foraging success at intermediate levels. At low turbulence levels, the perceptive abilities of both clams and crabs are not compromised, and clam predator avoidance behavior can be effectively employed. At high levels of turbulence, chemosensory perception is severely limited in both crabs and clams, and the crabs are unable to forage successfully. The findings of the study indicate that with increasing turbulence, clam perception decreases at a greater rate than that of the crabs, yielding a perceptive advantage to the crabs. The study illustrates the importance of considering organismal responses to gradients of turbulent properties.

CHAPTER III

METHODS

3.1 Site Description

Data were collected at various sites located near the Skidaway Institute of Oceanography, Savannah, Georgia, USA. The sites are considered representative of soft-sediment habitats characteristic of estuarine environments in the Southeastern United States and provide habitats for aquatic organisms such as clams and their predators. The intertidal sites were located in the Skidaway, Wilmington, Herb, and Moon Rivers as well as at Dead Man's Hammock and House Creek (see Figure 3.1).

Sites exhibit extended periods of unidirectional flow and are tidally driven. The sites are bordered by marsh (*Spartina alterniflora*), have average salinities between 20-28 ppt, a tidal range of 2-3 m, and receive small levels of freshwater inflow [35]. Substrates primarily consist of fine-grained sand and mud. The sites were located roughly 10 to 20 meters from oyster (*Crassostrea virginica*) reefs. The proximity to these areas of biological activity allowed for investigation of predation effects (see [34], [33], [9], [35]).

The DMHsh20 and DMHco20 sites were both located near Dead Man's Hammock, and were located in close proximity to each other over a shell substrate and a mud substrate, respectively. The Herb, Wilmington, Skidaway and Moon River sites were selected for additional studies of predation interactions between blue crabs (*Callinectes sapidus*) and hard clams (*Mercenaria mercenaria*), due to their location inland from Wassaw Sound [35]), whereas the House Creek and Dead Man's Hammock sites were

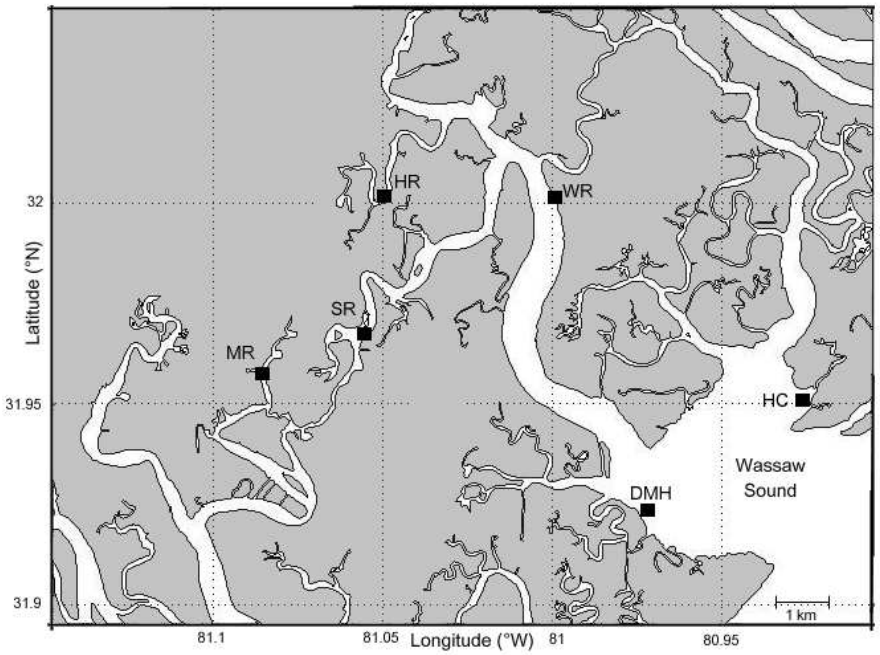

Figure 3.1: Location map for field sites. ADV measurments were taken at Herb River (HR), Wilmington River (WR), Skidaway River (SR), Moon River (MR), House Creek (HC) and Dead Mans Hammock (DMH).

chosen for predation studies between whelks (*Busycon* spp.) and hard clams based on their location on the Sound itself.

3.2 Data Collection

All data were collected by Lee Smee and Matt Ferner in support of their recent papers [34], [33], [9], [35]. The velocity data have received limited processing, and a primary objective of this thesis is to provide a more complete analysis and discussion of the data. The specific data sets reported in this thesis have not been presented in the referenced papers.

3.2.1 Equipment

Acoustic Doppler Velocimeters (NortekUSA^{TM}Vector Model or Sontek/YSI ADV-Field) were placed simultaneously at up to four sites for data collection and were configured using vendor supplied software. The probe geometry is similar to that shown in Figure 2.3. The ADV's recorded 3-components of velocity, signal-to-noise ratio, and correlation coefficient for each sensor.

3.2.2 Data Collection Procedure

A single ADV was mounted on a PVC frame at each site. Probes were placed such that the x-direction is roughly parallel to the mean flow direction (See Figure 3.2). In all cases, the direction upwards from the bed corresponds to positive z-component velocity.

Data were collected at 16 Hz in 5 minute bursts. 10 minute intervals were used between bursts, resulting in the collection of 4 bursts per hour. ADV units were placed with the center of the sampling volume located 0.20 m above the bed and

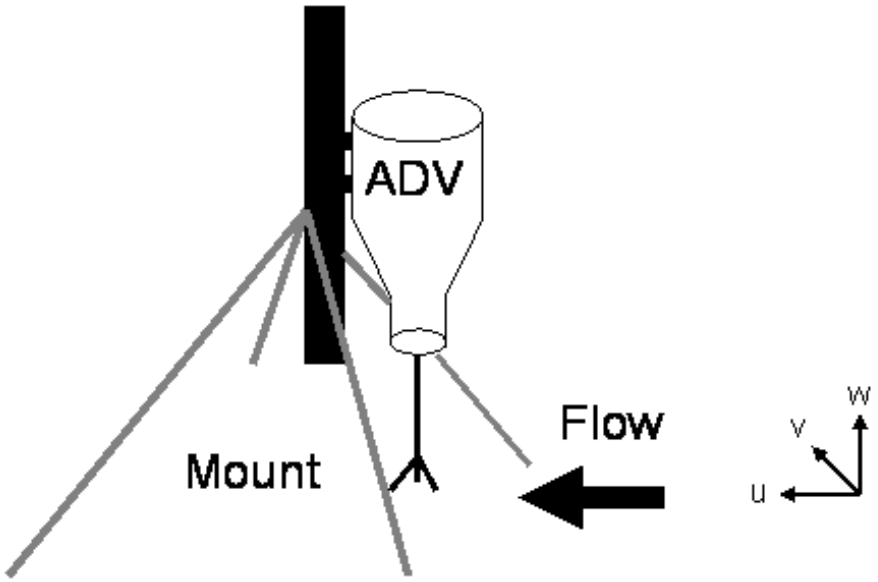

Figure 3.2: Diagram of field deployment of ADV probe.

at the mean lower-low water (MLLW) contour. This placement allowed for proper functioning of the ADV while ensuring the probe was fully submerged for the majority of the monitoring period. ADVs were deployed for a minimum of one tidal cycle. See Table 3.1 for more information about the individual data sets. The DMH (side) data set collected on 5/16/07 was obtained using a side-mounted ADV. The DMH control and DMH shell sets were collected at two closely paired sites, one over the typical sand and mud substrate (DMH control) and one over a shell substrate (DMH shell).

3.3 Data Manipulation

3.3.1 Basic Filtering

Velocity data were first evaluated at the burst level to identify and remove data sets with poor quality. The mean values of the three correlation coefficients were computed for each burst, and the entire burst was discarded if the mean value of

Table 3.1: ADV data collection information for each data set. DMH is the abbreviation for Dead Mans Hammock.

Site	Data Set Name	Start Time	Bursts	Retained Bursts
Herb River	Herb14	5/14/2007 12:00:00	123	54
Wilmington River	Wilmington14	5/14/2007 12:03:00	122	79
Skidaway River	Skidaway14	5/14/2007 12:05:00	77	55
Moon River	Moon14	5/14/2007 12:09:00	67	46
DMH (side)	DMHside16	5/16/2007 14:00:00	214	141
Herb River	Herb16	5/16/2007 14:00:00	215	127
DMH	DMH16	5/16/2007 14:00:00	62	41
House Creek	House16	5/16/2007 14:00:00	214	114
Herb River	Herb19	5/19/2007 19:00:00	44	43
Skidaway River	Skidaway19	5/19/2007 19:00:00	44	44
Wilmington River	Wilmington19	5/19/2007 19:00:00	60	43
DMH Control	DMHco20	5/20/2007 19:00:00	42	42
DMH Shell	DMHsh20	5/20/2007 19:00:00	45	44
Moon River	Moon20	5/20/2007 19:00:00	32	1
Skidaway River	Skidaway20	5/20/2007 19:00:00	64	47

any correlation coefficient was below 70%. This threshold is the generally established value below which instantaneous velocity measurements become unreliable. Typically, poor correlation coefficient values corresponded to bursts collected while the probe was exposed to the atmosphere at low tides. To further identify bursts where poor data quality could impact results, any burst with a string of 500 consecutive points (31.25 seconds out of 5 minutes total) having a mean correlation coefficient below 50% was also excluded. This additional criteria was added to identify those bursts when the probe was exposed for only a portion of the burst, but the burst mean correlation was high. Table 3.1 summarizes the number of bursts retained for each set after applying the correlation coefficient threshold criterion. Excluding the Moon River set Moon20, 26% of the bursts were removed across the remaining 14 data sets on average. No further analysis of the Moon20 set was performed due to the lack of quality data remaining after the basic filtering procedures.

The next preparatory step was to rotate the x- and y-direction velocity components such that the magnitude of the x-direction velocity was maximized within each burst. The rotated velocity data provide a consistent reference point for turbulent characteristics, as the mean flow is not expected to dramatically change over the 5 minute burst sampling period, but will vary over the sequence of bursts. Rotation was manipulated to ensure that the rotated x-direction velocity component would primarily be positive for the incoming tide and negative for the outgoing tide. Please see Section 4.3 for further discussion of tidal behavior.

3.3.2 Phase Filtering

Following the rotation and burst-level filtering, a more extensive procedure was employed to filter individual velocity measurements that were determined to be erroneous due to Doppler floor noise, aliasing of the Doppler signal, and other reasons. The procedure closely follows the methodology laid out by Goring and Nikora [12] and involves differencing estimates of first and second order derivatives. Individual velocity measurement filtering was composed of two components: spike detection and spike replacement.

3.3.2.1 Spike Detection

The criterion for identifying erroneous velocity measurements is derived from the assumption that the velocity measurements behave as n independent, identically distributed, standard, normal random variables ξ_i. The value of the Universal threshold, λ_U, of a set is

$$E(|\xi_i|_{max}) = \sqrt{2 \ln n} = \lambda_U \tag{3.1}$$

Given an estimation, $\hat{\sigma}$, of the standard deviation of a normal random variable with zero mean, the expected absolute maximum value of a set is:

$$\lambda_U \hat{\sigma} = \sqrt{2 \ln n} \hat{\sigma} \tag{3.2}$$

The procedure for the Phase-Space Thresholding Method is a follows. First, velocity derivatives are estimated from the following differences:

$$\Delta u_i = (u_{i+1} - u_{i-1})/2 \tag{3.3}$$

$$\Delta^2 u_i = (\Delta u_{i+1} - \Delta u_{i-1})/2 \tag{3.4}$$

The time step Δt is not used in the derivative estimates, which will be discussed in detail below. Second, calculate the standard deviation of each variable σ_u, $\sigma_{\Delta u}$, and $\sigma_{\Delta^2 u}$ and calculate the expected maximum value of the variables from Equation 3.2. Third, the rotation angle of the principal axis of the $\Delta^2 u_i$ versus u_i plot are calculated from the cross-correlation (rotation angles for other correlations are zero because of symmetry):

$$\theta = \tan^{-1}\left(\sum u_i \Delta^2 u_i / \sum u_i^2\right) \tag{3.5}$$

Fourth, using the extreme values calculated in Equation 3.2, two-dimensional ellipses are computed for each plane. See Table 3.2 for further details, where a and b are the major and minor axes of the ellipse in the u_i versus $\Delta^2 u_i$ plane. The following system of linear equations are solved for a and b:

$$(\lambda_U \sigma_u)^2 = a^2 \cos^2\theta + b^2 \sin^2\theta \tag{3.6}$$

$$(\lambda_U \sigma_{\Delta^2 u})^2 = a^2 \sin^2\theta + b^2 \cos^2\theta \tag{3.7}$$

Table 3.2: Major and minor axes for the projected ellipses used in phase filtering. a and b are the major and minor axes for u_i versus $\Delta^2 u_i$.

Plot	x-axis Amplitude	y-axis Amplitude
u_i vs. Δu_i	$\lambda_u \sigma_u$	$\lambda_u \sigma_{\Delta u}$
Δu_i vs. $\Delta^2 u_i$	$\lambda_u \sigma_{\Delta u}$	$\lambda_u \sigma_{\Delta^2 u}$
u_i vs. $\Delta^2 u_i$	a	b

where θ is the rotation angle of the principal axes defined in Equation 3.5. Note that Δt was not used in the estimation of first and second order derivatives because differences of orders of magnitude between standard deviation values can lead to a poorly conditioned matrix from Equations 3.6 and 3.7. The fifth step is to identify those individual points that fall outside the ellipsoid defined in the previous steps, and flag them for spike replacement. Spike detection and replacement are performed repeatedly until the total number of flagged data points becomes constant. Figure 3.3 shows an example of the ellipsoid projections and velocity phase diagrams for the u velocities in a single example burst.

3.3.2.2 Spike Removal and Replacement

Once erroneous velocity samples (i.e., spikes) have been identified, they are replaced by a polynomial best fit. As discussed further in Section 3.3.3, the replaced points were used only to calculate the wave contribution and were not used directly in the calculation of the turbulent statistics. Sample replacement occured at the velocity component level, so the identification of a spike in one component does not necessitate replacing the other velocity measurements at that point. Based upon the recommendation of Goring and Nikora [12], a third order polynomial fit was used, employing 12 points on either side of the identified spike. If additional spikes fall into the range around a spike, the range is expanded. Goring and Nikora [12] found this method to be suitable for sampling rates in the range of 25 to 100 Hz. The 16 Hz sampling

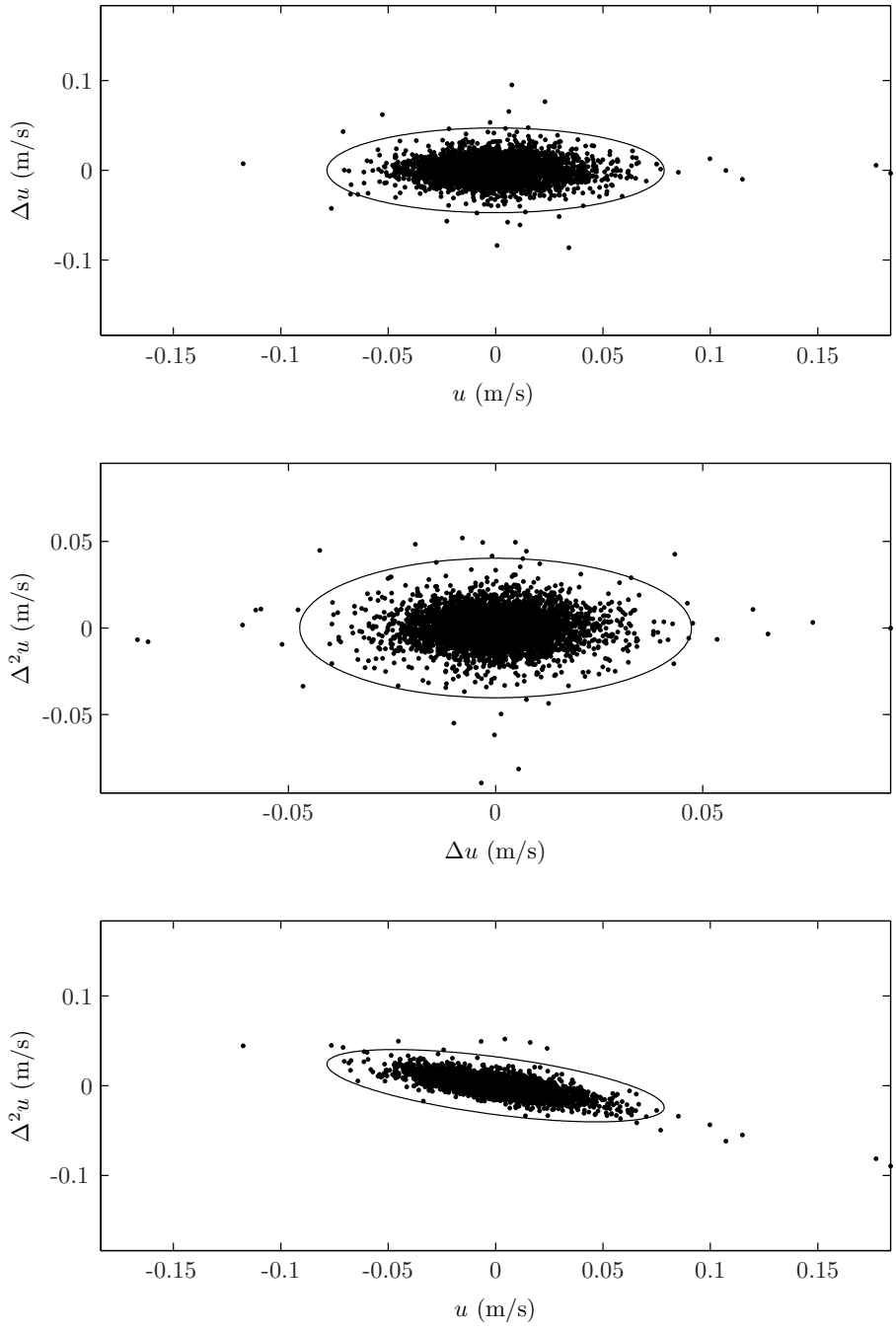

Figure 3.3: Ellipsoid projections and spike identification for an example single burst. Data correspond to the u velocity component from the 21$^{\text{st}}$ burst in the Skidaway20 data set.

rate used in this experiment is close to this range, and visual inspection of pre- and post-filtered data confirmed effectiveness of the sample replacement. See Figure 3.4 for spike removal and sample replacement in an example burst.

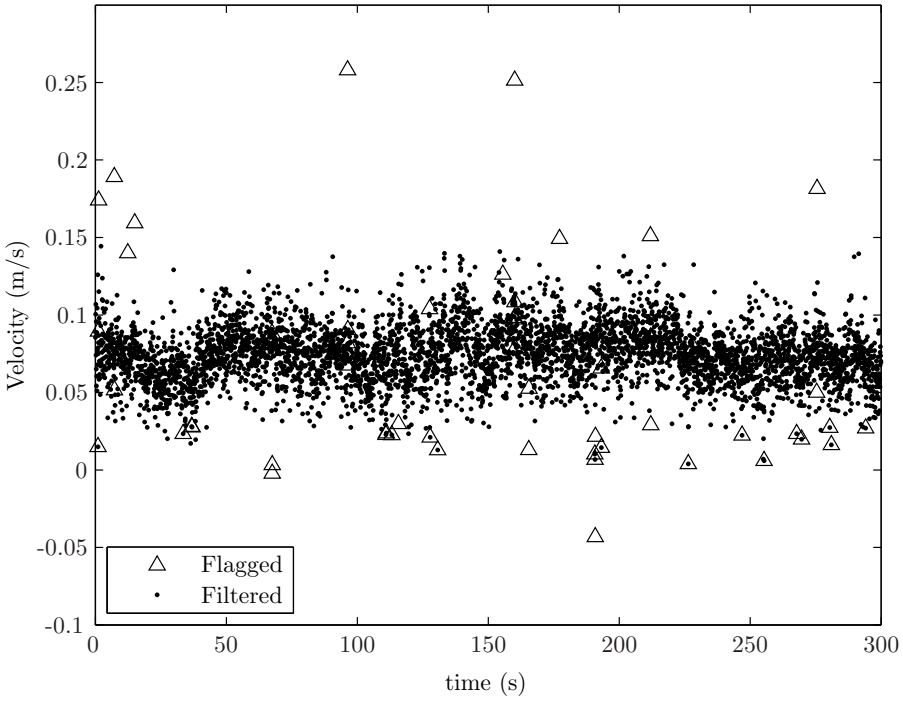

Figure 3.4: Time record of velocity with identified spikes highlighted. Data correspond to the u velocity component from the 21st burst in the Skidaway20 data set.

3.3.2.3 Filtering Efficiency

Table 3.3 reports the percentage of points flagged through the phase filtering method described above. The majority of the sets had few points ($< 3\%$) that were identified as spikes. However, three sets (Herb14, DMHco20 and DMHsh20) all had a relatively large portion of the data flagged for replacement, as shown in Table 3.3. The large number of identified spikes can be attributed to the presence of "banded" data within each set. For further discussion on banding and the methods used to address it, please see Section 3.3.2.4.

Table 3.3: Mean percentage of samples flagged for each data set by the phase filtration method.

Set Name	Mean Percentage Removed
Herb14	28.72
Wilmington14	0.92
Skidaway14	2.37
Moon14	1.92
DMH side16	2.67
Herb16	2.12
DMH16	2.30
House16	1.78
Herb19	2.42
Skid19	1.91
Wilmington19	2.37
DMHco20	70.00
DMHsh20	68.76
Skidaway20	1.86

3.3.2.4 Banded Sets

As seen in Table 3.3, the Herb14, DMHco20 and DMHsh20 sets all had a large number of points flagged for replacement, which is attributed to banding. Figure 3.5 shows a typical banded burst, and Figure 3.6 illustrates the corresponding velocity phase diagrams. Note that the ellipses in the first iteration of the filtering process indicate that a large portion of the data is erroneous. Banded bursts are characterized by the seemingly random jumping of velocity measurements between large negative and positive values that are arranged in discrete bands. Some of these values are outside of the range of detection of the ADV, and calculations performed on these data yield unrealistic results. It is clear that these data are not consistent with the physical constraints of the environment.

The DMHco20 and DMHsh20 sets were almost exclusively comprised of banded bursts. The severity of the banding resulted in the phase filter removing roughly 70% of the data in both sets and reliable results were unattainable. For this reason,

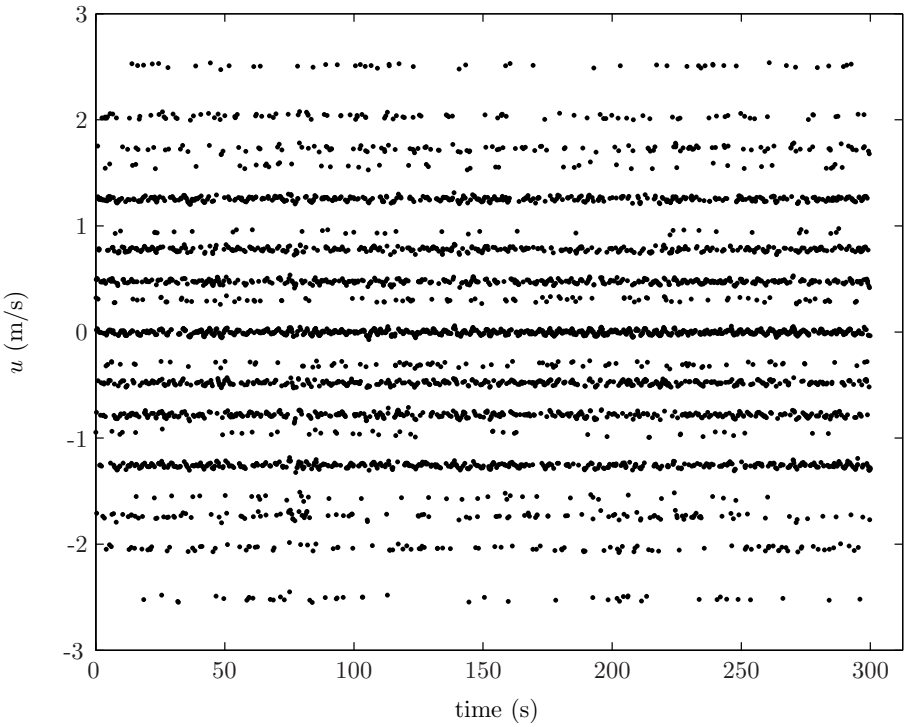

Figure 3.5: Example time record of velocity with banded behavior. Data correspond to the u velocity component from the 40^{th} burst in the DMHsh20 data set.

further analysis of DMHco20 and DMHsh20 will not be presented.

A modified phase filter approach was used for the Herb14 set because the banding was not as severe as the other sets. A burst was characterized as banded if the difference between the maximum and minimum values in a burst exceeded a certain criteria (2 m/s in the u and v directions) or if a standard deviation threshold was exceeded (0.06 m/s in the w direction) and the relative change in the span for the pre- and post-filtered data was small. These threshold numbers were empirically verified to identify banded bursts in the Herb14 data set. Once a burst was identified as exhibiting banded characteristics, the principal axes for the first round of phase filtering were decreased by a correction factor. This procedure allowed the spike smoothing procedure to naturally flag the extreme banded points. After the phase filtering algorithm, the burst was again checked for banded characteristics. If banding remained, the process was repeated with a smaller correction factor. This process

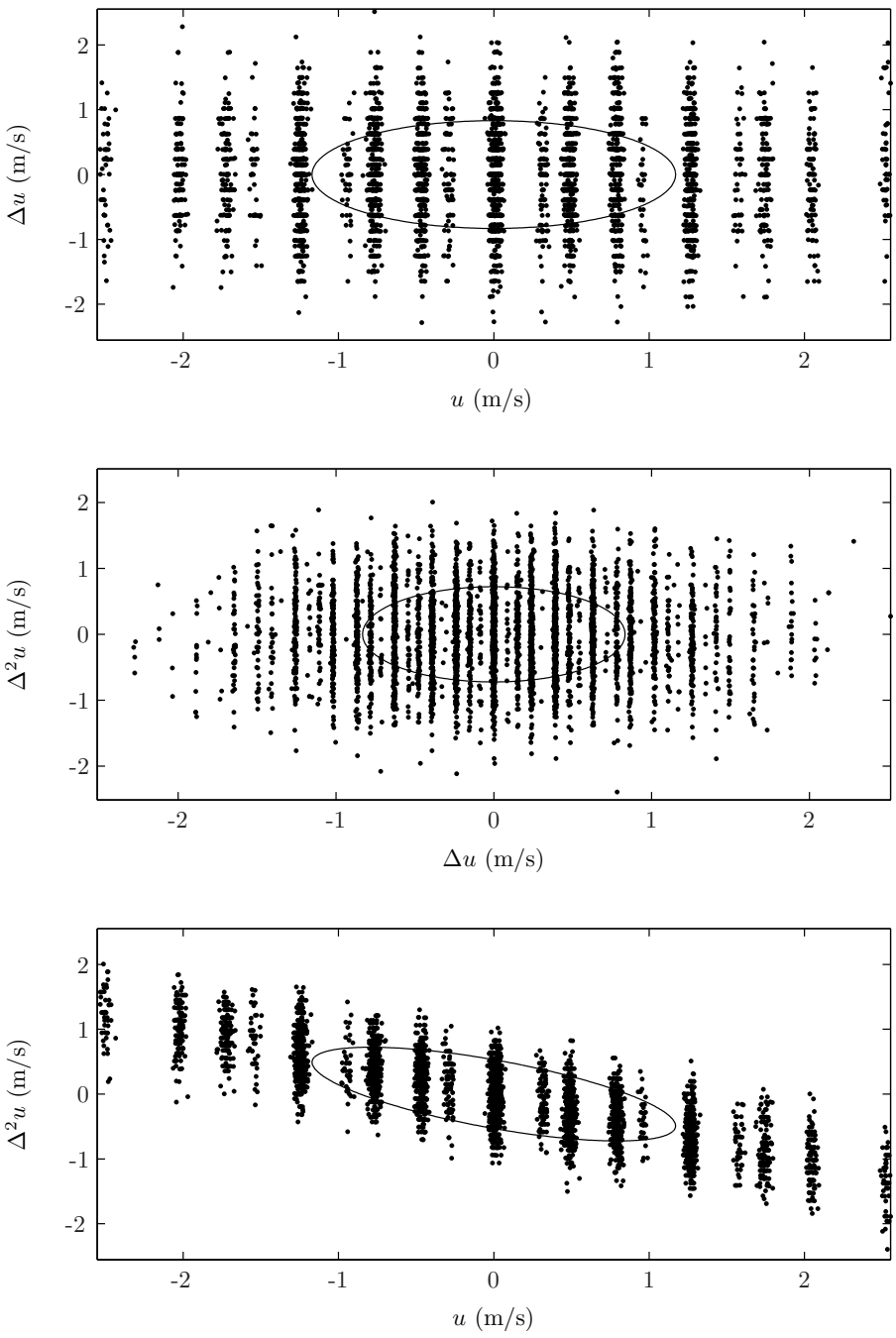

Figure 3.6: Velocity phase diagrams of burst exhibiting banded behavior. Data correspond to the u velocity component from the 40^{th} burst in the DMHsh20 data set.

was repeated at most 5 times when necessary, with the initial principal axes being multiplied by correction factors of 0.40, 0.52, 0.64, 0.76 and 0.88. The decreasing correction factors and corresponding relative increase in principal axis size with each iteration was determined to be an effective means of identifying banded points without interfering with apparrently good data points once the most extreme banded points have been removed. The modified treatment of the Herb14 set yielded results that are more consistent with the other data sets than if this procedure was not employed. Specifically, the standard deviation and visual appearance of the time record were consistent with the other sets.

3.3.3 Wave Removal

3.3.3.1 Reynolds Shear Stress

Because the ADV measurements were taken in estuarine areas that are not far removed from the open ocean, it is important to evaluate and remove the impact of wave influence on the turbulence measurements. The methodology described by Bricker and Monismith [4] has been shown to be an effective means for evaluating wave bias with a single ADV probe. Instantaneous velocity samples are decomposed into the following convention:

$$u = \bar{u} + \tilde{u} + u' \tag{3.8}$$

where $\bar{u}$ is the mean component, $\tilde{u}$ is the wave-induced component, and u' is the turbulent fluctuation. Computing the Reynolds shear stress through Reynolds averaging of the velocity components yields:

$$-\frac{\tau}{\rho} = \overline{\tilde{u}\tilde{w}} + \overline{\tilde{u}w'} + \overline{u'\tilde{w}} + \overline{u'w'} \tag{3.9}$$

Under ideal conditions, the first three terms of Equation 3.9 can be neglected [4]. However, instrument uncertainty or sloping bed geometry can yield $\overline{\tilde{u}\tilde{w}} \neq 0$ in the measurements, which artificially inflates the estimate of the Reynolds shear stress[42] . It is therefore important to estimate this wave-averaged contribution to the Reynolds stresses in flows where wave action may be present.

The wave stress can be estimated based on the Benilov and Filyushkin [2] method:

$$\overline{\tilde{u}\tilde{w}} = \int_{-\omega_{Nyquist}}^{\omega_{Nyquist}} S_{\tilde{u}\tilde{w}}(\omega) d\omega \tag{3.10}$$

where $S_{\tilde{u}\tilde{w}}$ is the two-sided cross-spectral density (CSD) of orbital velocities associated with wave action. Because the turbulence spectrum, and therefore the integral of the spectrum, can be written as the difference between raw velocity spectrum and the wave-induced velocity spectrum, the Reynolds shear stress can be calculated as the following difference:

$$\overline{u'w'} = \overline{(u-\bar{u})(w-\bar{w})} - \overline{\tilde{u}\tilde{w}} \tag{3.11}$$

In practice, the integral expression of Equation 3.10 can be rewritten for a finite discrete data set:

$$\overline{\tilde{u}\tilde{w}} = \sum_{N/2}^{N/2} \tilde{U}_j^* \tilde{W}_j \tag{3.12}$$

where $U_j = U(\omega_j)$ is the Fourier transform of $u(t)$ at frequency ω_j, N is the number of data points in the set, $*$ indicates complex conjugation, and t is time [4].

The challenge remains to remove the wave-induced velocities from turbulence. Because the wave-related energy peak is often found at wavenumbers where turbulence exists, employing a bandpass filter is not acceptable. It is also not possible to interpolate below the cross-spectral density (CSD) to remove the wave-related peak, because

the CSD can be either positive or negative. The single-direction autospectral density (PSD) in either the u or w direction possesses only positive, real values, so it is possible to interpolate below the wave peak (see Figure 3.7). The wave peak was defined as the maximum energy in the PSD that occurred at least 0.1 Hz from the start of the data. The peak width was defined as the region beginning at 70% of the peak frequency and ending 0.5 Hz from the peak frequency. These limits were determined for the data set to best identify the wave peak regions and are expected to be specific to this data set. For Reynolds shear stress calculations, the peak frequency range for the u velocity served to delineate the peak in both the u and w spectra. For normal stress calculations, the peak found for each respective velocity component was used. After the PSD coefficients for the wave peak ($S_{\tilde{u}\tilde{u}}$) have been identified, it is then possible to compute the wave CSD coefficients ($\tilde{U}_j$) from the terms in the PSD:

$$S_{\tilde{u}\tilde{u}_j} = \frac{1}{d\omega}|\tilde{U}_j|^2 \tag{3.13}$$

The Fourier coefficients of the respective velocity components can be expressed in phasor notation

$$U_j = |U_j|^{e^{i\angle U_j}} \tag{3.14}$$

$$W_j = |W_j|^{e^{i\angle W_j}}, \tag{3.15}$$

with the phase of each defined as

$$\angle U_j = \arctan\left[\frac{\mathrm{Im}(U_j)}{\mathrm{Re}(U_j)}\right] \tag{3.16}$$

$$\angle W_j = \arctan\left[\frac{\mathrm{Im}(W_j)}{\mathrm{Re}(W_j)}\right] \tag{3.17}$$

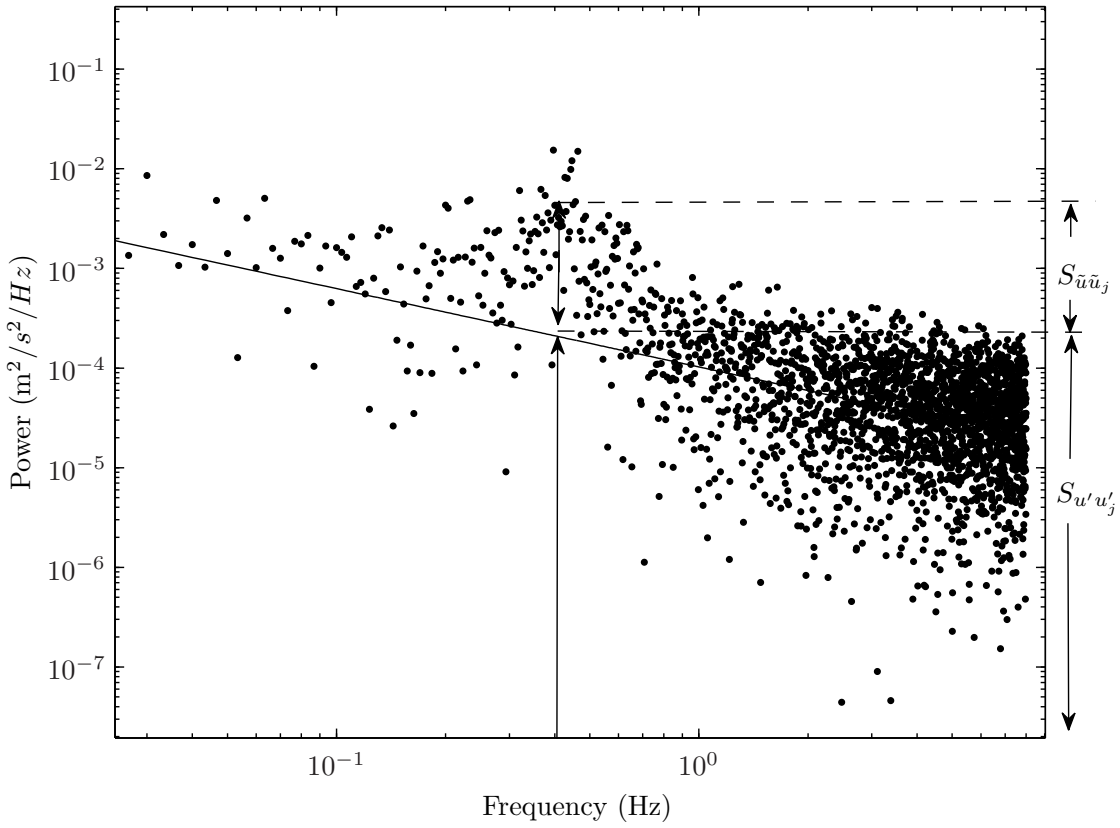

Figure 3.7: Single-direction autospectral density (PSD) of horizontal velocity, S_{uu}, calculated from data in the 130$^{\text{th}}$ burst in the DMHside16 data set. The solid line is a least squares fit to the data points excepting those in the wave peak range. In the wave peak range, the contributions from waves, $S_{\tilde{u}\tilde{u}}$, and turbulence, $S_{u'u'}$, are illustrated at a single frequency.

From Equations 3.14 and 3.15, the spectral component of the CSD can be expressed as:

$$U_j^* W_j = |U_j||W_j| e^{i(\angle W_j - \angle U_j)} \tag{3.18}$$

which can be written as:

$$U_j^* W_j = |U_j||W_j| \left[\cos(\angle W_j - \angle U_j) + i \sin(\angle W_j - \angle U_j)\right] \tag{3.19}$$

The imaginary part of the CSD then can be neglected in the summation over the two-sided spectral domain.

$$\overline{\tilde{u}\tilde{w}} = \sum_{j=\text{wave peak}} \tilde{U}_j^* \tilde{W}_j = \sum_{j=\text{wave peak}} |\tilde{U}_j||\tilde{W}_j| \cos(\angle W_j - \angle U_j) \tag{3.20}$$

The difference between U_j and the turbulent contribution U_j' gives the magnitude of $\tilde{U}_j$. Figure 3.7 illustrates the difference for the PSD components and Equation 3.13 is used to calculate the contribution for the velocity components. This method assumes no wave-turbulence interaction and that the phase of Equations 3.16 and 3.17 is also dominated by waves because waves dominate the signal under the wave peak. Therefore, the wave-induced shear stress can be accurately approximated from Equation 3.20. The wave stress computed from the summation of Equation 3.20 under the wave peak can then be used to calculate the turbulent stress from Equation 3.11.

Reynolds shear stress calculations involved a combination of the output of the phase filtering process. In order to preserve the characteristics of the original data as much as possible, calculations involving fluctuations were computed by excluding any measurement where the phase filtering procedure flagged one of the velocity components for smoothing. However, a continuous data set is required for spectral analysis in

the wave removal calculations, so the interpolated points that replace the flagged data were used in the calculation of the wave contribution. In Equation 3.11, the $\overline{(u-\bar{u})(w-\bar{w})}$ term is computed only from points that were not flagged by phase filtering, while $\overline{\tilde{u}\tilde{w}}$ includes both unflagged original points and flagged smoothed points.

While the wave removal method generally yielded physically plausible results, in a few instances the magnitude of $\overline{\tilde{u}\tilde{w}}$ exceeded that of $\overline{(u-\bar{u})(w-\bar{w})}$, which indicates the wave contribution to Reynolds shear stress was greater than the wave-included fluctuation correlation of which it is theoretically a portion. In all other cases, the wave contribution was small relative to the wave-included fluctuation product (see discussion in Section 4.2 and Table 4.1). For the exceptional bursts where $|\overline{\tilde{u}\tilde{w}}| > |\overline{(u-\bar{u})(w-\bar{w})}|$, the unflagged velocity product $\overline{(u-\bar{u})(w-\bar{w})}$ was substituted in the place of the final Reynolds shear stress, $\overline{u'w'}$.

3.3.3.2 Turbulent Kinetic Energy

The wave component of turbulent kinetic energy (TKE) is computed in a similar manner. The same assumptions made in the Reynolds shear stress calculation are again made here, namely that no wave-turbulence interaction occurs and that the wave contributions are responsible for the peak in the autospectral density (PSD). It is possible to calculate the wave-associated normal stress $\overline{\tilde{u}\tilde{u}}$ from the PSD of a velocity time record of u using the same process used for Reynolds shear stress. The turbulent contribution to normal stress, $\overline{u'u'}$ can then be computed similarly to Equation 3.11. Summing the three normal stresses yields the TKE:

$$TKE = \frac{1}{2}(\overline{u'u'} + \overline{v'v'} + \overline{w'w'}) \tag{3.21}$$

Some TKE results were nonphysical for the Herb14 set, which exhibited a manageable

amount of banding. This stems from the greater value of TKE of the combined wave and turbulent fluctuations in the phase-filtered data set including interpolated points, which must be used because a continuous time record is required for spectral analysis. Data sets including interpolated points generally have larger TKE relative to the set composed of unflagged points only, due to the difficulty in completely removing spikes. For three bursts in the Herb14 set, the TKE including interpolated points was large enough that its wave component was greater than the TKE for unflagged points only, hence resulting in a calculated negative value of TKE for the burst. Because the wave contribution to TKE was generally small, the wave contribution to TKE was neglected for these exceptional cases, and the TKE calculated for unflagged points was used.

It is possible to compute the turbulence intensity (TI) from the TKE. TI normalizes the velocity fluctuation variance by the mean velocity:

$$TI = 100 \times \frac{\sqrt{2TKE}}{\sqrt{\bar{u}^2 + \bar{v}^2 + \bar{w}^2}} \tag{3.22}$$

CHAPTER IV

RESULTS AND DISCUSSION

4.1 Phase Filtering

The identification and replacement of spikes within the data sets through phase filtration was one technique used to improve data quality. The effects of this procedure are illustrated in Figures 4.1, 4.2, and 4.3. "No Phase Filtering" indicates calculations performed before phase filtration. "Including interpolated" indicates post-phase filtration calculations with all points included. "Unflagged only" calculations were performed only on points that were not flagged as spikes.

Because the number of replaced points in most sets was fairly small (see Table 3.3), changes in the mean velocity were small in almost all data sets (Figures 4.1 and 4.2). The mean velocity in these figures corresponds to averaging over each burst and averaging among the bursts in the set. In contrast, the estimates of turbulence quantities are affected by the phase filter as demonstrated by the decrease in TKE (Figure 4.3). The extreme samples flagged, and either replaced by interpolation or removed, contribute to inflated estimates of TKE. Of particular note is the change for the Herb14 data set, where the TKE changed from 0.039 m^2/s^2 to 0.0024 m^2/s^2 (not shown in Figure 4.3). The bandedness of some bursts in the data set resulted in a dramatic overestimation of the TKE for this set, and illustrates the importance of phase filtration. Even for those sets without banding, the DMHside16 and House16 sets see a noticeable decrease in TKE after phase filtration.

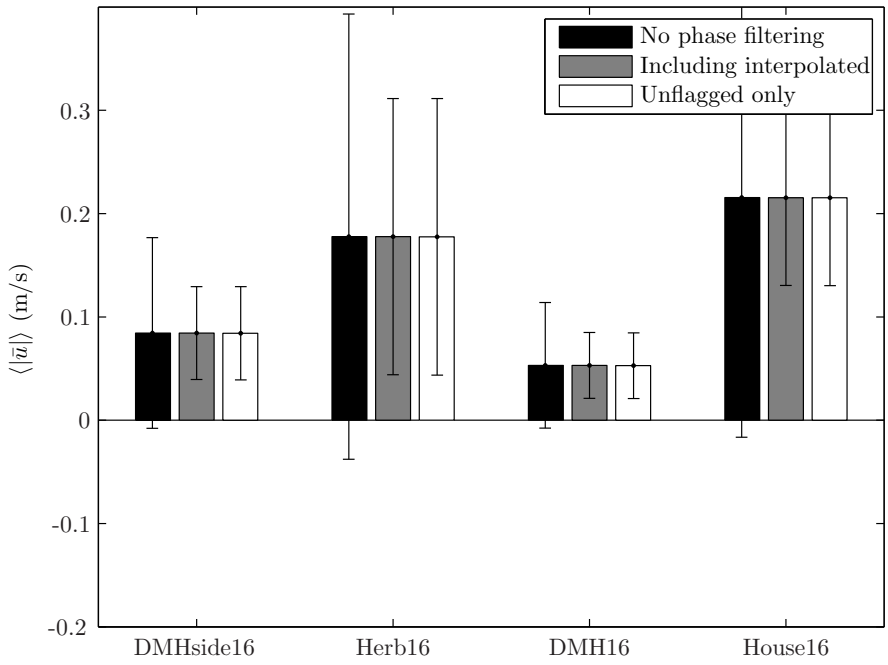

Figure 4.1: Comparison of $\langle \bar{u} \rangle$ for steps along the phase filtration process. "No phase filtering" indicates the pre-filtered data, "Including interpolated" indicates inclusion of the interpolated data points, and "Unflagged only" indicates exclusion of interpolated data points. The error bars indicate the standard deviation of the burst mean values. Presented sets were collected on 5-16-07.

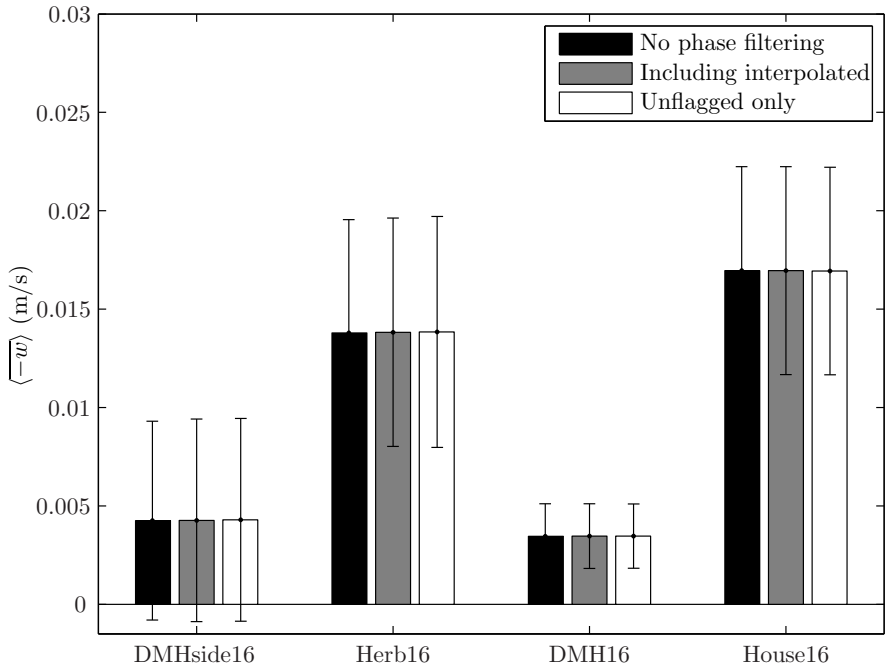

Figure 4.2: Comparison of $\langle -\bar{w} \rangle$ for steps along the phase filtration process. "No phase filtering" indicates the pre-filtered data, "Including interpolated" indicates inclusion of the interpolated data points, and "Unflagged only" indicates exclusion of interpolated data points. The error bars indicate the standard deviation of the burst mean values. Presented sets were collected on 5-16-07.

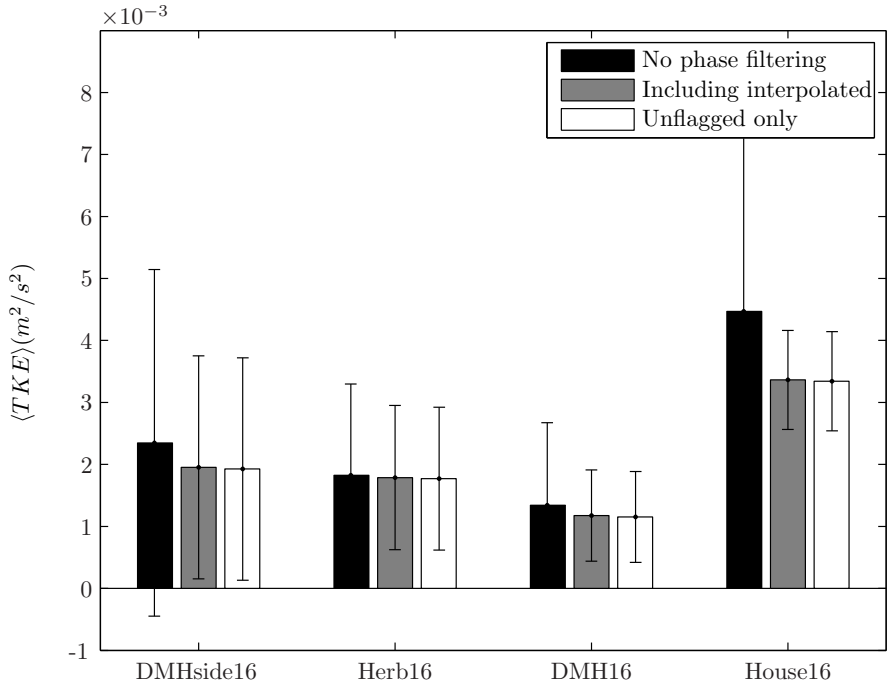

Figure 4.3: Comparison of TKE values for steps along the phase filtration process. "No phase filtering" indicates the pre-filtered data, "Including interpolated" indicates inclusion of the interpolated data points, and "Unflagged only" indicates exclusion of interpolated data points. The error bars indicate the standard deviation of the burst mean values. Presented sets were collected on 5-16-07.

4.2 Wave Removal

The results of the wave removal procedure can be seen in Table 4.1. In general, the average wave contribution to TKE or Reynolds shear stress in a data set was around an order of magnitude less than the final computed value. For the DMHside16 and DHM16 data sets, however, the wave contribution to TKE accounted for more than half of the apparent TKE. For some of the Skidaway14 and House16 data sets, addressing nonphysical results (see Section 3.3.3.1) resulted in an increase in the mean burst-average shear stress. This can occur if the wave contribution is greater for negative apparent Reynolds shear stress than for positive apparent Reynolds shear stress. The set means would then see a preferential shift towards a larger overall value. Physically, this would correspond to the situation where negative Reynolds shear stress was correlated with higher proportional absolute values of wave contribution.

While the wave associated components of TKE are generally the same across the sets with the exception of the DMHside16 and DMH16 sets, the same cannot be said for the burst-average Reynolds shear stress. The Reynolds shear stress increases in value by small (8.9%, House16) or large (121.5%, Skidaway14) amounts, while in others it decreases by small (1.0%, Wilmington14) or large (85%, Herb16) amounts. Additionally, the occurence of wave contributions that were greater and sometimes opposite in sign than the total $\overline{(u-\bar{u})(w-\bar{w})}$ indicate some problems with the wave removal process for Reynolds shear stress computation (see Section 3.3.3.1). The source of these problems could be the computation of two power spectra (PSDs) and two fast Fourier transforms (FFTs) for each burst. Noise in the power spectrum (see Figure 3.7) and FFTs for each velocity component are then combined together and could be responsible for the volatility in the wave-removed Reynolds shear stresses. Due to the lack of confidence in the calculations, the wave contribution to the burst-avereage Reynolds shear stress will not be removed, and the apparent, phase-filtered

$\overline{(u-\bar{u})(w-\bar{w})}$ will be presented as Reynolds shear stress.

Table 4.1: Comparison of TKE and Reynolds shear stress before and after wave removal. PF indicates result based on phase-filtered fluctuations, and WR indicates the value after wave removal.

Set Name	$\langle$TKE PF$\rangle$ (m^2/s^2)	$\langle$TKE WR$\rangle$ (m^2/s^2)	% Decrease	$\langle\overline{u'w'}\rangle$ PF (m^2/s^2)	$\langle\overline{u'w'}\rangle$ WR (m^2/s^2)	% Decrease
Herb14	2.41E-03	2.06E-03	15.9	-2.07E-05	-1.33E-05	35.6
Wilmington14	3.70E-03	2.86E-03	22.7	-4.13E-04	-4.09E-04	1.0
Skidaway14	7.09E-04	6.27E-04	11.6	1.63E-06	3.60E-06	-121.5
Moon14	1.57E-03	1.29E-03	17.7	4.27E-05	2.89E-05	32.3
DHMside16	1.93E-03	8.75E-04	54.6	-6.58E-05	-4.43E-05	32.7
Herb16	1.77E-03	1.42E-03	19.5	-6.09E-06	-8.83E-07	85.5
DMH16	1.15E-03	4.91E-04	57.4	1.56E-05	9.34E-06	40.0
House16	3.34E-03	2.87E-03	14.2	9.50E-05	1.03E-04	-8.9
Herb19	1.42E-03	1.23E-03	13.9	-4.60E-05	-3.70E-05	19.6
Skidaway19	9.19E-04	7.53E-04	18.1	5.28E-05	4.00E-05	24.2
Wilmington19	1.41E-03	1.15E-03	18.3	-1.77E-04	-1.46E-04	17.6
Skidaway20	1.56E-03	1.35E-03	13.3	6.53E-05	5.85E-05	10.4

4.3 Individual Burst Behavior

The properties of a single burst of data are examined in this section. Figure 4.4 presents the three velocity time series for the 20^{th} burst of the DMHside16 data set, a burst exhibiting a large wave influence. Any points that were flagged in the phase filtering process are excluded from the plot. As described in Chapter 3, the raw horizontal velocity components have been rotated to maximize the magnitude of mean u velocity and minimize the magnitude of mean v velocity. For this burst, the u component has a mean value of 1.86×10^{-2} m/s and standard deviation of 3.85×10^{-2} m/s. The other components are $\bar{v} = -2.11 \times 10^{-4} \pm 2.33 \times 10^{-2}$ m/s and $\bar{w} = -1.28 \times 10^{-3} \pm 2.49 \times 10^{-2}$ m/s (mean $\pm$ standard deviation). The TKE for this burst is 6.73×10^{-4} (m^2/s^2) and the wave contribution is 6.46×10^{-4} (m^2/s^2). The Reynolds shear stress is -4.32×10^{-5} (m^2/s^2) and the wave contribution is -4.53×10^{-5} (m^2/s^2). The TI for this burst is 196.5%.

Figure 4.5 contains the power spectra for time records shown in Figure 4.4. The wave influence is seen primarily in the peak of the u power spectral density (PSD) at approximately 0.3 Hz. Smaller peaks are also evident in the v and w PSDs.

4.4 Data Set Behavior

This section presents burst-average records for each data set. Burst-average quantities for each set are computed for the first full tidal cycle, defined as a period roughly half of a day in length, in which data quality parameters indicated the probe was submerged. Individual bursts within a tidal cycle may be excluded if they did not meet data quality thresholds. Because of the nature of the ADV placement, two flow regimes are usually apparent in each set. The first half of the time series occurs during the rising tide, while the second half corresponds to the falling tide. In order

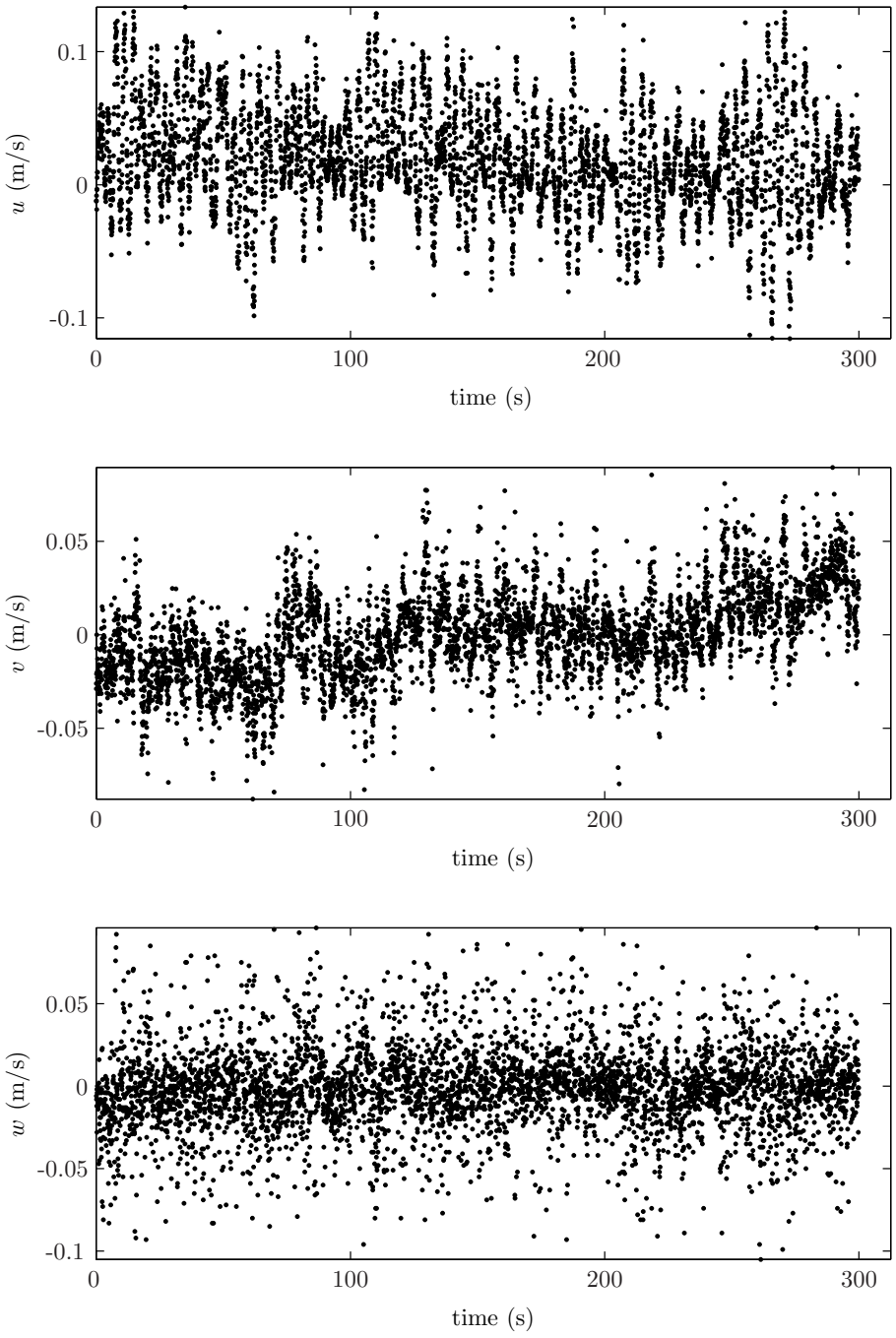

Figure 4.4: Velocity time series for the 20$^{\text{th}}$ burst of the DMHside16 data set. Samples flagged in the phase filtering process are not plotted.

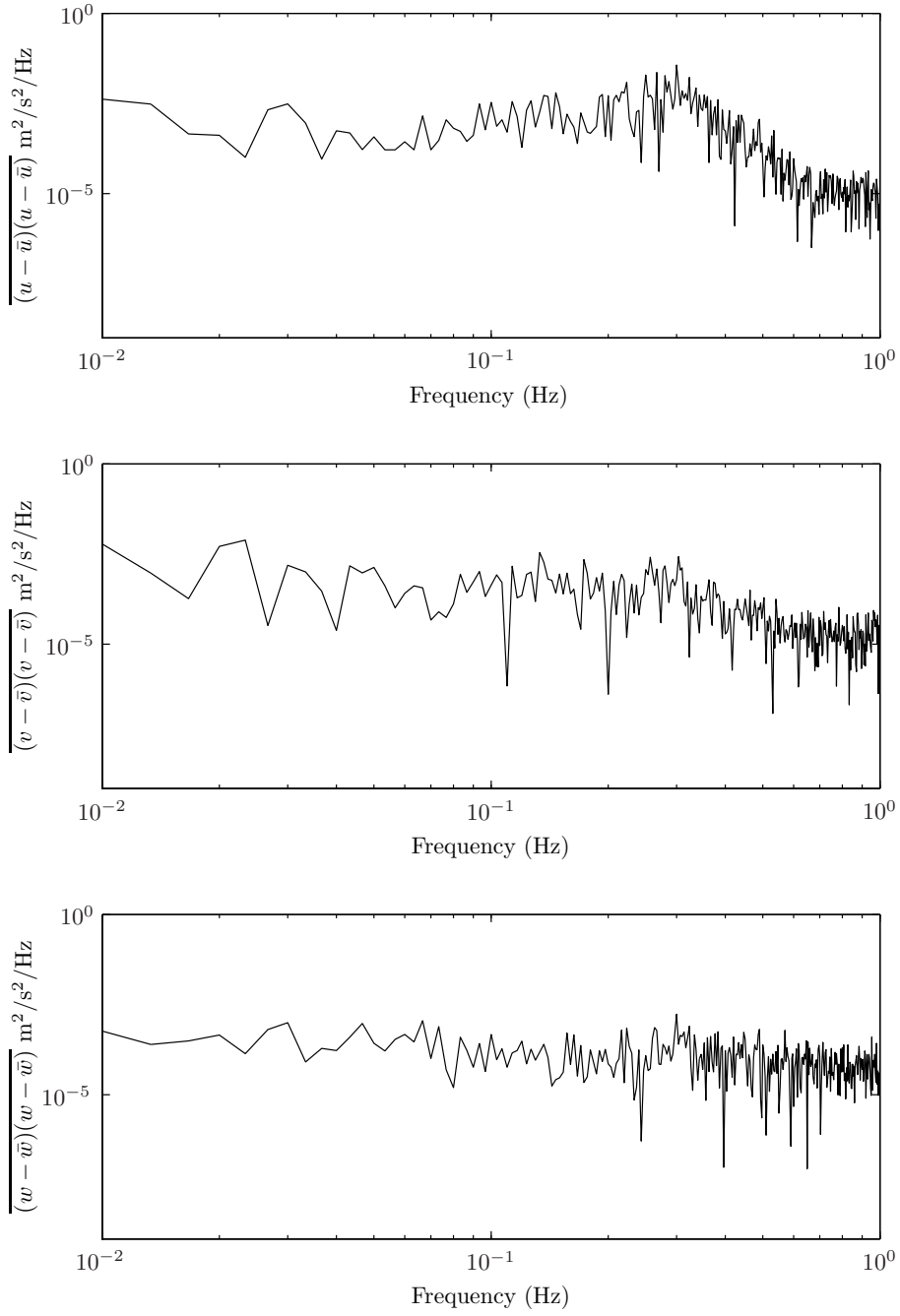

Figure 4.5: Power spectra of the individual velocity components for the 20$^{\text{th}}$ burst of the DMHside16 data set.

to illustrate the effect of rotating each burst within a set individually, plots of rotation angle variation in time are given for the Wilmington14 and Moon14 sets (see Figures 4.8 and 4.11). The behaviors presented in these two sets are charateristic of the other data sets with respect to rotation angle variability in time.

4.4.1 Data Collected on 5/14/07

4.4.1.1 Herb14 Data Set

Figure 4.6 presents the records for the Herb14 data set. The burst-average values of horizontal velocity have a mean of $1.13 \times 10^{-1} \pm 2.03 \times 10^{-1}$ m/s (mean $\pm$ standard deviation of the burst-average values), with a maximum value of 3.99×10^{-1} m/s at 133.75 year-days and a maximum negative value of -4.19×10^{-1} at 133.90 year-days. The velocity is small (near zero) around 133.82 year-days, which indicates the high tide portion of the time series. The burst-average values of vertical velocity are small and variable ($-4.64 \times 10^{-3} \pm 6.65 \times 10^{-3}$ m/s). The burst-average value of vertical velocity changes sign from positive for the incoming tide to negative for the outgoing tide. TKE peaks in the outgoing tide at 5.70×10^{-3} m^2/s^2 at 133.93 year-days, corresponding with the maximum negative $\bar{u}$ value. Reynolds shear stress is small ($-1.33 \times 10^{-5} \pm 1.50 \times 10^{-4}$ m^2/s^2) and reaches a maximum of 4.91×10^{-4} m^2/s^2 at 133.89 year-days peaking at the same time the horizontal velocity is approaching a maximum negative value in the outgoing tide.

4.4.1.2 Wilmington14 Data Set

Figure 4.7 contains the records for the Wilmington14 data set. The mean of the burst-average horizontal velocity ($1.02 \times 10^{-1} \pm 3.23 \times 10^{-1}$ m/s) is larger in magnitude during the incoming tide, with a maximum of 5.08×10^{-1} m/s at 133.71 year-days and

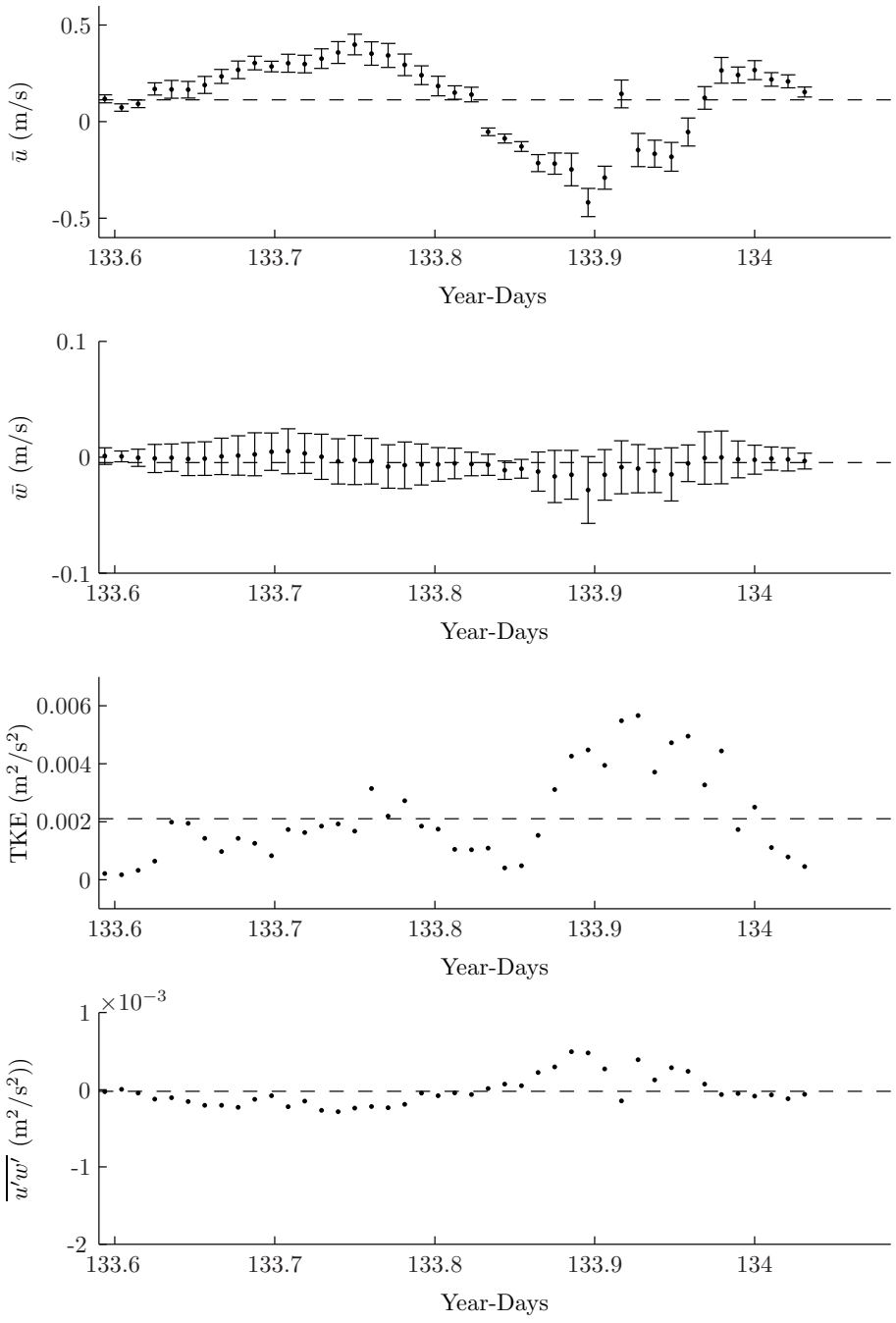

Figure 4.6: Burst-average records for Herb14 data set. The dashed line indicates the mean of the burst-average values. The error bars in the burst-average velocity plots correspond to standard deviation.

a maximum negative value of -3.40×10^{-1} m/s at 133.93 year-days. Burst-average vertical velocities ($-9.58 \times 10^{-3} \pm 3.65 \times 10^{-2}$ m/s) are negative for the incoming tide and change signs following high tide around 133.82 year-days. Both TKE and Reynolds shear stress have maximum absolute values during the incoming tide around 133.80 year-days and the Reynolds shear stress also has large magnitudes during the outgoing tide around 133.92 year-days.

Figure 4.8 contains the rotation angle Θ for the Wilmington14 set. Here the rotation angle is positive (around $\pi/4$) for the incoming tide, close to zero as high tide approaches, and then negative (around $\pi/8$) for the outgoing tide. This variability could be ascribed to the positioning of the probe in the Wilmington River, combined with different flow direction during the incoming and outgoing tides. Asymmetric behavior of this type was also seen in the rotation angles for a few of the other data sets (not presented).

4.4.1.3 Skidaway14 Data Set

Figure 4.9 contains the records for the Skidaway14 data set. The burst-average values of horizontal velocity ($3.11 \times 10^{-2} \pm 1.45 \times 10^{-1}$ m/s) exhibit unusual "lull" periods. For instance, around 133.73 year-days the $\bar{u}$ velocity in the Wilmington14 data set (Figure 4.7) is at a maximum value (characteristic of a rising tide), while the Skidaway14 $\bar{u}$ is close to zero. A similar phenomenon is observed around 133.95 year-days. Aside from this period of small burst-average horizontal velocity, the set exhibits normal tidal behavior, with $\bar{u}$ values approaching zero from either side of the high tide occurring at approximately 133.88 year-days. The TKE for the Skidaway14 set peaks from 133.80 to 133.87 year days, which corresponds to an elevated period of u velocity in the set. The burst-average values of vertical velocity ($-5.16 \times 10^{-3} \pm 5.85 \times 10^{-3}$) and Reynolds shear stress ($-3.77 \times 10^{-6} \pm 4.83 \times 10^{-5}$) remain small throughout the

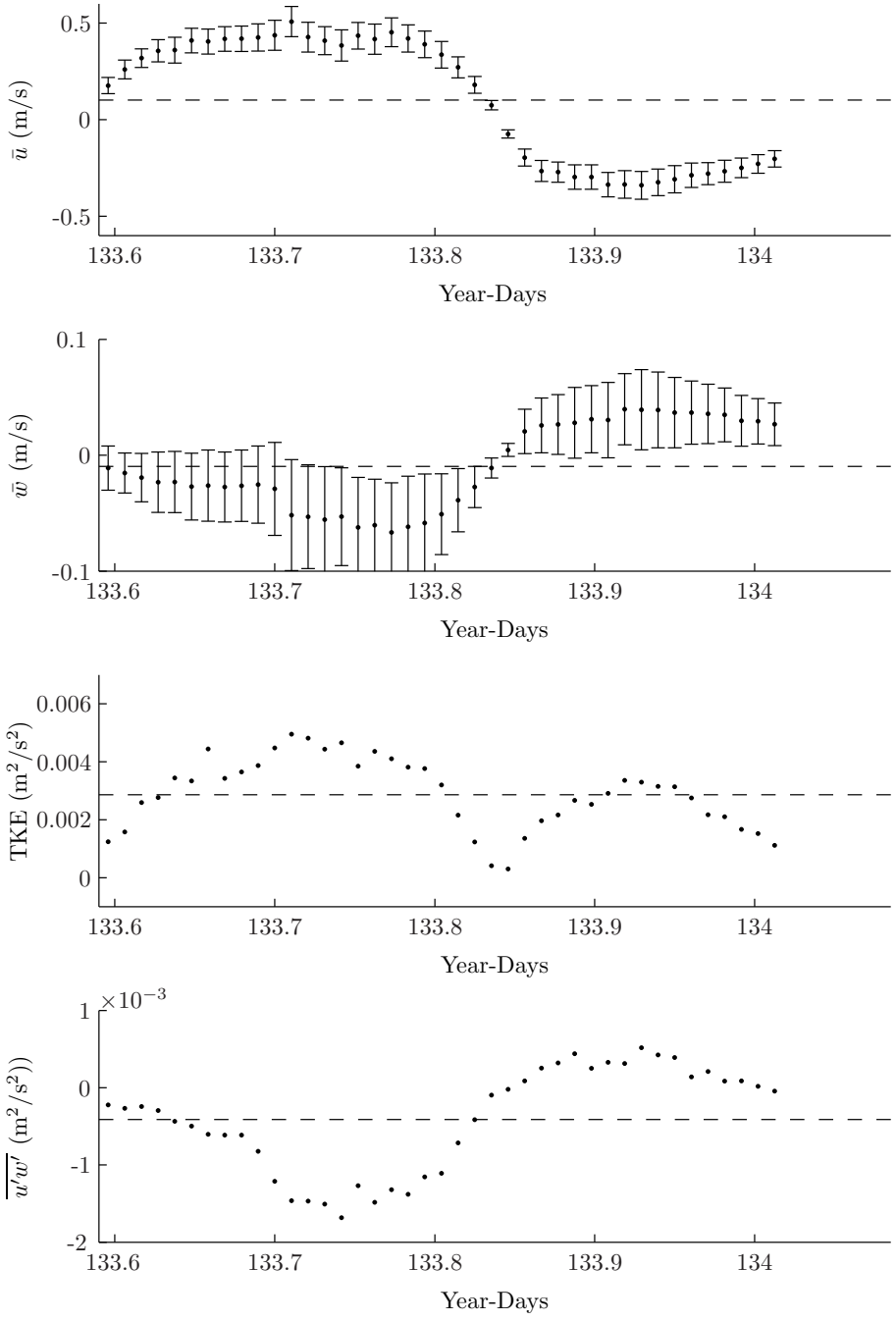

Figure 4.7: Burst-average records for Wilmington14 data set. The dashed line indicates the mean of the burst-average values. The error bars in the burst-average velocity plots correspond to standard deviation.

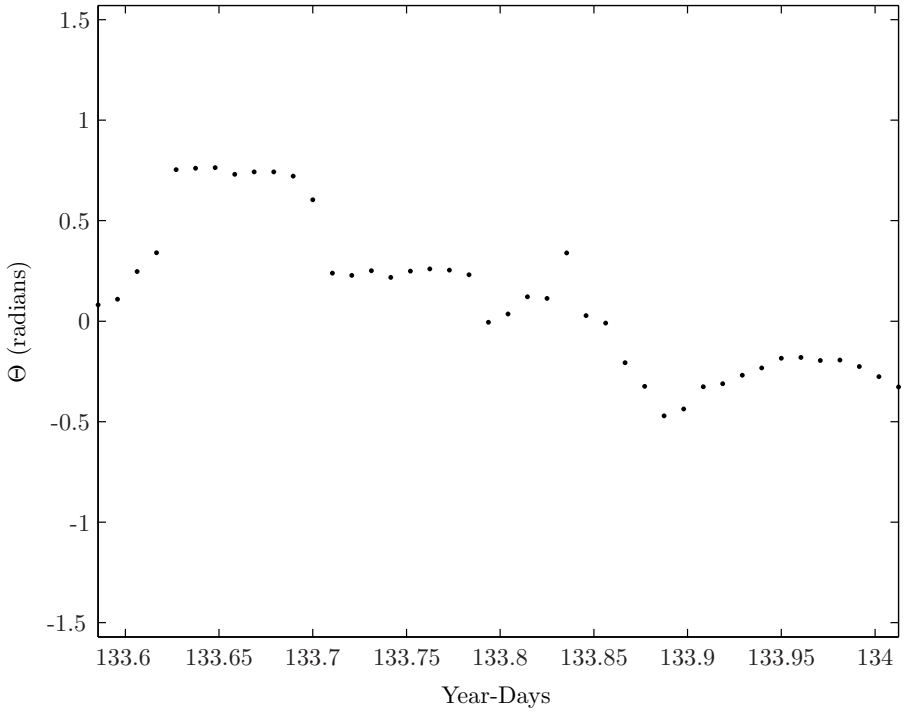

Figure 4.8: Rotation angle Θ for Wilmington14 data set.

data set.

4.4.1.4 Moon14 Data Set

Figure 4.10 contains the records for the Moon14 data set. The set exhibits a two-cycle record of burst-average horizontal velocity, with high tide occurring around 133.90 year-days. The values of burst-average horizontal velocity are positive for the incoming tide (maximum of 3.77×10^{-1} m/s at 133.70 year-days) and negative for the outgoing tide (maximum negative value of -4.65×10^{-1} m/s at 133.92 year-days). The burst-average vertical velocity values are positive for the incoming tide with a maximum of 2.58×10^{-2} m/s at 133.70 year-days (matching the time of maximum $\bar{u}$ velocity) and negative for the outgoing tide with a maximum negative value of -2.35×10^{-2} m/s at 133.87 year-days. TKE is greatest in the middle of the outgoing tide around 133.93 year-days, concurrent with the maximum negative value of $\bar{u}$

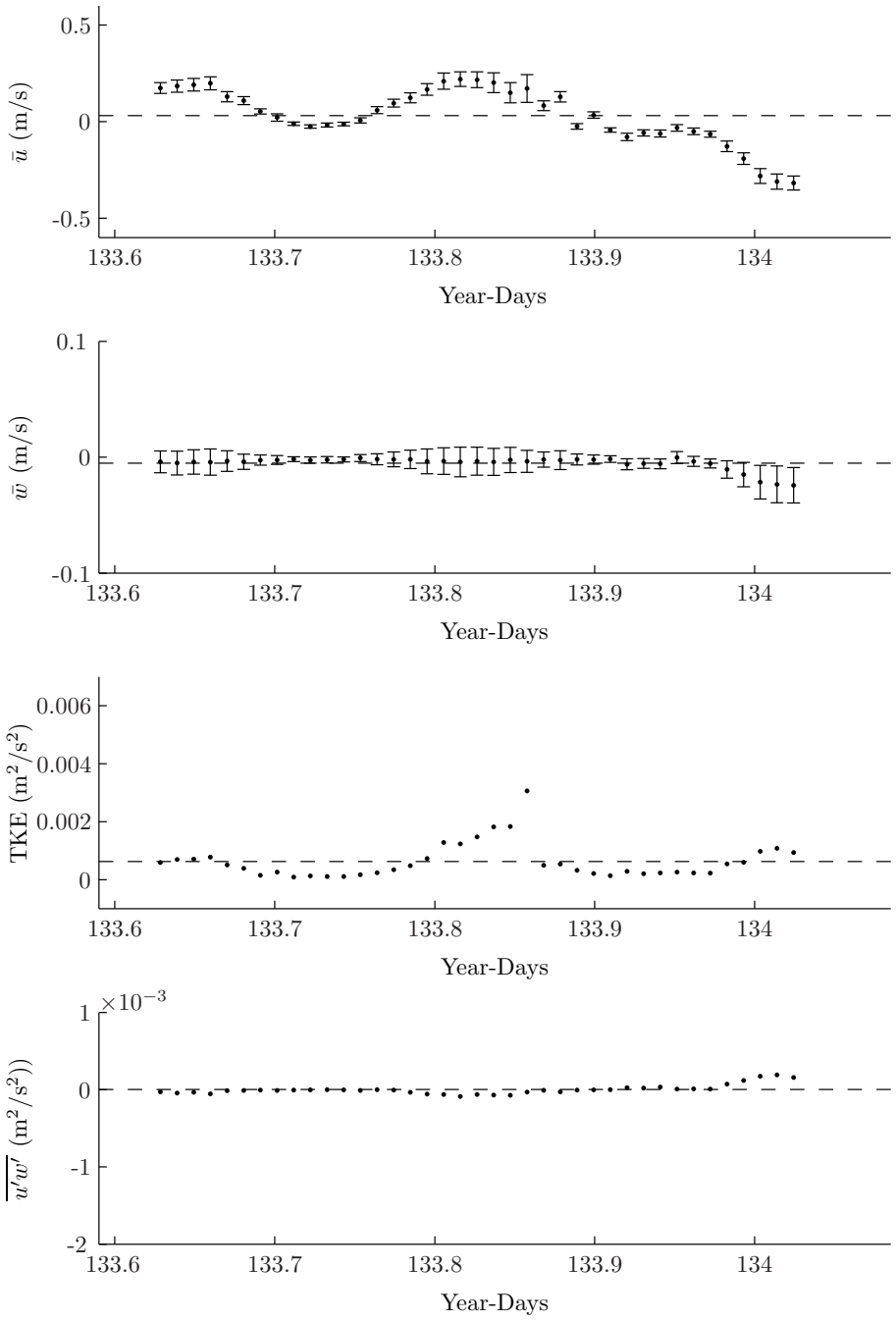

Figure 4.9: Burst-average records for Skidaway14 data set. The dashed line indicates the mean of the burst-average values. The error bars in the burst-average velocity plots correspond to standard deviation.

velocity. The magnitude of the Reynolds shear stress also is greatest during the periods of largest velocity.

Figure 4.11 contains the rotation angle Θ for the Moon14 set. Here the rotation angle remains small during the incoming tide varying between approximately 0.1 and 0.2 radians. The only major deviation occurs near the high tide at 133.84 year-days, where the large rotation angle is likely due to the slowing of the dominant tidal current. After the deviation, the rotation angle remains small and close to that of the incoming tide, ranging from approximately -0.1 to 0.1 radians. The relatively small variation in rotation angle, except when the tidal flow is slowing, is charactertistic of the rotation angles for sets that do no behave in the asymmetric way shown in the Wilmington14 set case (see Figure 4.11).

4.4.2 Data Collected on 5/16/07

4.4.2.1 DMHside16 Data Set

Figure 4.12 contains the records for the DMHside16 data set. For the outgoing tide, the burst-average values of horizontal velocity reach a negative maximum shortly after high tide (-1.81×10^{-1} m/s at 135.91 days) and then approach zero. The burst-average values of vertical velocity have a small mean ($-4.29 \times 10^{-3} \pm 5.16 \times 10^{-3}$ m/s) but exhibit large within-burst variability. TKE values are slightly elevated on either side of the high tide period (around 135.88 year-days) and at the beginning and end of the set, but TKE generally stays close to the mean of -8.75×10^{-4} m^2/s^2. The Reynolds shear stress is greatest at the beginning of the data set and remain close to the mean.

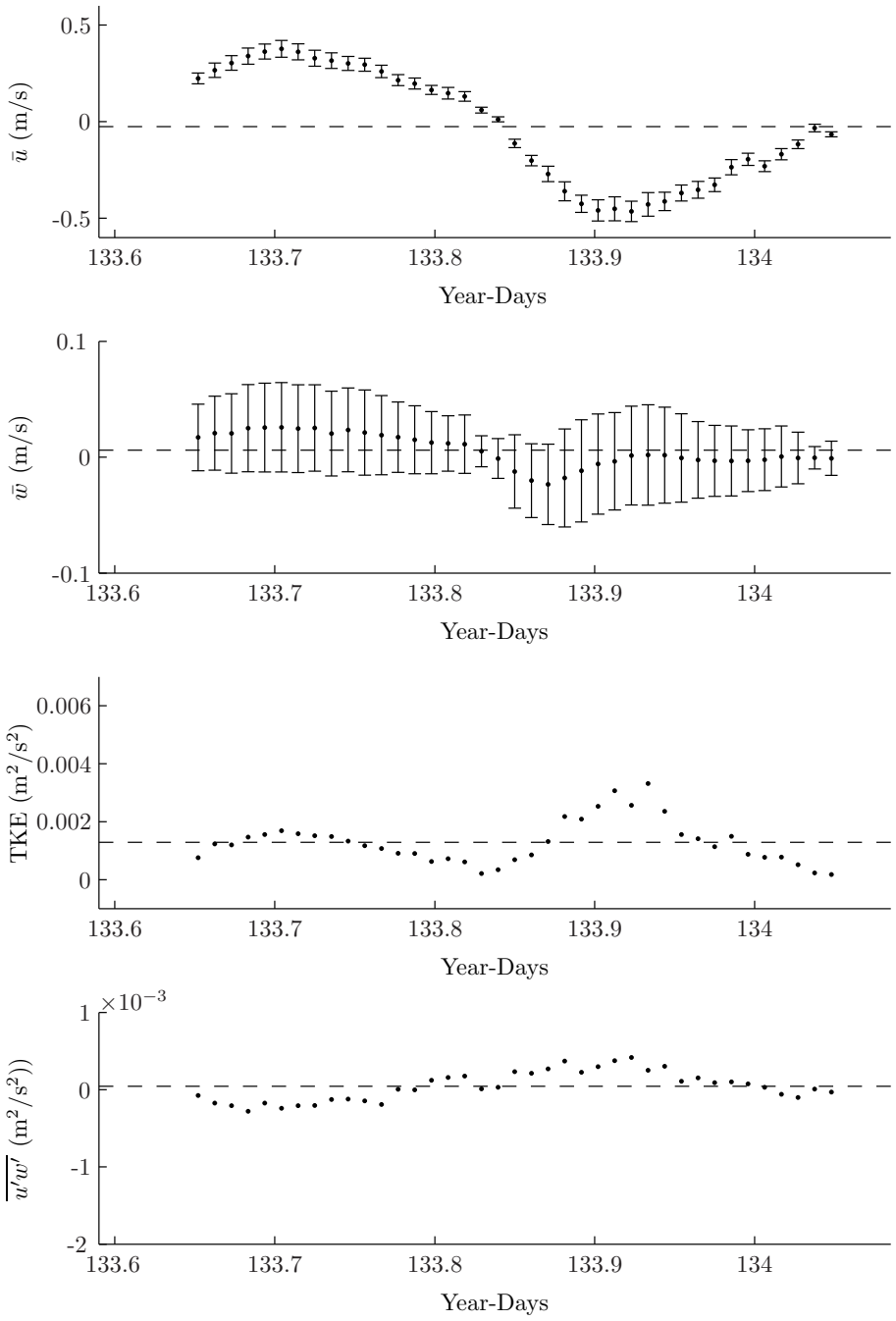

Figure 4.10: Burst-average records for Moon14 data set. The dashed line indicates the mean of the burst-average values. The error bars in the burst-average velocity plots correspond to standard deviation.

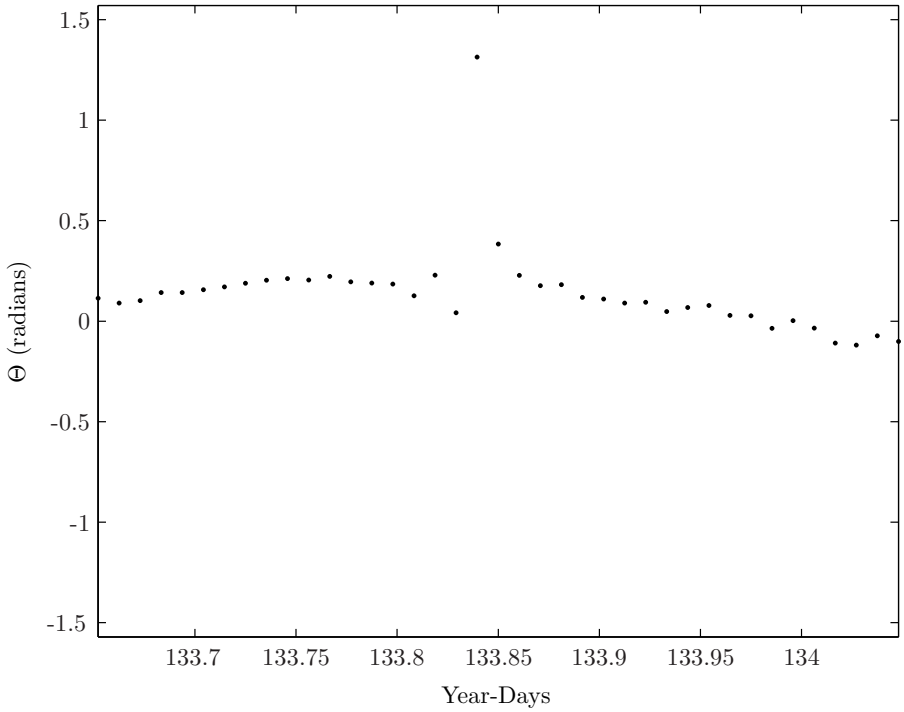

Figure 4.11: Rotation angle Θ for Moon14 data set.

4.4.2.2 Herb16 Data Set

Figure 4.13 contains the records for the Herb16 data set. The burst-average values of horizontal velocity are larger during the incoming tide (maximum of 4.69×10^{-1} m/s at 135.79 year-days) than in the outgoing tide (maximum negative value of -1.59×10^{-1} m/s at 135.99). The burst-average values of vertical velocity are primarily negative throughout and the variance within bursts is large, especially during the rising tide. TKE and Reynolds shear stress are similar for both tides, peaking both before and after the high tide at approximately 135.87 year-days. While the maximum TKE value occurs during the outgoing tide (3.40×10^{-3} m^2/s^2 at 135.95 year-days), a sustained period of large TKE occurs from 135.76 to 135.84 year days, corresponding to the large $\bar{u}$ value during the incoming tide. The Reynolds shear stress magnitude is smaller for the incoming tide (-4.82×10^{-4} m^2/s^2 at 135.93 year-days) relative to the incoming tide (-7.33×10^{-4} m^2/s^2 at 135.79 year-days).

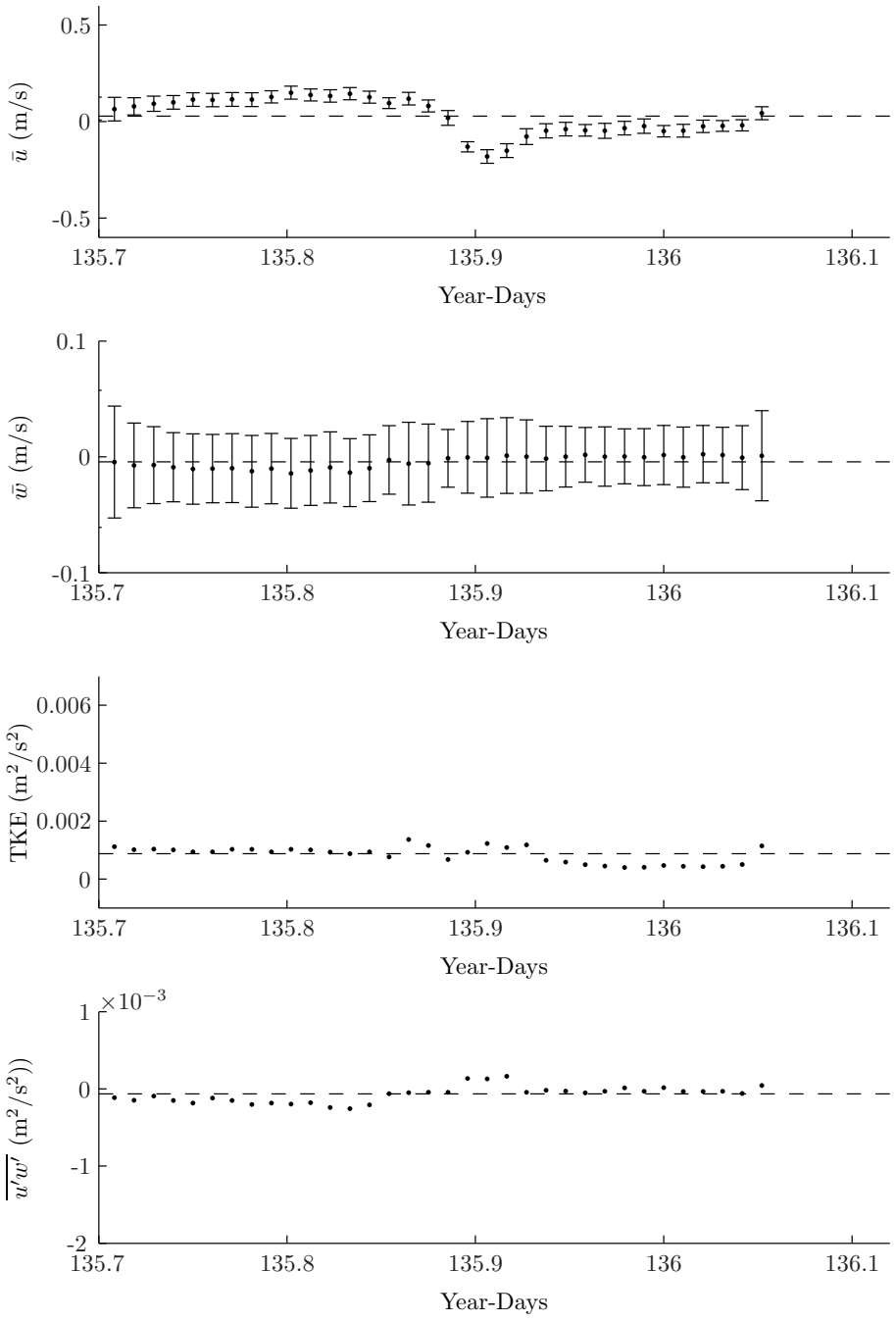

Figure 4.12: Burst-average records for DMHside16 data set. The dashed line indicates the mean of the burst-average values. The error bars in the burst-average velocity plots correspond to standard deviation.

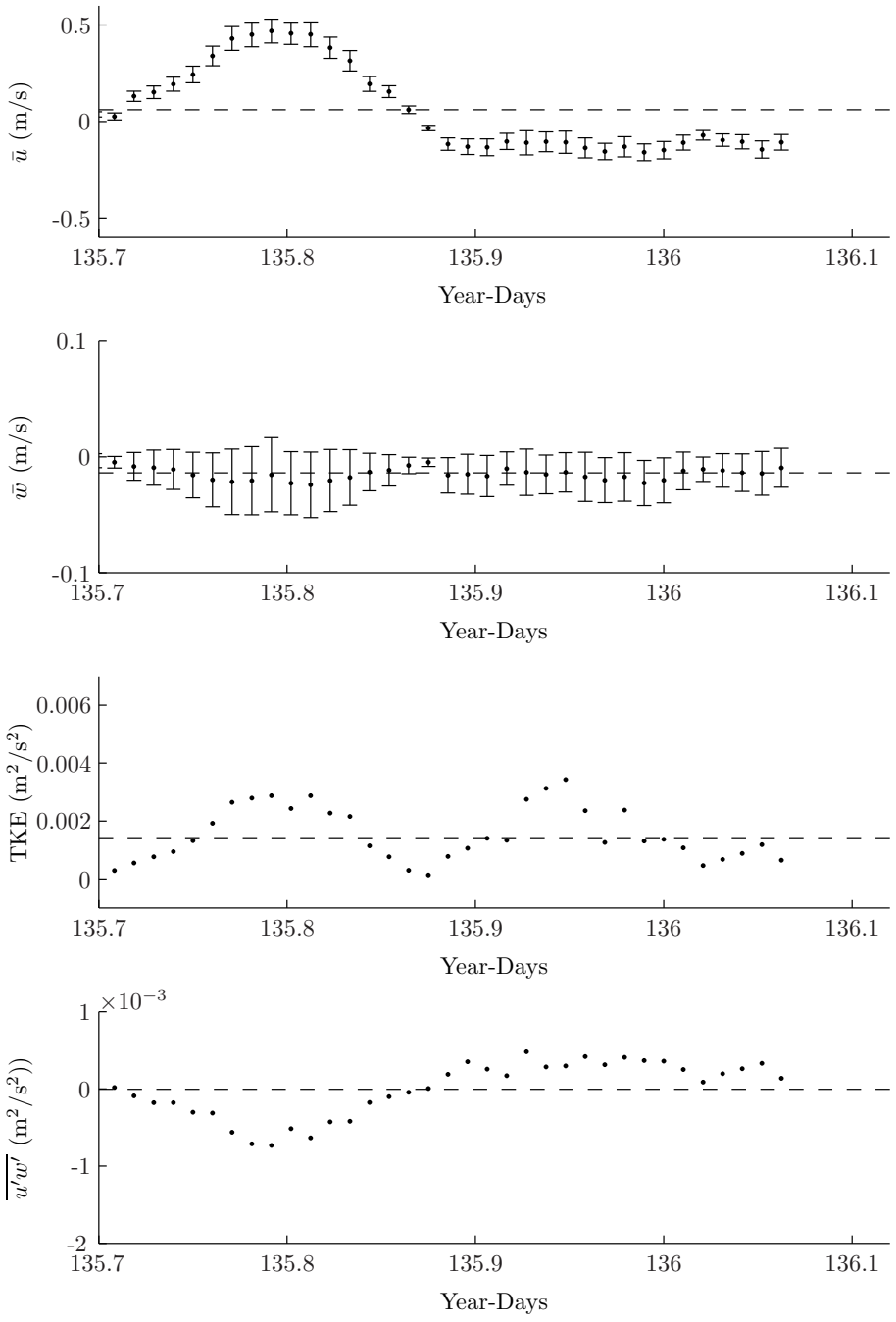

Figure 4.13: Burst-average records for Herb16 data set. The dashed line indicates the mean of the burst-average values. The error bars in the burst-average velocity plots correspond to standard deviation.

4.4.2.3 DMH16 Data Set

Figure 4.14 contains the records for the DMH16 data set. The burst-average values of horizontal velocity fluctuate and remain small with a mean of $-1.50 \times 10^{-2} \pm 6.04 \times 10^{-2}$ m/s and don't appear to exhibit strong tidal dependence. The burst-average values of vertical velocity ($-3.47 \times 10^{-3} \pm 1.63 \times 10^{-3}$ m/s) are primarily small and negative. TKE and Reynolds shear stress also do not strongly exhibit tidal tendencies since they remain close to the average value throughout.

4.4.2.4 House16 Data Set

Figure 4.15 contains the records for the House16 data set. The burst-average values of horizontal velocity are greatest during the incoming tide (3.70×10^{-1} m/s at 135.79 year-days), and do not reach a comparable maximum negative value as the tide recedes (-2.43×10^{-1} m/s at 135.98 year-days). The burst-average values of vertical velocity are small, primarily negative, and possess large variance within the bursts. TKE doesn't exhibit a strong tidal influence as all values are close to the set mean of 2.87×10^{-3} m^2/s^2. Reynolds stress is minimum as high tide approaches (-5.52×10^{-4} m/s at 135.79 year-days) and maximum during the receding tide (7.00×10^{-4} m/s at 135.99 year-days).

4.4.3 Data Collected on 5/19/07

4.4.3.1 Herb19 Data Set

Figure 4.16 contains the records for the Herb19 data set. The burst-average values of horizontal velocity magnitude are larger during the outgoing tide (negative maximum of -3.60×10^{-1} m/s at 139.13 year-days) than in the incoming tide (maximum value of 3.11×10^{-1} m/s at 138.88 year-days). The burst-average values of vertical velocity

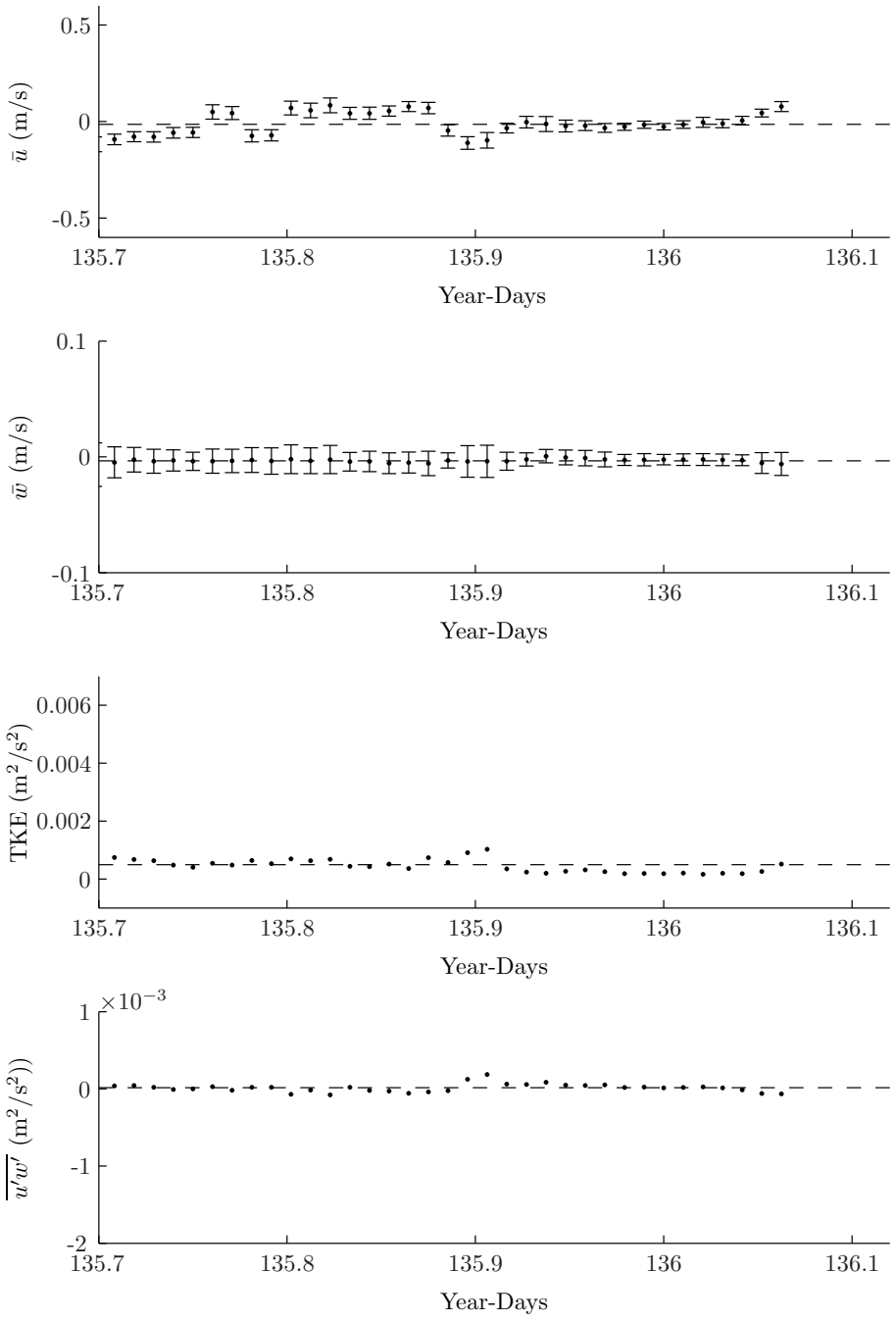

Figure 4.14: Burst-average records for DMH16 data set. The dashed line indicates the mean of the burst-average values. The error bars in the burst-average velocity plots correspond to standard deviation.

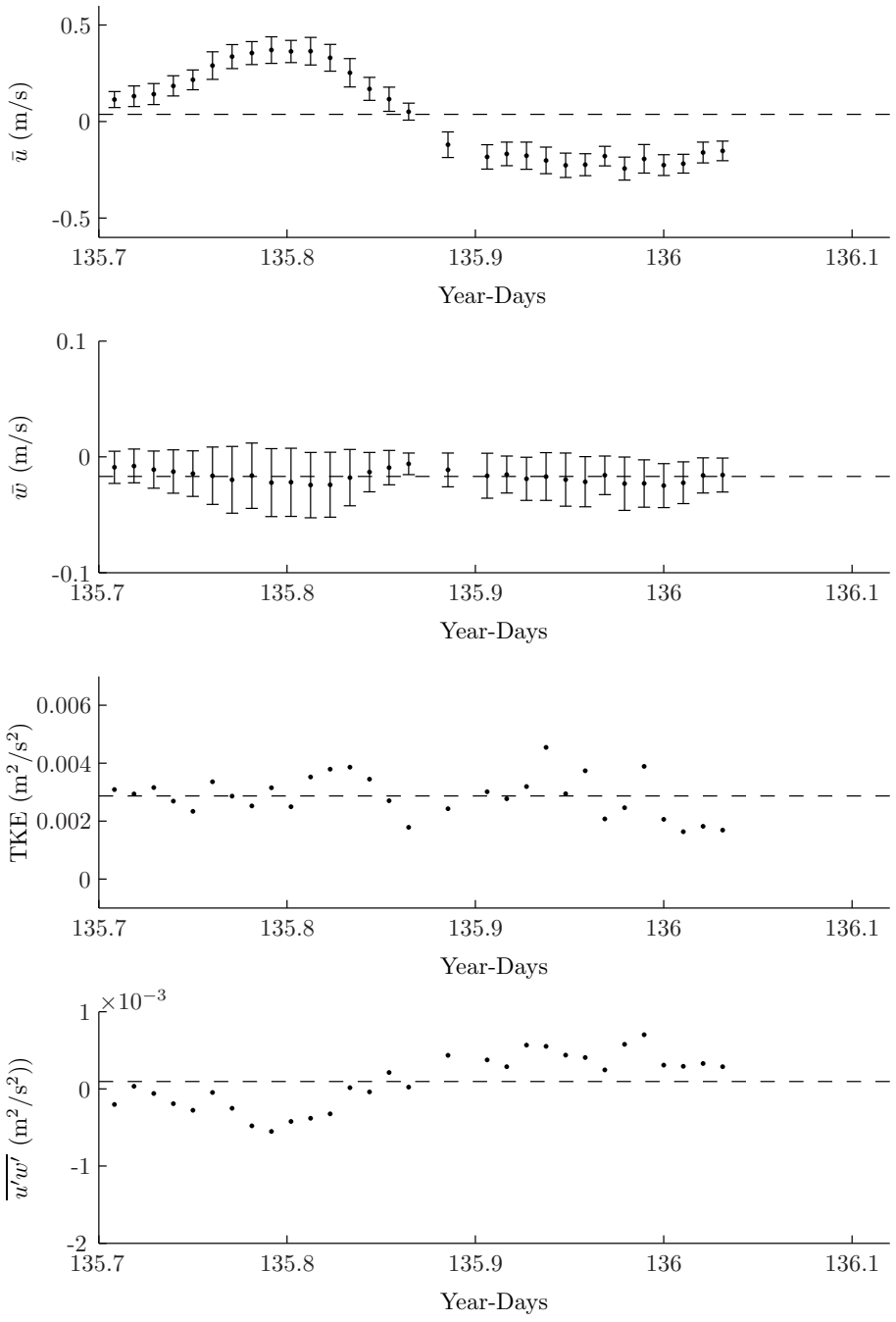

Figure 4.15: Burst-average records for House16 data set. The dashed line indicates the mean of the burst-average values. The error bars in the burst-average velocity plots correspond to standard deviation.

are relatively small, primarily negative, and fluctuate around a mean of $-9.99 \times 10^{-3} \pm 4.18 \times 10^{-3}$ m/s. TKE is greatest around 139.12 year-days. The Reynolds shear stress does not deviate far from the mean of -4.60×10^{-5} m^2/s^2.

4.4.3.2 Skidaway19 Data Set

Figure 4.17 contains the records for the Skidaway19 data set. The burst-average values of horizontal velocity are largest during the receding tide portion of the time series (negative maximum of -3.55×10^{-1} m/s at 139.13 year-days). The burst-average values of vertical velocity steadily decrease in magnitude over the course of the entire tidal cycle. TKE is greatest between 139.07 and 139.17 year-days, when the maximum $\bar{u}$ velocity occurs. The Reynolds shear stress is also greatest in magnitude in this period, reaching a value of 5.02×10^{-4} m^2/s^2 at 138.79 year-days.

4.4.3.3 Wilmington19 Data Set

Figure 4.18 contains the records for the Wilmington19 data set. The burst-average values of horizontal velocity magnitude are larger during the incoming tide (maximum value of 3.22×10^{-1} m/s at 138.88 year-days) than in the outgoing tide (maximum of -2.15×10^{-1} m/s at 139.05). The burst-average values of vertical velocity are negative for all bursts and don't vary significantly from the mean value of -1.25×10^{-2}. The incoming tide TKE and Reynolds shear stress behave similarly to the $\bar{u}$ velocity. As the tide recedes the TKE increases and decreases multiple times.

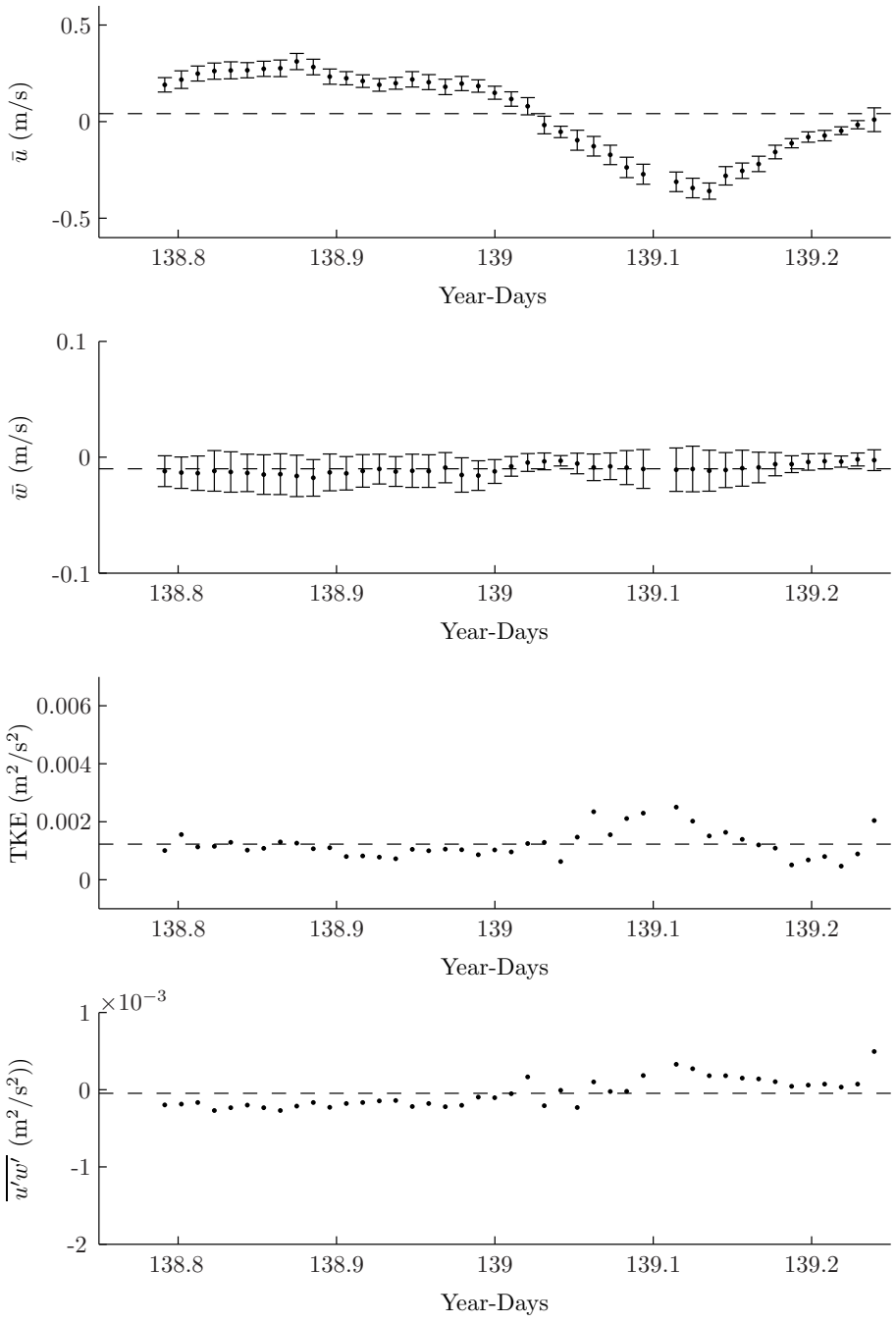

Figure 4.16: Burst-average records for Herb19 data set. The dashed line indicates the mean of the burst-average values. The error bars in the burst-average velocity plots correspond to standard deviation.

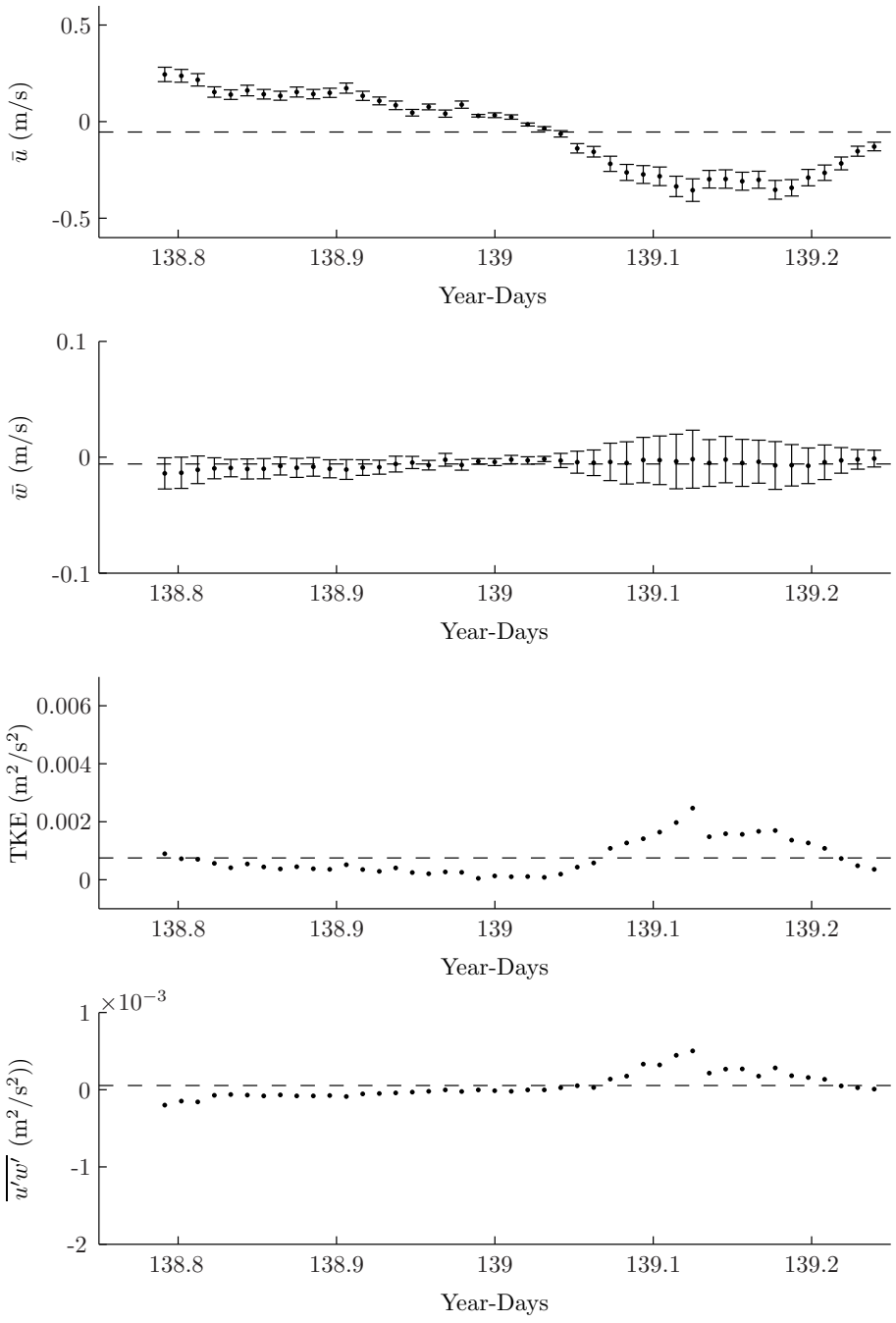

Figure 4.17: Burst-average records for Skidaway19 data set. The dashed line indicates the mean of the burst-average values. The error bars in the burst-average velocity plots correspond to standard deviation.

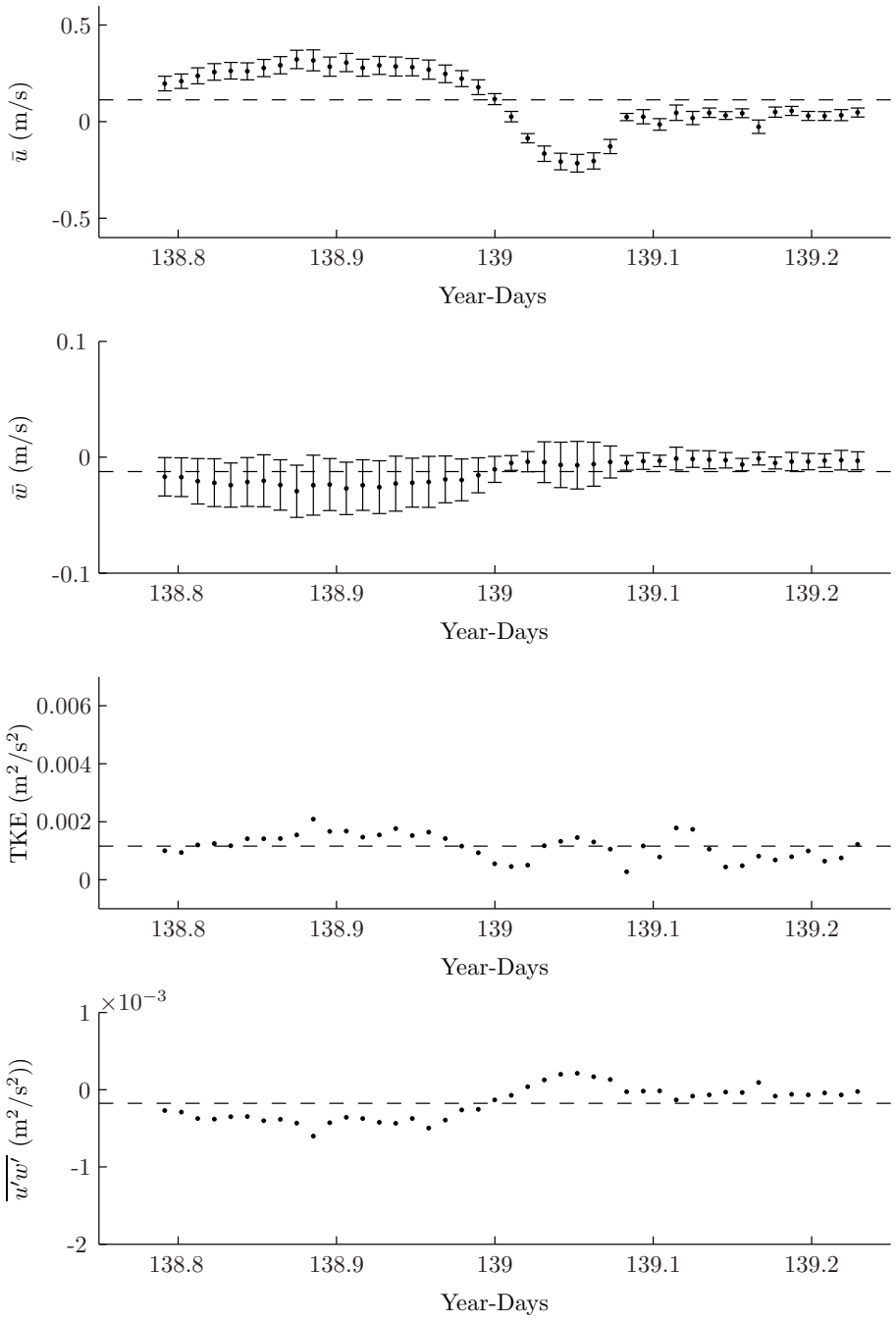

Figure 4.18: Burst-average records for Wilmington19 data set. The dashed line indicates the mean of the burst-average values. The error bars in the burst-average velocity plots correspond to standard deviation.

4.4.4 Data Collected on 5/20/07

4.4.4.1 Skidaway20 Data Set

Figure 4.19 contains the records for the Skidaway20 data set. The burst-average values of horizontal velocity magnitude are largest during the receding tide, reaching a maximum negative value of -3.31×10^{-1} m/s at 140.17 year-days. The burst-average values of vertical velocity are negative and also greatest during the receding tide, with the maximum negative value of -3.36×10^{-2} m/s occurring at 140.21 year-days. Both TKE (5.81×10^{-3} m^2/s^2 at 140.13 year-days) and Reynolds shear stress (5.18×10^{-4} m^2/s^2 at 140.10 year-days) peak during the receding tide, and are relatively small during the incoming tide.

4.5 Between Set Comparisons

Characteristics for each data set are presented in Tables 4.2 and 4.3. Because this study is framed in an ecological context, the directionality of both the horizontal velocity and the Reynolds shear stress are unimportant from an organismal perspective. Means of the absolute value of individual burst-average values for these quantities are presented in Tables 4.2 and 4.3. Discussion of individual data sets will still refer to the directional quantities. The DMHside16 and DMH16 data sets stand out due to their relatively small mean $\langle \bar{u} \rangle$ velocity. For the DMHside16 data set, U velocity is small for the outgoing tide (see Figure 4.12), while it is small everywhere in the DMH16 set (see Figure 4.14). For all sets, the $\langle \bar{v} \rangle$ velocity values are multiple orders of magnitude below the $\langle \bar{u} \rangle$ velocity, as expected due to the rotation of each individual burst to maximize $\langle \bar{u} \rangle$ velocity. The removal of points flagged during phase filtration results in $\langle \bar{v} \rangle$ values that are nonzero, but are still very small relative to $\langle \bar{u} \rangle$ velocity. For all sets, the mean $\langle \bar{w} \rangle$ velocity values are negative. However, some individual

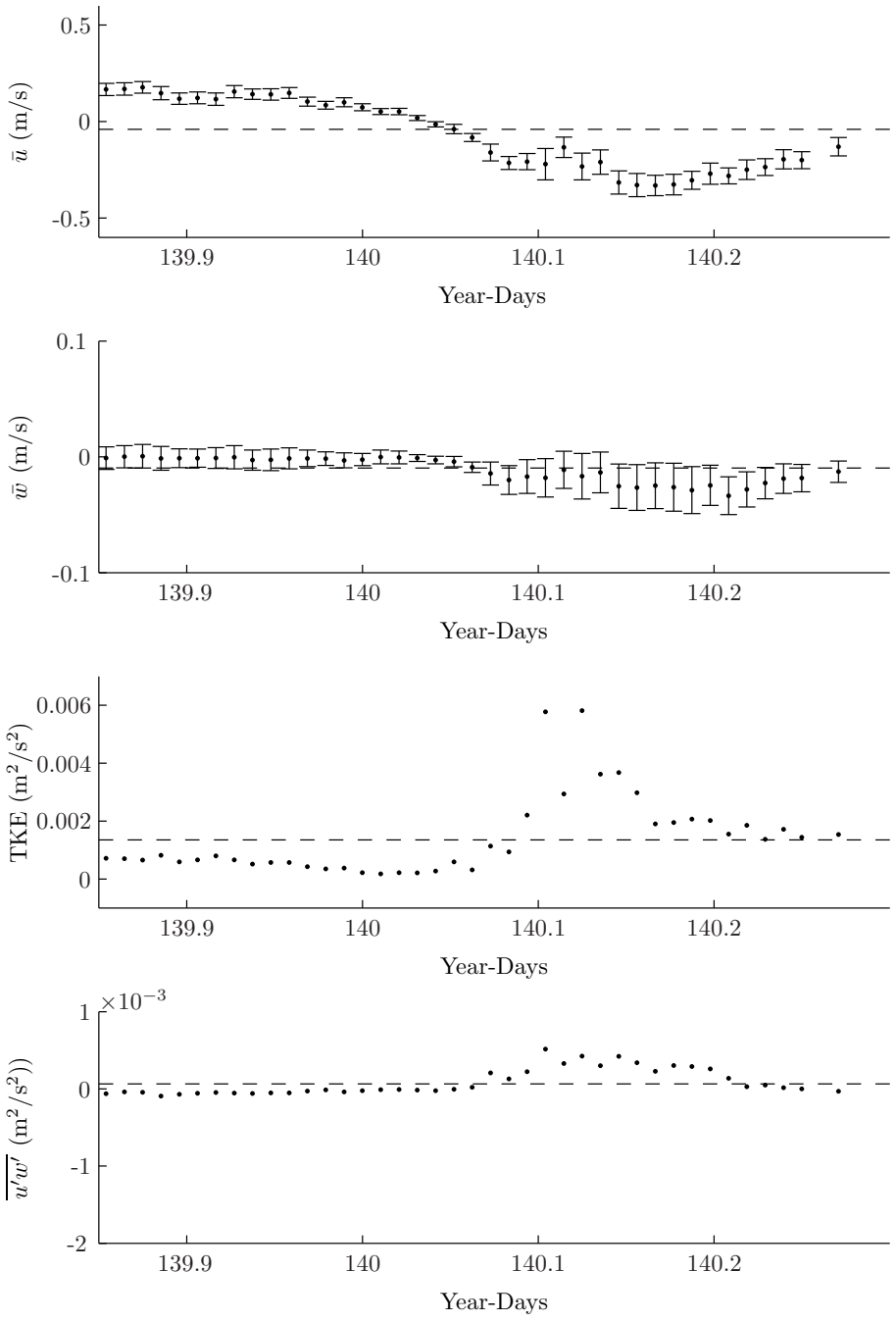

Figure 4.19: Burst-average records for Skidaway20 data set. The dashed line indicates the mean of the burst-average values. The error bars in the burst-average velocity plots correspond to standard deviation.

burst-average values are positive and varied with tidal flow.

TKE is largest for the House16 (2.87×10^{-3} m^2/s^2) and Wilmington14 (2.86×10^{-3} m^2/s^2) sets. Of these two sets, the Wilmington14 set (Figure 4.7) shows the most tidal variability, with the maximum and minimum burst-average Reynolds shear stress both being an order of magnitude larger than the House16 set (Figure 4.15). The Wilmington14 set also has the most deviation from the mean and within-burst variability for the vertical velocity.

TKE for the DMH16 set is smallest, at 4.91×10^{-4} m^2/s^2, and the TKE for the Skidaway14 set is also small at 6.27×10^{-4} m^2/s^2. These sets also have the smallest absolute value of burst-averaged Reynolds shear stresses (2.79×10^{-5} m^2/s^2 and 2.96×10^{-5} m^2/s^2, respectively). The DMH16 set exhibits little variability and small mean values for $\langle \bar{u} \rangle$ and $\langle \bar{w} \rangle$ velocity (see Figure 4.14), which may explain the small values of the fluctuation quantities. The Skidaway14 set exhibits greater $\langle \bar{u} \rangle$ velocity when concurrent sets are at minimums (see Figure 4.9), which could indicate a different flow environment relative to the other sites.

Turbulence intensity (TI) provides insight to the magnitude of the velocity fluctuations relative to the mean velocity magnitude. The DMH16 set (5.60×10^{-1}) has the largest TI, while it has one of the smaller TKE values. Conversely, while the House16 set has the largest TKE, the TI (40.9%) is less than half that of the DMH16 set.

Tidal influences within the estuary were observed, as turbulent characteristics often reach absolute maximum values during the incoming or outgoing tides, and sites on the whole were less energetic at high tide when flowrates should be at a minimum. However, some sets (DMH16 for example) did not show a noticeable tidal response, further illustrating the spatial and temporal variability observed in the study. Similar variability in turbulence parameters has been seen in another study in a small estuary

by Trevethan and Chanson [40], where variability was primarily attributed to small water depths, among other factors.

Table 4.2: Set lengths and mean velocities grouped by day. The mean and standard deviation are computed from the individual burst-averaged values for each data set.

set name	length	$\lvert\bar{u}\rvert$ (m/s)		$\bar{v}$ (m/s)		$\bar{w}$ (m/s)	
	days	mean	std dev	mean	std dev	mean	std dev
5/14/2007							
Herb14	0.61	2.11E-01	9.34E-02	2.06E-04	2.00E-03	-4.64E-03	6.65E-03
Wilmington14	0.57	3.19E-01	1.02E-01	-1.70E-04	3.32E-04	-9.58E-03	3.65E-02
Skidaway14	0.53	1.19E-01	8.70E-02	-4.44E-05	2.19E-04	-5.16E-03	5.85E-03
Moon14	0.53	2.65E-01	1.24E-01	3.26E-05	1.73E-04	5.99E-03	1.39E-02
5/16/2007							
DMHside16	0.49	8.42E-02	4.51E-02	6.80E-05	2.57E-04	-4.29E-03	5.16E-03
Herb16	0.51	1.77E-01	1.34E-01	1.19E-04	2.64E-04	-1.38E-02	5.87E-03
DMH16	0.51	5.28E-02	3.18E-02	1.12E-04	2.78E-04	-3.47E-03	1.63E-03
House16	0.43	2.15E-01	8.49E-02	1.08E-05	2.31E-04	-1.69E-02	5.27E-03
5/19/2007							
Herb19	0.60	1.91E-01	9.12E-02	-3.54E-05	1.99E-04	-9.99E-03	4.18E-03
Skidaway19	0.60	1.77E-01	1.02E-01	3.82E-05	1.34E-04	-5.92E-03	3.38E-03
Wilmington19	0.58	1.62E-01	1.11E-01	-2.57E-05	1.98E-04	-1.25E-02	9.46E-03
5/20/2007							
Skidaway20	0.64	1.64E-01	8.33E-02	1.29E-04	6.50E-04	-9.65E-03	1.06E-02

Table 4.3: Set TKE, Turbulence Intensity (TI), and Reynolds shear stresses grouped by day. The mean and standard deviation are computed from the individual burst-averaged values for each data set.

set name	TKE (m^2/s^2)		TI %		$\lvert\overline{u'w'}\rvert$ (m^2/s^2)	
	mean	std dev	mean	std dev	mean	std dev
5/14/2007						
Herb14	2.06E-03	1.54E-03	35.3	28.4	1.54E-04	1.18E-04
Wilmington14	2.86E-03	1.23E-03	23.8	3.7	5.97E-04	5.06E-04
Skidaway14	6.27E-04	6.12E-04	47.1	49.2	4.03E-05	4.86E-05
Moon14	1.29E-03	7.57E-04	25.9	33.3	1.63E-04	1.08E-04
5/16/2007						
DMHside16	8.75E-04	3.26E-04	66.0	39.9	1.16E-04	9.10E-05
Herb16	1.42E-03	9.69E-04	38.3	19.6	2.79E-04	1.95E-04
DMH16	4.91E-04	2.62E-04	97.0	107.6	4.53E-05	3.72E-05
House16	2.87E-03	7.25E-04	40.9	19.5	3.10E-04	1.85E-04
5/19/2007						
Herb19	1.23E-03	4.90E-04	53.3	103.4	1.66E-04	9.24E-05
Skidaway19	7.53E-04	6.04E-04	25.6	15.1	1.19E-04	1.20E-04
Wilmington19	1.15E-03	4.35E-04	64.5	69.0	2.22E-04	1.65E-04
5/20/2007						
Skidaway20	1.35E-03	1.30E-03	35.3	25.0	1.18E-04	1.33E-04

4.5.1 Spatial Comparisons

4.5.1.1 5/14/07

The Herb14, Wilmington14, Skidaway14, and Moon14 data sets were collected on 5/14/2007. Set mean behavior is presented in Figure 4.20. Burst-average values are presented in Figures 4.6, 4.7, 4.9, and 4.10, respectively. Of the sets, the Wilmington14 set exhibits the most tidal influence, as both the incoming and outgoing tides result in extreme values of $\bar{u}$, $\bar{w}$, TKE, and Reynolds shear stress. The Wilmington14 w velocity variation both within-burst and of burst-average values is the greatest of any set collected on any day. The large mean velocities of the Wilmington14 set (mean burst-average $\langle|\bar{u}|\rangle$ of 3.19×10^{-1} m/s, for example) result in a TI value that is the smallest of those sites observed on 5/14/07. The mean absolute value of the burst-averaged Reynolds shear stress is greatest for the Wilmington14 set. The Herb14 and Moon14 sets have tidal behavior for incoming and outgoing tides in $\bar{u}$ and $\bar{w}$, but strong tidal response in TKE and Reynolds shear stress is predominately seen in the outgoing tide, if at all. Both sets have mean $\langle|\bar{u}|\rangle$ above 0.2 m/s, and while the mean burst-average $\langle|\bar{u}|\rangle$ is greater for the Moon14 set, the Herb14 set has a larger TKE and TI. The mean of the burst-average values of $\langle|\bar{u}|\rangle$, TKE, and Reynolds shear stress for the Skidaway14 set are smaller than the corresponding calculations for the data collected at other sites. Of particular note are the "lull periods" that occur around 133.73 and 133.95 year-days (see Figure 4.9). These are areas where the other sets are more likely to experience extreme values, but the Skidaway14 values are depressed and exhibit smaller within-burst variability in u and w (see Figure 4.9). Turbulence intensity, however, is has the greatest set mean value for the Skidaway14 set.

For these sets, the relationships between sites for $\langle|\bar{u}|\rangle$, TKE, and absolute value of Reynolds shear stress all remain consistent, while the trends are reversed for TI (see

Figure 4.20). Spatially, the Wilmington River is the widest water body and is located closest to Wassaw Sound. The Wilmington14 set could then reasonably be expected to have the strongest tidal response. Among the other three sites, the tidal influence is not clear based on the spatial arrangement of the sites (see Figure 3.1).

4.5.1.2 5/16/07

The DMHside16, Herb16, DMH16, and House16 data sets were collected on 5/16/2007. Set mean behavior is presented in Figure 4.21. Burst-average values are presented in Figures 4.12, 4.13, 4.14 and 4.15, respectively. The House16 parameters plotted in Figure 4.15 exhibit variation in both the incoming and outgoing tides. The tidal response is greater for the incoming tide (maximum U velocity and Reynolds shear stress) in the Herb16 data set, but is still present in the outgoing tide. The House16 data set had the greatest mean TKE at 2.87×10^{-3} m^2/s^2, while the Herb16 set also had a relatively large 1.42×10^{-3} m^2/s^2 mean. Both sets collected at Dead Man's Hammock exhibited small values of TKE and Reynolds shear stress relative to the Herb16 and House16 sets, although the converse is true for TI (see Table 4.3). Additionally, the $\bar{u}$ and $\bar{w}$ values for these sets were also small and stayed close to the mean. For these sets, the relationships between sites for $\langle|\bar{u}|\rangle$, TKE, and absolute value of Reynolds shear stress all remain the same, while the relationships are inverted for TI (see Figure 4.21).

Spatially, the Dead Man's Hammock and House Creek study sites (see Figure 3.1) were the only sites on Wassaw Sound itself monitored during this study. While the House16 set had the largest set average values of $\langle|\bar{u}|\rangle$, TKE, and absolute value of Reynolds shear stress, this was not observed for either set at Dead Man's Hammock, which had much smaller values when compared to the inland Herb16 set. While a heightened response in most of the measured parameters might be expected closer to

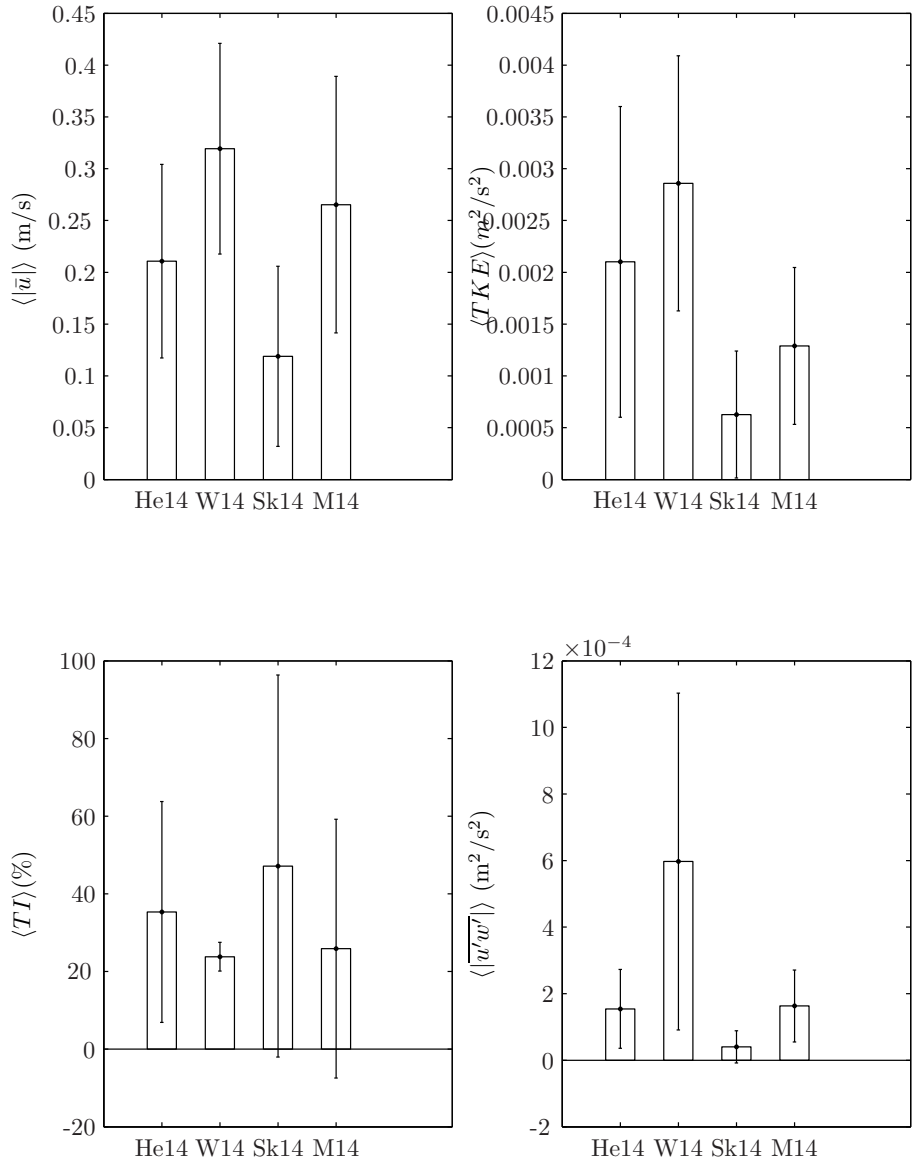

Figure 4.20: Set mean $\langle|\bar{u}|\rangle$, TKE, TI, and absolute value of the Reynolds shear stress for all sites where data were collected on 5/14/07. He14 stands for Herb14, W14 for Wilmington14, Sk14 for Skidaway14, and M14 for Moon14.

the open sea for the DMH16 and DMHside16 sets, only TI is larger for the two sets relative to the Herb16 and House16 sets.

4.5.1.3 5/19/07

The Herb19, Skidaway19, and Wilmington19 data sets were collected on 5/19/2007. Set mean behavior is presented in Figure 4.22. Burst-average values are presented in Figures 4.16, 4.17, and 4.18, respectively. These data sets appear to begin at the beginning of an incoming tide, as the $\bar{u}$ maximum for the Skidaway19 set occurs at the beginning of the time record (see Figure 4.17), although the other sets do not exhibit this trend to the same extreme. For the Skidaway19 and Herb19 sets, tidal response results in the maximum magnitude of $\bar{u}$ and TKE occurring during the outgoing tide, while the Wilmington river set has a stronger response to the incoming tide. The mean $\langle|\bar{u}|\rangle$ values between the three sites are similar, with a maximum value of 1.91×10^{-1} m/s (Herb19) and a minimum of 1.62×10^{-1} m/s (see Table 4.2). Deviation from mean TKE is much more evident in the Skidaway19 and Herb19 sets (Figure 4.17 and 4.16) than in the Wilmington19 set (Figure 4.18). As seen in the 5/14/2007 observations, the TKE for the Skidaway19 set is roughly half that of the mean TKEs for other sites monitored at the same time. While site trends were consistent across mean burst-average values of $\langle|\bar{u}|\rangle$, TKE, and absolute value of Reynolds shear stress for observations on the other days, here the site with the minimum $\langle|\bar{u}|\rangle$ value (Wilmington19) has the largest absolute value of Reynolds shear stress. Additionally, the set with the smallest TKE value (Skidaway19) does not exhibit a relatively large TI (see Figure 4.22), as seen among set collected on other days.

Spatially, the Wilmington river again exhibited the largest set mean values of TKE and absolute value of Reynolds shear stress when compared to sites that are further

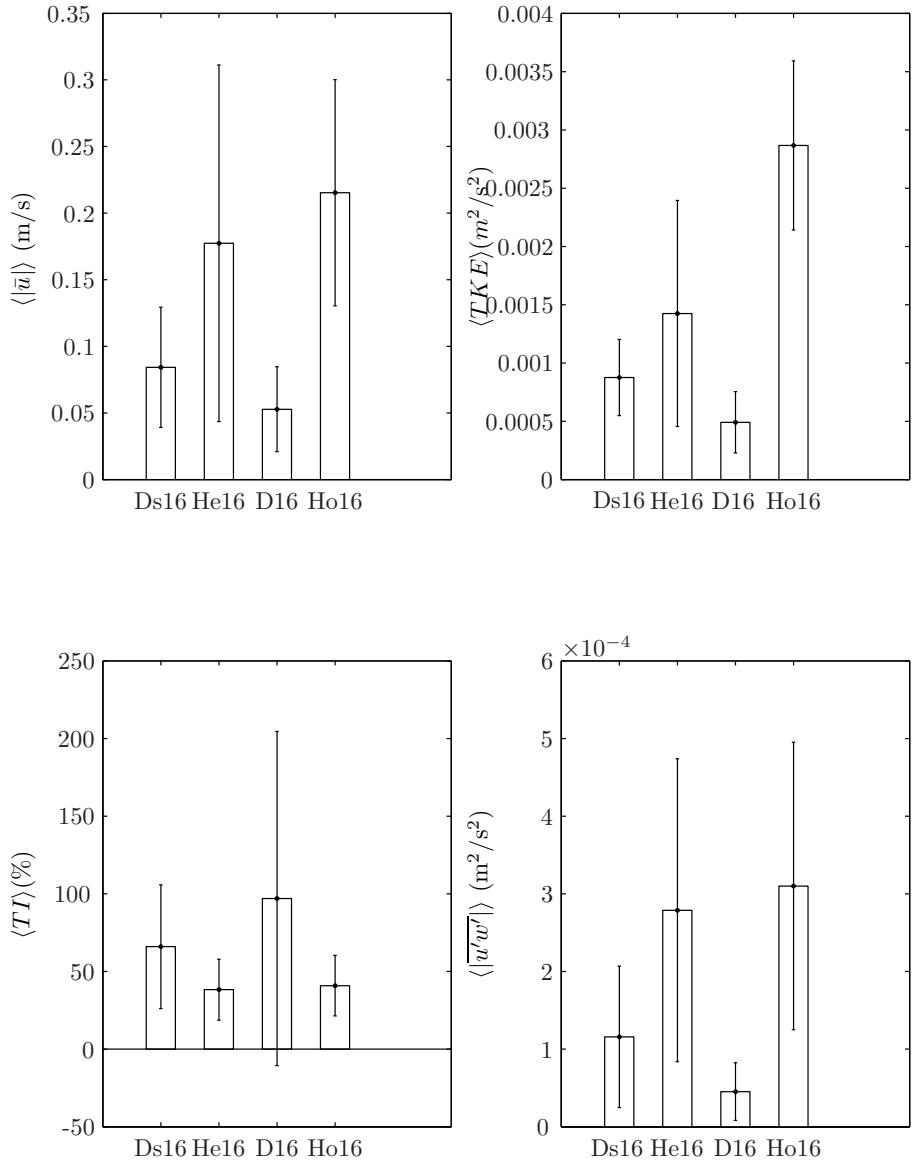

Figure 4.21: Set mean $\langle|\bar{u}|\rangle$, TKE, TI, and absolute value of Reynolds shear stress for all sites where data were collected on 5/16/07. Ds16 stands for DMHside16, He16 for Herb16, D16 for DMH16, and Ho16 for House16.

inland, as seen on 5/14/07.

4.5.2 Temporal Comparisons

4.5.2.1 Herb River

Data were collected in the Herb River on 5/14, 5/16, and 5/19. Set mean behavior at the site is presented in Figure 4.23. The mean $\langle|\bar{u}|\rangle$ velocity magnitude for the Herb14 (2.11×10^{-1} m/s) set is only slightly larger than that of the Herb16 (1.77×10^{-1} m/s) or Herb19 (1.91×10^{-1} m/s) sets. TKE is also greatest (2.06×10^{-3} m^2/s^2) for the Herb14 set. The opposite is true for mean $\langle\bar{w}\rangle$ velocity magnitude, where Herb14 (-4.64×10^{-3} m/s) is the smallest, compared to Herb16 (-1.38×10^{-2} m/s) and Herb19 (-9.99×10^{-3} m/s) (see Table 4.2). The Reynolds shear stress is also smallest (1.15×10^{-5} m^2/s^2) for the Herb14 set. The Herb14 and Herb19 burst properties generally peak during the outgoing tide (see Figures 4.6 and 4.16), while the parameter magnitudes reach their peak for the incoming tide for the Herb16 data set (see Figure 4.13).

4.5.2.2 Skidaway River

Data were collected in the Skidaway River on 5/14, 5/19, and 5/20. Set mean behavior at the site is presented in Figure 4.24. The unusual $\bar{u}$ velocity "lull period" exhibited in the Skidaway14 data set (see Figure 4.9) was not seen in the Skidaway19 (see Figure 4.17) or Skidaway20 (see Figure 4.19) data sets. On both occasions (5/14 and 5/19) when other sites were concurrently monitored, the mean TKE for the Skidaway River sets was approximately half of that for the other sites (see Table 4.3). In contrast, the mean TKE for the Skidaway20 set is on the order of the larger TKE values found at other sites. The same trend is not exhibited in $\langle|\bar{u}|\rangle$, $\langle\bar{w}\rangle$, or Reynolds shear stress.

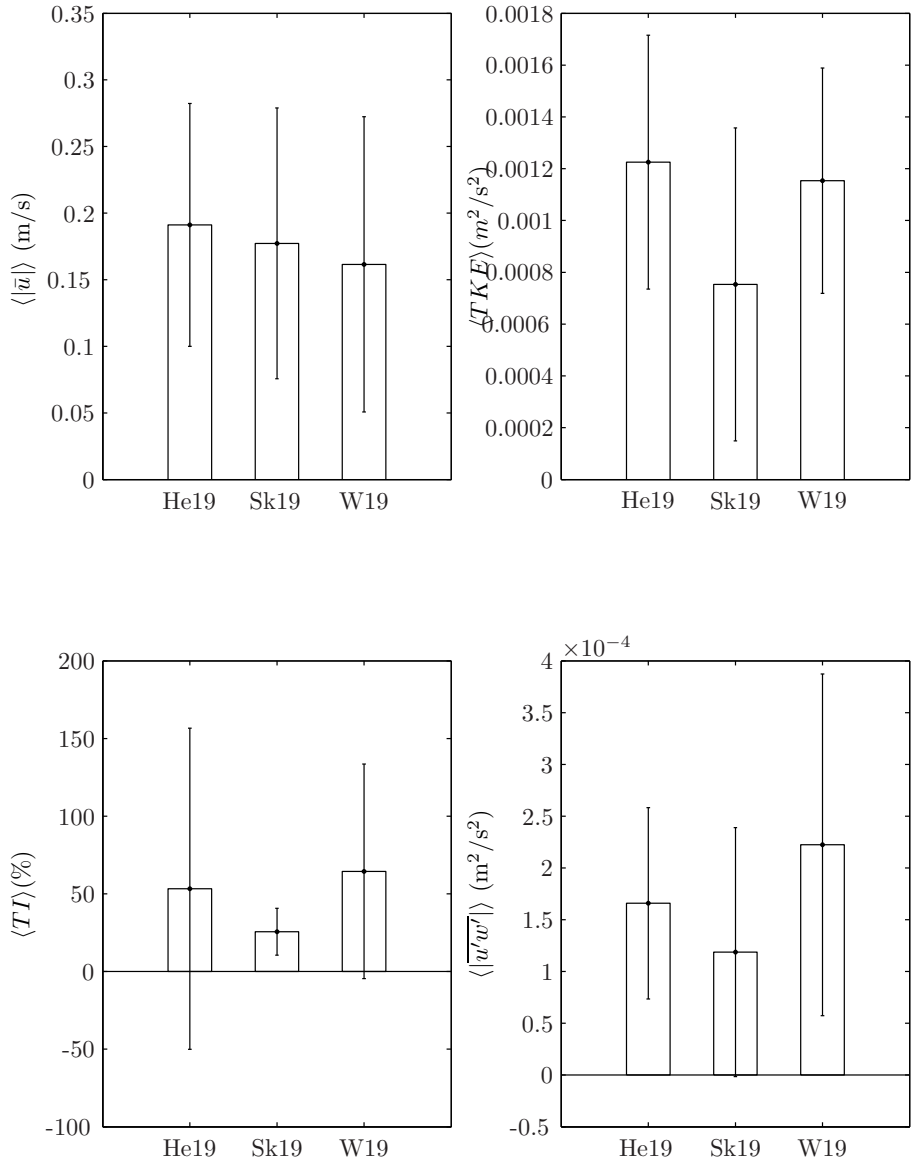

Figure 4.22: Set mean $\langle|\bar{u}|\rangle$, TKE, TI, and absolute value of Reynolds shear stress for all sites where data were collected on 5/19/07. He19 stands for Herb19, Sk19 for Skidaway19, and W19 for Wilmington19.

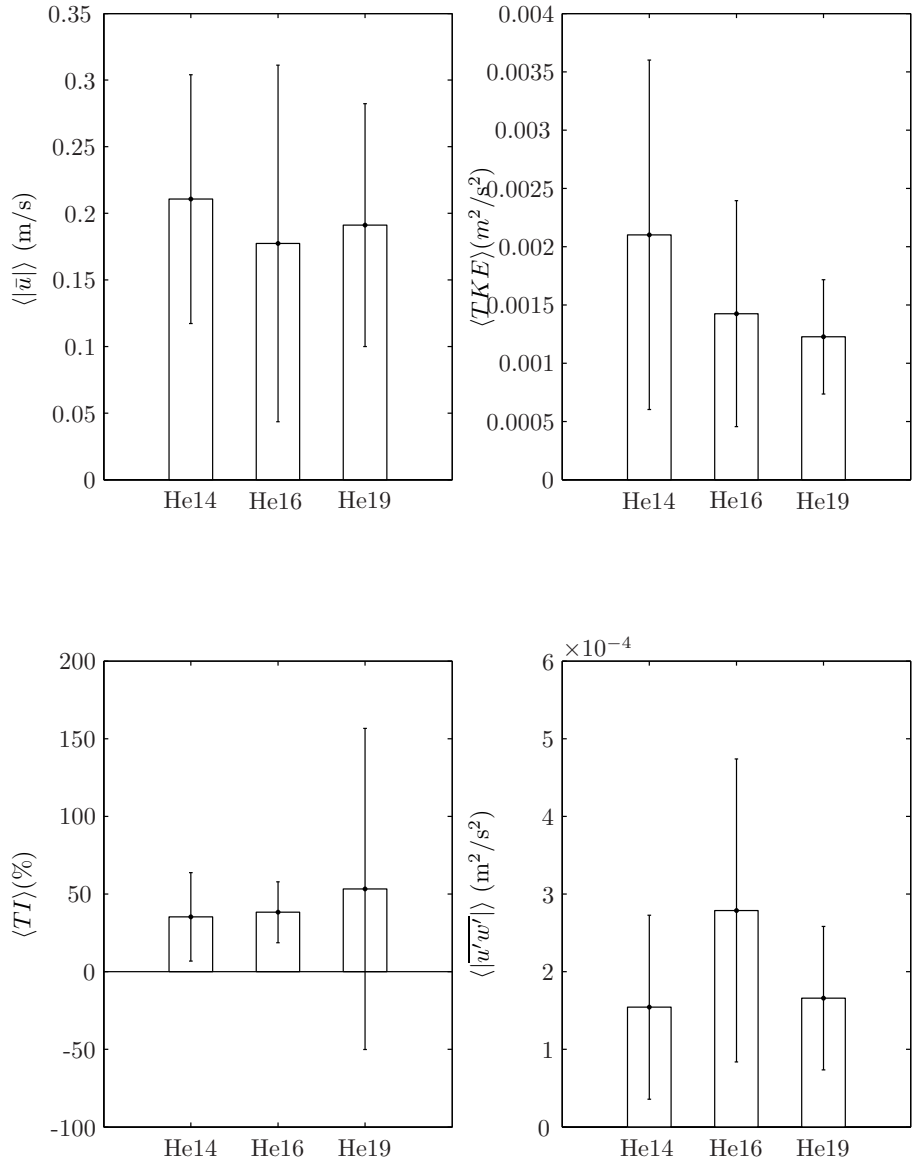

Figure 4.23: Set mean $\langle|\bar{u}|\rangle$, TKE, TI, and absolute value of Reynolds shear stress for the Herb River data sets. He14 stands for Herb14, etc.

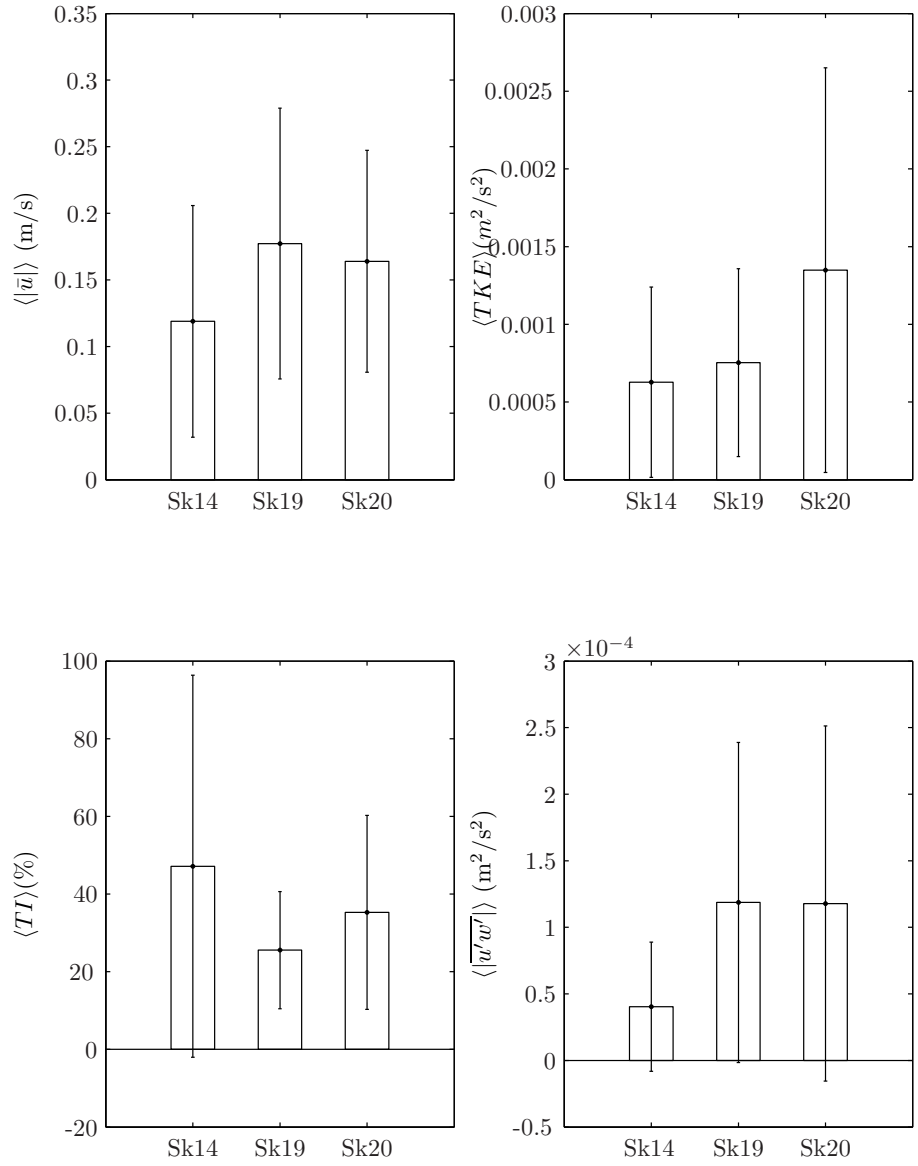

Figure 4.24: Set mean $\langle|\bar{u}|\rangle$, TKE, TI, and absolute value of Reynolds shear stress for the Skidaway River data sets. Sk14 stands for Skidaway14, etc.

4.5.2.3 Wilmington River

Data were collected in the Wilmington River on 5/14 and 5/19. Set mean behavior at the site is presented in Figure 4.25. Both TKE and Reynolds stress set means are greater for the Wilmington14 data sets (see Table 4.3). For both sets, burst properties generally peak during the incoming tide. The Wilmington14 set has larger mean $\langle|\bar{u}|\rangle$, TKE, and absolute value of Reynolds shear stress compared to the Wilmington19 set, but a smaller TI.

4.6 Sources of Uncertainty

As with any field study, there are a variety of uncertainties associated with the collection and manipulation of the data. Bursts were rotated to maximize the absolute value of the $\bar{u}$ velocity for each burst. Only horizontal velocity components were rotated however; the w velocity was left as recorded. When placing an ADV probe in the field, it is difficult to ensure the axes are perfectly aligned with the flow directions, and the vertical component of velocity could be incorrectly oriented if the probe was not precisely leveled. While the wave removal calculations are designed to account for the inflation of apparent turbulent statistics due to wave contributions, no correction for imprecise vector orientation is made for the mean velocity comparisons. Imprecise vector orientation may be magnified when making comparisons between sets due to the likely random nature of inaccurate instrument placement.

Another source of uncertainty when comparing across days is the inexact matching of tidal cycle length. The data collected on 5/19/07 seems to start somewhere in the middle of the rising tide, where sets from other days may have started closer to low tide, when the probe first became submerged. While the overall mean behavior should be comparable, differences in set lengths due to the removal of bursts with

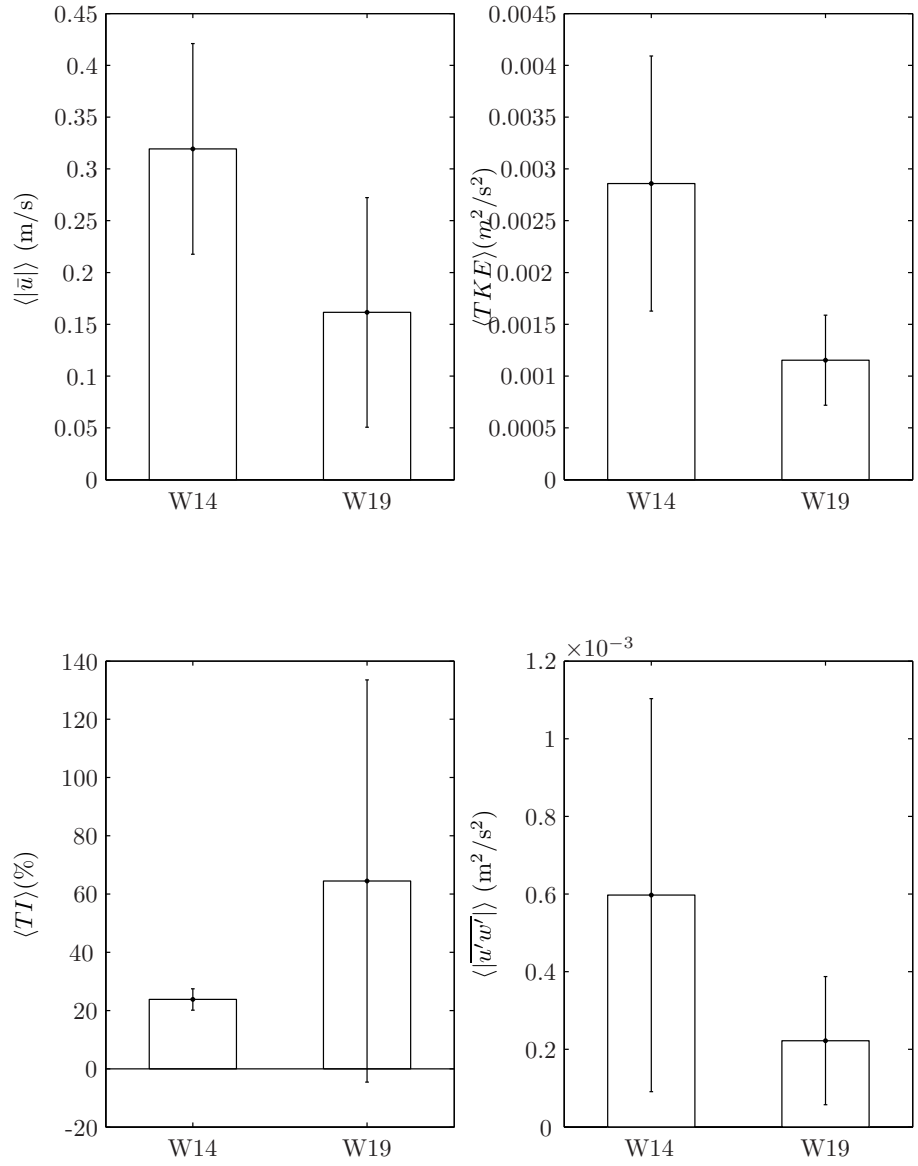

Figure 4.25: Set mean $\langle|\bar{u}|\rangle$, TKE, TI, and absolute value of Reynolds shear stress for all Wilmington River data collections. W14 stands for Wilmington14, etc.

poor data quality could cause uncertainty, even for measurements taken on the same day.

4.6.1 Phase Filtering

In the calculation of many of the parameters used to characterize the sets presented in this study, only points that were unflagged by the phase filtering procedure were used. The only exceptions are the wave contribution components of TKE and Reynolds shear stress, which use unflagged and interpolated points (discussed in Section 3.3.3.1). For sets with large amounts of replacement (Herb14, DMHco20 and DMHsh20), the polynomial fits used to interpolate and replace spikes are based on points that can be far removed from some the points flagged as spikes, which results in inflated interpolated values, particularly at the beginning or end of a burst where the data used in the fit do not extend to either side of the flagged area. In the case of normal stresses, these inflated interpolated points can result in increased wave contributions that exceed the normal stress values of the $\overline{(u-\bar{u})(u-\bar{u})}$ value for the unflagged data set (discussed in Section 3.3.3.2). This discrepancy between velocity sets including unflagged points only and those including interpolated points does introduce some uncertainty, which is magnified in those sets with large number of replaced values. The small levels of replacement (see Table 3.3) for the other sets and the fact that only sets with banding encountered wave induced normal stresses with greater magnitudes than the entire normal stresses is a good indicator that the introduced uncertainty is small.

Additionally, the banded sets where the correction factor was introduced required empirical tailoring of the parameters to catch banded points. Despite the fine tuning, acceptable results were not obtained for those sets with heavy banding, DMHco20

and DMHsh20, without flagging points at rates near 70%. The difficulty in determining when the banding ended and where good data (if any) began likely results in banded points remaining unflagged in some bursts while good points were flagged for interpolation in other bursts.

4.6.2 Wave Removal

As in the treatment for banded sets in the phase filtering methodology, some empirical tuning was used in the peak identification procedure used in wave contribution calculations. Automation of defining the peak span based upon pre-set offsets from a peak value means that for some cases, the wave peak span will be over- or underestimated when compared to the actual wave peak discernible to visual inspection, and calculations based on the incorrect wave peak span will be affected accordingly. It is also possible that some bursts did not exhibit a meaningful wave influence. While visual inspection suggested that most bursts had at least some minor wave effects, there is no provision in the methodology for a PSD without a wave peak. Any burst without a wave peak will have one imposed upon it, potentially overestimating the wave contributions. When wave peaks are present, however, the PSD coefficients are usually orders of magnitude greater than the power in nearby frequencies. If an incorrect wave peak is identified, it is likely that the magnitudes of the PSD for the false peak make up a relatively small portion of the total power, and thus this source of error should be small.

CHAPTER V

CONCLUSIONS

The current study examines naturally occurring differences in the turbulent environment at a variety of field sites near the Skidaway Institute of Oceanography. Acoustic Doppler velocimetry (ADV) was used to record point velocities in support of work performed by Smee and Ferner ([33], [9], [35]). Data sets were composed of 5 minute bursts sampled at 16 Hz separated by 15 minutes intervals. Basic filtering of the data sets was performed using equipment-provided data quality parameters. Horizontal velocities were rotated within each burst to maximize the U velocity component. Data quality was further improved by applying a phase filtering procedure to each velocity time series to identify and smooth velocity spikes, following the methodology of Goring and Nikora [12]. Because the sites were potentially subjected to wave interference, which can appear as turbulent fluctuations (see [43]), wave influence was also addressed. Velocity power spectra were utilized to compute the wave contribution to both normal and shear stresses using the method described by Bricker and Monismith [4]. In addition to shear and normal stresses, the turbulent kinetic energy (TKE) and turbulence intensity (TI) were also computed. The computed parameters serve to characterize the sites and allow for comparisons both spatially and temporally.

5.1 Phase Filtering

This study serves to illustrate the importance of rigorous consideration of data quality when using data collected from ADVs. For sets that did not exhibit banded behavior (all except Herb14, DMHsh20 and DMHco20), no more than 3% of individual velocity

measurements were flagged as spikes (see Table 3.3). Despite the fact that generally a small number of points were removed, these points are almost exclusively extreme values (see Figure 3.4) that should not be included in further analysis of the data set. The small removal rates do not have a noticeable effect on the burst-averaged velocity values (see Figures 4.1 and 4.2). In contrast, the data identified as spikes were found to alter the burst-averaged values of TKE (see Figure 4.3) because the extreme values disproportionately contribute to elevated TKE measurements due to their relatively large magnitudes. These findings are consistent with prior observations regarding the importance of advanced data filtering when working with ADV data (see [12] and [6]).

The use of phase filtration with banded sets produced mixed results. The Herb14 set, which exhibited some banded bursts, had 28.72% of its points flagged as spikes. Spike removal resulted in a decrease of TKE from 0.039 m^2/s^2 to 0.0024 m^2/s^2. The DMHco20 and DMHsh20 sets, which contained extensively banded bursts, had approximately 70% of all points flagged as spikes (further discussed in Section 3.3.2.4). For the DMHco20 and DMHsh20 sets, the extensive banding did not allow the phase filtering process to improve data quality to the level of the other sets, even at large replacement rates.

5.2 Wave Removal

The removal of wave energy in this study addresses both the magnitude of wave contribution to the apparent TKE and Reynolds shear stress calculations at the study sites in particular and serves to demonstrate the importance of considering wave contributions in studies where waves may be present. Despite prior observations of relatively small surface wave activity [9], the current data demonstrate wave contributions to both TKE and Reynolds shear stress in the Wassaw Sound ecosystem (see Table 4.1).

In extreme cases, wave-related fluctuations accounted for as much as 57.4% of the TKE (DMH16 set) and as much as 85.5% of the Reynolds shear stress (Herb16 set). While the majority of both TKE and Reynolds shear stress wave contributions were below 50%, every set had some wave contribution.

In characterizing field sites, addressing wave contributions is clearly important to gain a better understanding of the sources of energy within the system. This is particularly true in small estuarine systems, where little prior work has been done to describe the turbulent characteristics. TKE for all of the sets excluding DMH16 and DMHside16 had wave contributions that were between 10% and 20% of the total TKE. It is also important to consider the role that wave contributions play in making comparisons between sites. Ranked comparisons between the sites in this study would not have changed dramatically if wave contributions were not addressed.

5.3 Set Comparisons

5.3.1 Spatial Differences

Because data were collected from multiple sites simultaneously, it is possible to compare the turbulent characteristics under the same large-scale environmental conditions. For the sets collected on 5/14/2007 (Herb14, Wilmington14, Skidaway14, and Moon14), there is great variability. Tidal influence is strongly seen in the Herb14 set (see Figure 4.6), some variability is seen in the Herb14 and Moon14 sets, and the Skidaway14 site has smaller magnitudes and variability in $\bar{u}$, $\bar{w}$, TKE, and Reynolds shear stress.

On 5/16/07, the House16 set showed the most tidal variability, as well as the greatest mean TKE. The DMH16 and DMHside16 sets had small burst-averaged velocities, and TKE, although the TI for both sets are larger than for the House16 and Herb16

sets (see Figure 4.21).

On 5/19/07, the Herb19 (see Figure 4.16) and Skidaway19 (see Figure 4.17) data sets had similar overall behaviors and tidal dependence, with similar peaks in $\bar{u}$ and TKE, entirely negative burst-average $\bar{w}$ values, and small value Reynolds shear stress. While the maximum magnitude of burst-average $\bar{u}$ for these sets occurs during the outgoing tide, the maximum magnitude burst-average $\bar{u}$ for the Wilmington19 set occurs during the incoming tide. The Skidaway19 set has the smallest TKE and TI among the three sets (see Figure 4.22). On the same day in locations that are exposed to similar environmental conditions, two sets (Herb19 and Skidaway19) have similar properties, while the third (Wilmington19) is clearly experiencing different local flow conditions. The varying amounts of similarity across spatial differences illustrates the importance of local factors in shaping the hydrodynamic characteristics of a study site.

Spatially, some overall trends emerge. The Wilmington14 set, perhaps due to its location closest to Wassaw Sound of the four sites observed on 5/14/07, has the largest set mean values of $\langle|\bar{u}|\rangle$, TKE, and absolute value of the Reynolds shear stress (see Figure 4.20). Meanwhile, the Skidaway14 set, with the smallest set mean values of $\langle|\bar{u}|\rangle$, TKE, and absolute value of the Reynolds shear stress has the largest TI. This trend, where $\langle|\bar{u}|\rangle$, TKE, and absolute value of the Reynolds shear stress seem to be positively correlated with each other and negatively correlated with TI is also seen in observations taken on 5/16/07, but not on 5/19/07. Of the sites bordering Wassaw Sound, the DMHside16 and DMH16 sets have smaller $\langle|\bar{u}|\rangle$, TKE, and absolute value of the Reynolds shear stress but larger TI compared to the House16 set. The Skidaway River site generally had the smallest $\langle|\bar{u}|\rangle$, TKE, and absolute value of the Reynolds shear stress values relative to sites monitored at the same time, although the Skidaway14 set had a large TI and the Skidaway19 set did not

have the smallest $\langle|\bar{u}|\rangle$ (see Figures 4.20, 4.21, and 4.22). The Herb River and Moon River measurements usually fell between those of the Wilmington River and Skidaway River.

The findings illustrate the importance of factors that act on scales smaller than the primary tidal forcing within the estuary. While sites monitored simultaneously were subjected to identical estuary-scale tidal behavior, significant differences in the evolution of turbulent characteristics were observed. Local bed geometry, local vegetation, organismal aggregation (marshes and oyster reefs, for example), and flow influx from tributaries or porewater sources are all factors that could alter turbulent properties at the cross-site scales monitored in this experiment.

5.3.2 Temporal Differences

With the same study areas being sampled multiple times over the course of a week, it is also possible to address temporal changes. The Herb River site was observed on 5/14/07, 5/16/07, and 5/19/07. For this site, both mean burst-average $\langle|\bar{u}|\rangle$ and TKE decrease in time, while TI increases (see Figure 4.23). The Herb16 data set Reynolds shear stress was greatly variable within the set with a maximum value of 4.00×10^{-3} m^2/s^2 and an extreme negative value of -7.00×10^{-3} m^2/s^2, both greater in magnitude than any burst-average value within the Herb14 or Herb19 sets. For the Skidaway River sets, the "lull periods" observed in the Skidaway14 $\bar{u}$ velocity time record (Figure 4.9) were not seen in the Skidaway19 or Skidaway20 sets. The mean burst-average TKE and Reynolds shear stress were smaller for the Skidaway14 set than for the others, although the TI was the largest (Figure 4.24). The Wilmington River was observed on two days, with the mean TKE and Reynolds shear stress being greater in the Wilmington14 set and the mean TI being greater in the Wilmington19 set (Figure 4.25). In both sets, properties reach maximum magnitudes during the

incoming tides. As seen for the spatial comparisons, the temporal comparisons vary greatly even within the same study site.

The great variability observed temporally within a site also includes spatial variation. The contributions of space and time differences to the variability of turbulent properties are difficult to seperate because the probes were placed within the same site but not at the exact same location across different days. Hence the data cover a representative sampling of turbulent characteristics within each site. The difficulty in this study in drawing any overarching conclusions about differences in sites is a testament to the challenges of characterizing sites, which have internal variability.

5.3.3 Ecological Consequences

The overall findings of the study suggest that TKE, Reynolds shear stress, and TI vary greatly within the Wassaw Sound ecosystem, both spatially and temporally. Burst-average turbulent characteristics also do not exhibit any universal trends. For example, when comparing data collected on 5/14/07 (Figure 4.20), a relatively large value of TKE corresponds to a relatively small TI (the Wilmington14 set), while small TKE corresponds to a large TI (the Skidaway14 set). Contrast this with the data collected on 5/19/07 (Figure 4.22), where relatively large TKE corresponds to relatively large TI (the Herb19 and Wilmington19 sets) and small TKE corresponds to small TI (the Skidaway19 set). Reynolds shear stress is equally variable across the data sets relative to TKE. Generally, the burst-average $\bar{u}$ velocity corresponds well to TKE (see the Wilmington14 set, Figure 4.7). However, sometimes this relationship does not occur (see Herb19 set, Figure 4.16). The turbulent properties presented in this study serve to help characterize some locations within the Wassaw Sound estuary, one of the few characterizations perfomed on small estuary sites.

In order to fully characterize a study site from an ecological prespective, the spatial and temporal scales relevant to the organisms of interest must be considered. In this study, sites were chosen based on a spatial scale appropriate for studying predator-prey interactions. Because benthic organisms can move over ranges much greater than those observed to generate differences in turbulent properties (although temporal differences may also play a role, see previous section), the monitoring if multiple points within a site may be nececssary to characterize an ecological study site. Because it is impossible *a priori* to know how many locations within a site are needed to characterize the hydrodynamic environment, preliminary observations should be performed in order to identify the small-scale variations within a site. After representative spatial locations within a site have been chosen, it is important to monitor these sites repeatedly over the course of many tidal cycles. Temporal observations on the scale of tidal strength variations (such as spring and neap tides, for example) would allow for the impact of turbulent characterstics over an ecologically-relevant time scale that incorporates more environmental variability. Local differences in turbulent characteristics have been observed to be associated with significant differences in predator-prey interactions (see [9] and [35]), illustrating the importance of comprehensively addressing the small-scale turbulent differences within a site.

Prior studies have suggested TI (see [30], [33], and [9]) and root-mean-square of velocity fluctuations (see [34] and [35]) to be governing parameters for turbulent impacts on ecological processes. However, from a turbulent characteristics standpoint, these parameters are only part of the flow characterization. TKE gives an estimate of the actual magnitude of turbulent fluctuations independent of mean velocity behavior. Reynolds shear stress is a critical component in defining the boundary layer, where benthic predator and prey organisms are found. The consideration of all these parameters serves to characterize the hydrodynamics of a particular site.

Ferner et al. [9] studied whelk-clam interactions at the House Creek and Dead Man's Hammock sites. Smee et al. [35] studied crab-clam interactions at the Herb River, Moon River, Skidaway River, and Wilmington River sites. Sites were selected based on the existence of distinct predator communities for each respective study. Differences in foraging behavior between the two predator study organisms have been studied, and blue crabs have been characterized as better foragers at small flow rates, while whelks are more successful at large flow rates [24]. Smee et al. [34] suggests that whereas crabs and whelks can successfully forage at moderate levels of TI, whelks continue to forage effectively at higher levels of TI and crabs do not. These findings suggest that the locations where blue crabs were found to have foraging success would be characterized by smaller TI than those where thriving whelk populations occur. However, the variability among whelk sites bordering Wassaw Sound and crab sites further inland does not provide a single indicator among the sets presented in this study (see Section 5.3.1). There may be competing or amplifying effects between the various turbulent characteristics presented in this study, but a clear delineation between the sites is not apparent.

5.4 Future Directions

The results of this study provide some insight into directions for future work. As seen in the discussion of temporal and spatial comparisons, great variability can exist both among sites and day-to-day within a site. Consistent, long-term data collection at tidally-driven estuarine sites would provide a more comprehensive picture of hydrodynamic characteristics at the sites. Additionally, such an approach could help reduce the impact of environmental fluctuations in tidal strength or changing weather that could have contributed to the temporal variability found in this study. Repeated measurements at a site also would help to eliminate local topographical

variability and provide a broader sense of turbulence behavior on an environmental scale closely related to the predator and prey organisms of interest. The incorporation of estuary-level tide information regarding tide strength and periodicity could also identify larger-scale effects that were not apparent in this study and could have contributed to apparent variability in turbulent characteristics.

The ease of use and robust features of ADVs likely means they will continue to be commonly used for collecting point velocity time records in the field. It is therefore important to continue to improve methods for addressing data quality and computational accuracy. The phase filtration method used in this study has been shown, both by Goring and Nikora [12] and by this study, to have an impact on computations of turbulence parameters, like TKE for example. While the only sets that had large spike detection rates were those exhibiting banded behavior, it is conceivable that other studies might include non-banded sets with greater occurrence of spikes. It is important to determine the limits of the phase filtration method for sets with poor data quality. The inability of the phase filtration method to generate reasonable results for the DMHco20 and DMHsh20 sets indicates that there may be an upper limit of effectiveness even for sets that do not exhibit banded behavior, and at what level the breakdown in the method occurs is not currently clear. The wave-removal method employed in this study also could be improved. Peak detection has to be empirically tailored in each application. If it were possible to better detect peaks with less manual optimization, the method would become more robust and the errors associated with rigid offsets for peak spans could be eliminated.

REFERENCES

[1] Bell, R. G., Hume, T. M., Dolphin, T. J., Green, M. O., and Walters, R. A., "Characterisation of physical environmental factors on an intertidal sandflat, manukau harbor, new zealand," *Journal of Experimental Marine Biology and Ecology*, vol. 216, pp. 11–31, 1997.

[2] Benilov, A. Y. and Filyushkin, B. N., "Application of methods of linear filtration to an analysis of fluctuations in the surface layer of the sea," *Izvestiya Atmospheric and Oceanic Physics*, vol. 6, no. 3, pp. 810–819, 1970.

[3] Blasius, H., "Grenzschichten in flussigkeiten mit kleiner reibung," *Z. Math. Phys.*, vol. 56, pp. 1–37, 1908.

[4] Bricker, J. D. and Monismith, S. G., "Spectral wave-turbulence decomposition," *Journal of Atmospheric and Oceanic Technology*, vol. 24, no. 8, pp. 1479–1487, 2007.

[5] Chanson, H., Brown, R., Ferris, J., Ramsay, I., and Warburton, K., "Preliminary measaurements of turbulence and environmental parameters in a sub-tropical estuary of eastern australia," *Environmental Fluid Mechanics*, vol. 5, pp. 553–575, 2005.

[6] Chanson, H., Trevethan, M., and ichi Aoki, S., "Acoustic doppler velocimetry (adv) in small estuary: Field experience and signal post-processing," *Flow Measurement and Instrumentation*, vol. 19, pp. 307–313, 2008.

[7] Collins, M. B., Ke, X., and Gao, S., "Tidally-induced flow structure over intertidal flats," *Estuarine Coastal and Shelf Science*, vol. 46, no. 2, pp. 233–250, 1998.

[8] Drombroski, D. E. and Crimaldi, J. P., "The accuracy of acoustic Doppler velocimetry measurements in turbulent boundary layer flows over a smooth bed," *Limnology and Oceanography: Methods*, vol. 5, pp. 23–33, 2007.

[9] Ferner, M. C., Smee, D. L., and Weissburg, M. J., "Habitat complexity alters lethal and non-lethal olfactory interactions between predators and their prey," *Marine Ecology Progress Series*, vol. 374, pp. 13–22, 2009.

[10] Ferner, M. C. and Weissburg, M. J., "Slow-moving predatory gastropods track prey odors in fast and turbulent flow," *Journal of Experimental Biology*, vol. 208, pp. 809–819, 2005.

[11] Finelli, C. M., Hart, D. D., and Fonseca, D. M., "Evaluating the spatial resolution of an acoustic Doppler velocimeter and the consequences for measuring near-bed flows," *Limnology and Oceanography*, vol. 44, no. 7, pp. 1793–1801, 1999.

[12] Goring, D. G. and Nikora, V. I., "Despiking acoustic Doppler velocimeter data," *Journal of Hydraulic Engineering*, vol. 128, no. 1, pp. 117–126, 2002.

[13] Grant, W. D., III, A. J. W., and Glenn, S. M., "Bottom stress estimates and their prediction on the Northern California continental-shelf during Code-1 – the importance of wave-current interaction," *Journal of Physical Oceanography*, vol. 14, no. 3, pp. 506–527, 1984.

[14] Gross, T. F. and Nowell, A. R. M., "Spectral scaling in a tidal boundary-layer," *Journal of Physical Oceanography*, vol. 15, no. 5, pp. 496–508, 1985.

[15] Growns, I. O. and Davis, J. A., "Longitudinal changes in near-bed flows and macroinvertebrate communities in a Western-Australian stream," *Journal of the North American Benthological Society*, vol. 13, no. 4, pp. 417–438, 1994.

[16] Hart, D., Clark, B., and Jasentuliyana, A., "Fine-scale field measurement of benthic flow environments inhabited by stream invertebrates," *Limnology and Oceanography*, vol. 41, no. 2, pp. 297–308, 1996.

[17] Hay, M. E., "Marine chemical ecology: Chemical signals and cues structure marine populations, communities, and ecosystems," *Annual Review of Marine Systems*, vol. 1, pp. 193–212, 2009.

[18] Jackson, J. L., Webster, D. R., Rahman, S., and Weissburg, M. J., "Bed-roughness effects on boundary-layer turbulence and consequences for odor-tracking behavior of blue crabs (*Callinectes sapidus*)," *Limnology and Oceanography*, vol. 52, no. 5, pp. 1883–1897, 2007.

[19] Kawanisi, K. and Yokosi, S., "Mean and turbulence characteristics in a tidal river," *Estuarine Coastal and Shelf Science*, vol. 38, no. 5, pp. 447–469, 1994.

[20] Kolmogorov, A. N., "The local structure of turbulence in incompressible viscous fluid for very large reynolds numbers," *Dokl. Akad. Nauk SSSR*, vol. 30, pp. 301–305, 1941.

[21] Kraus, N. C., Lohrmann, A., and Cabrera, R., "New acoustic meter for measuring 3D laboratory flows," *Journal of Hydraulic Engineering*, vol. 120, pp. 406–412, 1994.

[22] Le Hir, P., Roberts, W., Cazaillet, O., Christie, M., Bassoullet, P., and Bacher, C., "Characterization of intertidal flat hydrodynamics," *Continental Shelf Research*, vol. 20, no. 12-13, pp. 1433–1459, 2000.

[23] Pope, S. B., *Turbulent Flows*. Cambridge, England: Cambridge University Press, 2000.

[24] Powers, S. P. and Kittinger, J. N., "Hydrodynamic mediation of predator-prey interactions: differential patterns of prey susceptibility and predator success explained by variation in water flow," *Journal of Experimental Marine Biology and Ecology*, vol. 273, pp. 171–187, 2002.

[25] Prandtl, L., "A report on testing for built-up turbulence," *Zeitschrift Fur Angewandte Mathematik Und Mechanik*, vol. 5, pp. 136–139, 1925.

[26] Precht, E. F., Janssen, F., and Huettel, M., "Near-bottom performance of the acoustic Doppler velocimeter (ADV) – a comparative study," *Aquatic Ecology*, vol. 40, pp. 481–492, 2006.

[27] Rahman, S. and Webster, D. R., "The effect of bed roughness on scalar fluctuations in turbulent boundary layers," *Experiments in Fluids*, vol. 38, no. 3, pp. 372–384, 2005.

[28] Reynolds, O., "An experimental investigation of the circumstances which determine whether the motion of water shall be direct or sinuous, and of the law of resistance in parallel shear channels," *Proceedings of the Royal Society of London Series A — Mathematical Physical and Engineering Sciences*, vol. 35, pp. 84–99, 1883.

[29] Richardson, L. F., *Weather Prediction by Numerical Process*. Cambridge, England: Cambridge University Press, 1922.

[30] Robson, B. J., Chester, E. T., and Davis, J. A., "Manipulating the intensity of near-bed turbulence in rivers: effects on benthic invertebrates," *Freshwater Biology*, vol. 42, no. 4, pp. 645–653, 1999.

[31] Shaw, W. J. and Trowbridge, J. H., "The direct estimation of near-bottom turbulent fluxes in the presence of energetic wave motions," *Journal of Atmospheric and Oceanic Technology*, vol. 18, no. 9, pp. 1540–1557, 2001.

[32] Shiono, K. and West, J. R., "Turbulent perturbations of velocity in the conwy estuary," *Estuarine, Coastal and Shelf Science*, vol. 25, pp. 533–553, 1987.

[33] Smee, D. L., Ferner, M. C., and Weissburg, M. J., "Alteration of sensory abilities regulates the spatial scale of nonlethal predator effects," *Oecologia*, vol. 156, no. 2, pp. 399–409, 2008.

[34] Smee, D. L. and Weissburg, M. J., "Clamming up: environmental forces diminish the perceptive ability of bivalve prey," *Ecology*, vol. 87, pp. 1587–1598, 2006.

[35] Smee, D. L., Ferner, M. C., and Weissburg, M. J., "Nonlinear relationship between estuarine hydrodynamics and predation intensity," *Ecology*, In Press.

[36] Spalart, P. R., "Direct simulation of a turbulent boundary-layer up to $R\theta = 1410$," *Journal of Fluid Mechanics*, vol. 187, pp. 61–98, 1988.

[37] Sunardi, Asaeda, T., and Manatunge, J., "Physiological responses of top-mouth gudgeon (*Pseudorasbora parva*), to predator cues and variation of current velocity," *Aquatic Ecology*, vol. 41, pp. 111–118, 2007.

[38] Talke, S. A. and Stacey, M. T., "The influence of oceanic swell on flows over an estuarine intertidal mudflat in San Francisco Bay," *Estuarine Coastal and Shelf Science*, vol. 58, no. 3, pp. 541–554, 2003.

[39] Tennekes, H. and Lumley, J. L., *A First Course in Turbulence*. Cambridge, Massachusetts: MIT Press, 1972.

[40] Trevethan, M. and Chanson, H., "Turbulent mixing in a small estuary: Detailed measurements," *Estuarine, Coastal and Shelf Science*, vol. 81, pp. 191–200, 2009.

[41] Trevethan, M., Chanson, H., and Brown, R., "Turbulent measurments in a small subtropical estuary with semidiurnal tides," *Journal of Hydraulic Engineering*, vol. 11, pp. 1665–1670, 2008.

[42] Trowbridge, J. H., "On a technique for measurement of turbulent shear stress in the presence of surface waves," *Journal of Atmospheric and Oceanic Technology*, vol. 15, pp. 290–298, 1988.

[43] Trowbridge, J. H., "On a technique for measurement of turbulent shear stress in the presence of surface waves," *Journal of Atmospheric and Oceanic Technology*, vol. 15, no. 1, pp. 290–298, 1998.

[44] Trowbridge, J. H., Geyer, W. R., Bowen, M. M., and Williams, A. J., "Near-bottom turbulence measurements in a partially mixed estuary: Turbulent energy balance, velocity structure, and along-channel momentum balance," *Journal of Physical Oceanography*, vol. 29, no. 12, pp. 3056–3072, 1999.

[45] van der Ham, R., Fontijn, H. L., Kranenburg, C., and Wintwerp, J. C., "Turbulent exchange of fine sediments in a tidal channel in the ems/dollard estuary. part i: Turbulence measurements," *Continental Shelf Research*, vol. 21, pp. 1605–1628, 2001.

[46] von Karman, T., "Mechanische ahnlichkeit und turbulenz," in *Proceedings of the Third International Congress of Applied Mechanics*, (Stockholm, Sweden), pp. 85–105, 1930.

[47] Voulgaris, G. and Trowbridge, J. H., "Evaluation of the acoustic doppler velocimeter (ADV) for turbulence measurements," *Journal of Atmospheric and Oceanic Technology*, vol. 51, no. 1, pp. 272–289, 1998.

[48] Voulgaris, G. and Meyers, S. T., "Temporal variability of hydrodynamics, sediment concentration and sediment settling velocity in a tidal creek," *Continental Shelf Research*, vol. 24, pp. 1659–1683, 2004.

[49] Weissburg, M. J. and Zimmer-Faust, R. K., "Life and death in moving fluids: hydrodynamic effects on chemosensory-mediated predation," *Ecology*, vol. 74, no. 5, pp. 1428–1443, 1993.

[50] Weissburg, M. J., "The fluid dynamical context of chemosensory behaviour," *Biological Bulletin*, vol. 198, no. 2, pp. 188–202, 2000.

[51] Weissburg, M. J., Ferner, M. C., Pisut, D. P., and Smee, D. L., "Ecological consequences of chemically mediated prey perception," *Journal of Chemical Ecology*, vol. 28, no. 10, pp. 1953–1970, 2002.

[52] Zagarola, M. V. and Smits, A. J., "Mean-flow scaling of turbulent pipe flow," *Journal of Fluid Mechanics*, vol. 373, pp. 33–79, 1998.

[53] Zimmer, R. K. and Butman, C. A., "Chemical signaling processes in the marine environment," *The Biological Bulletin*, vol. 198, no. 2, pp. 168–187, 2000.